

Chapter 7. Load and response

Wind tunnel experiments performed in different wind tunnels and thus different boundary layers allowed to study the effect of certain atmospheric boundary layer properties on wind forces and pressures. A simple design tool, generalizable to any atmospheric boundary layer flow is then derived by using the results in WiSt and CRIACIV (section 7.1). This model can be applied to calculate the quasi-static response of the tower to the stochastic wind loading process in any design conditions. Basic assumptions are linear structural analysis and quasi-static behaviour.

In sections 7.2 and 7.3 the beam and shell responses are analyzed. The effect of the asymmetric load due to the rings along the height is also quantified.

7.1 Modelling of wind load

The time-averaged mean load and the load covariances (i.e. rms values and correlation coefficients) are the input data to evaluate the quasi-static structural response to the stochastic wind loading process. The breaking-up of the covariances in the frequency domain is not necessary because the mechanical admittance is constant. More sophisticated methods to evaluate the structural response are the spectral method in the frequency domain, which is applicable to linear structures, and the time history method applicable to both linear and non-linear structures.

This section addresses the modelling of the stochastic quasi-static design wind load, with respect to the turbulent properties of the flow, by combining results of both WiSt and CRIACIV wind tunnels. The model refers to the basic configuration (without rings) and has a general application for cylindrical towers of any aspect ratio⁶. It also represents the reference case to evaluate the effect of the rings.

7.1.1 Influence of boundary layer flows on force coefficients

The comparison of experimental data recorded in different wind tunnels – and thus different atmospheric boundary layers – cannot be addressed without considering the properties of the flow in which such data are measured. This approach is pursued in this section with regard to the force coefficients.

⁶ For low-aspect ratio circular cylinders, i.e. for H/D less than a critical value (which ranges from 1 to 6, depending on the boundary layer thickness) a different flow structure develops in the wake (see section 3.5). The proposed wind load model is thus appropriate for sufficiently slender circular cylinders, e.g. $H/D \geq 6$.

The local mean value of the drag coefficient that results from the experiments (EXP) is calculated by definition as:

$$C_{D,m}^{EXP}(z) = \frac{F_m^{EXP}(z)}{q_m(z)D} \quad (7.1)$$

where $q_m(z)$ is the local velocity pressure, i.e. at the level of the pressure measurement. Similarly, the coefficient can be defined with respect to the velocity pressure at the top of the tower:

$$C_{D,m}^{EXP,H}(z) = \frac{F_m^{EXP}(z)}{q_m(H)D} \quad (7.2)$$

The comparison between results at WiSt and CRIACIV (Figure 7.1a) shows that the local mean force coefficients – calculated according to equation (7.1) – depend on the type of boundary layer. In fact, a certain boundary layer – characterized by its velocity and pressure gradients – may enhance certain flow movements. The time-averaged wake structure may also change, as addressed in section 6.3. While the tip effect is not so sensitive to the characteristics of the boundary layer, lateral and especially wake suction at middle height at CRIACIV are lower than at WiSt. This issue was commented with regard to Figure 6.17, which explains the differences between the two drag curves in Figure 7.1a.

The use of $q_m(H)$ instead of $q_m(z)$ allows to remove the differences due to the boundary layer and the results in the two wind tunnels are in wonderful agreement (Figure 7.1b). However, by using $q_m(H)$, an even more constraining dependency is gained: the one on the aspect ratio. The coefficients in Figure 7.1b are thus only valid for the aspect ratio of the experiments, that is $H/D = 6.7$.

The rms values of the forces (equation(7.3)) are necessarily different in the two wind tunnels (Figure 7.2), because the turbulence in the flow (σ_u) is different (Figure 7.3).

$$C_{D,\sigma}^{EXP,H}(z) = \frac{F_m^{EXP}(z)}{q_m(z)D} \quad (7.3)$$

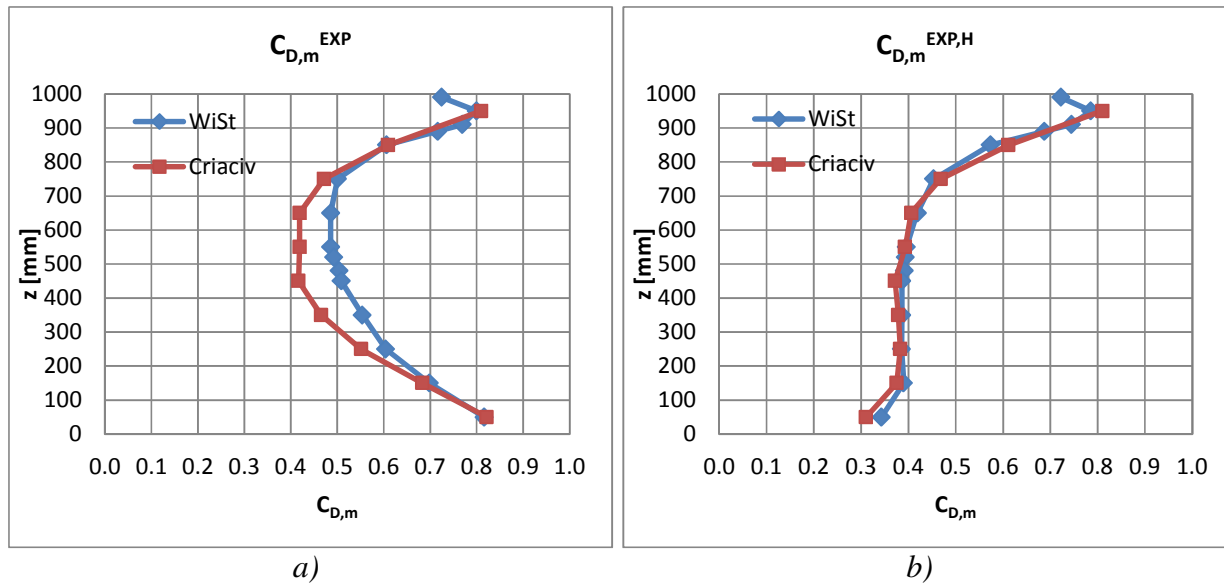


Figure 7.1 Mean drag coefficients $C_{D,m}$: comparison between WiSt and CRIACIV data (EXP)
 a) $C_{D,m}$ by using local velocity pressure $q_m(z)$; b) $C_{D,m}$ by using velocity pressure on top $q_m(H)$

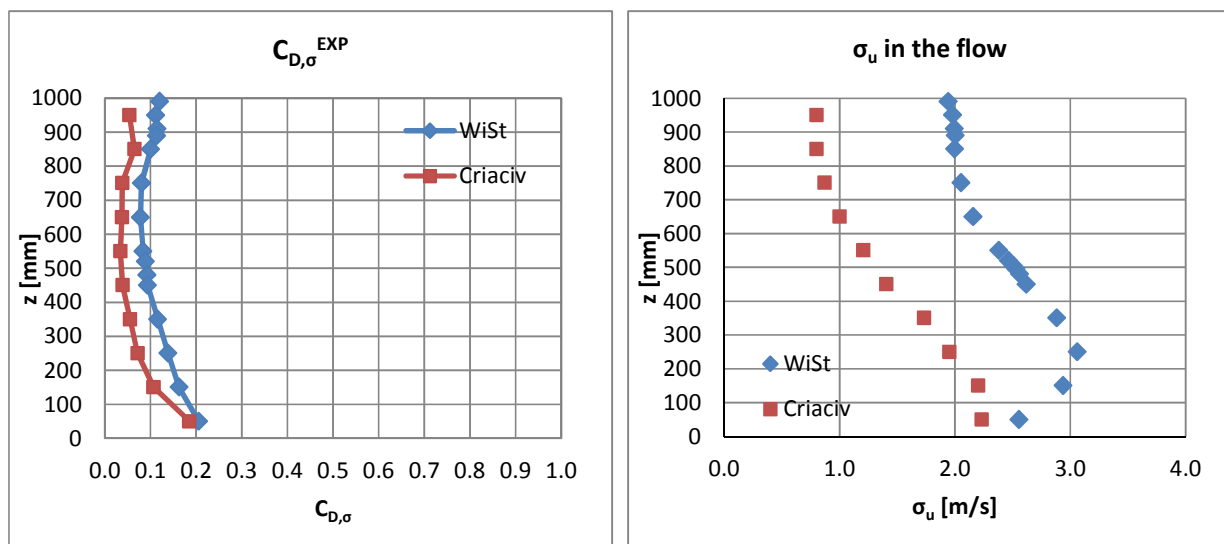


Figure 7.2 Rms drag coefficients $C_{D,\sigma}$: comparison between WiSt and CRIACIV experimental data (EXP)

Figure 7.3 Rms values of along wind velocity (σ_u) at WiSt and CRIACIV

It is then apparent that, in order to compare results obtained in different boundary layer flows and codify the force coefficients, a more general approach should be used, which includes the mean velocity pressure and the turbulence intensity.

The code approach is based on the peak force coefficient ($C_{D,peak}$), that is the ratio of peak (drag) force and peak velocity pressure (equation (7.4)). The latter is multiplied by D as usual, in order to obtain the dimension of force per unit length. In this way, the results in different boundary layer flows are more comparable even by using the local

velocity pressure and not the velocity pressure on top (Figure 7.4). The peak force coefficients are generalizable for load modelling.

$$\begin{aligned}
 C_{D, peak} &= \frac{F_{peak}}{q_{peak} D} = \frac{F_m^{EXP} + k_F F^{EXP}}{\sigma} = \\
 &= \frac{C_{D,m}^{EXP} q_m D + k_F C_{D,\sigma}^{EXP} q_m D}{q_m \left(1 + 2k_p I_u\right) D} = \frac{C_{D,m}^{EXP} + k_F C_{D,\sigma}^{EXP}}{1 + 2k_p I_u}
 \end{aligned}
 \tag{7.4}$$

The peak factors in equation (7.4) are assumed equal to 3.5 for both forces and velocities (k_F and k_p , respectively). The apex (^{EXP}) means resulting from experiments. It should be mentioned, however, that the code definition of the peak force includes the dynamic factor and the size factor. Relying on the experimental data, $C_{dyn} = 1$ because the model is rigid, C_s is assumed equal to 1, too, although it should take into account the decrease in correlation around the circumference. It could be partially responsible for the differences in the two curves in Figure 7.4.

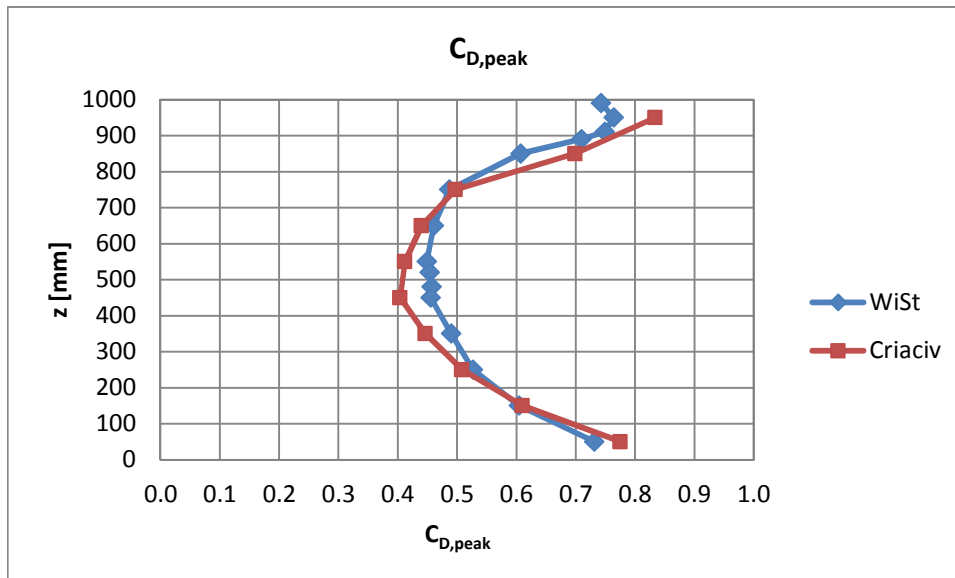


Figure 7.4 Peak drag coefficient $C_{D,peak}$ related to $q_{peak}(z)$

By assuming a quasi-stationary approach (the aerodynamic coefficient is invariant with respect to time) and linearized model ($I_u^2 \ll 1$), the intensity of force is twice the turbulence intensity and the peak force can be split up into its mean and fluctuating components as follows:

$$F_m = C_{D, peak} q_m D \quad (7.5)$$

$$F_\sigma = C_{D, peak} 2I_u q_m D \quad (7.6)$$

Therefore, the mean and the rms values of the force coefficients to be used in the proposed beam-load model (^{LM}) are:

$$C_{D, m}^{LM} = \frac{F_m}{q_m D} = C_{D, peak} \quad (7.7)$$

$$C_{D, \sigma}^{LM} = \frac{F_\sigma}{q_m D} = C_{D, peak} 2I_u \quad (7.8)$$

The behaviour of the peak drag coefficient along the height resembles the profile of the $C_{D, m}$, which increases both at tower top (tip effect) and at the bottom, as previously commented in sections 3.5 and 4.4.

The main results are reported in the following tables.

Table 7.1 Boundary layer flow at WiSt

	z [mm]	z/H	U [m/s]	σ_u	$q_m(z)/q_m(H)$	I_u
WiSt: Boundary layer	990	0.99	25.16	1.9431	1.00	0.0772
	950	0.95	24.98	1.9826	0.98	0.0794
	910	0.91	24.79	1.9972	0.97	0.0806
	890	0.89	24.70	2.0041	0.96	0.0811
	850	0.85	24.30	2.0003	0.95	0.0823
	750	0.75	23.78	2.0536	0.91	0.0863
	650	0.65	23.32	2.1580	0.86	0.0925
	550	0.55	22.66	2.3833	0.81	0.1052
	520	0.52	22.43	2.4656	0.80	0.1099
	480	0.48	22.16	2.5621	0.78	0.1156
	450	0.45	21.91	2.6181	0.76	0.1195
	350	0.35	21.01	2.8842	0.70	0.1373
	250	0.25	20.05	3.0614	0.64	0.1527
	150	0.15	18.77	2.9381	0.56	0.1566
50	0.05	16.28	2.5565	0.42	0.1571	

Table 7.2 Drag coefficients at WiSt

	z/H	$C_{D,m}^{EXP}$	$C_{D,m}^{EXP.H}$	$C_{D,\sigma}^{EXP}$	$I_F = \frac{C_{D,\sigma}^{EXP}}{C_{D,m}^{EXP}}$	I_F/I_u	$C_{D,peak}$
WiSt: Drag Coeff.	0.99	0.7246	0.7221	0.1198	0.1654	2.1407	0.7425
	0.95	0.7992	0.7853	0.1112	0.1391	1.7528	0.7640
	0.91	0.7693	0.7447	0.1148	0.1492	1.8519	0.7487
	0.89	0.7158	0.6877	0.1134	0.1584	1.9523	0.7096
	0.85	0.6061	0.5732	0.1001	0.1652	2.0073	0.6069
	0.75	0.5007	0.4535	0.0801	0.1601	1.8539	0.4869
	0.65	0.4858	0.4189	0.0781	0.1607	1.7366	0.4606
	0.55	0.4859	0.3956	0.0838	0.1725	1.6401	0.4488
	0.52	0.4924	0.3933	0.0888	0.1804	1.6411	0.4540
	0.48	0.5039	0.3915	0.0922	0.1830	1.5825	0.4568
	0.45	0.5083	0.3863	0.0937	0.1844	1.5430	0.4554
	0.35	0.5540	0.3862	0.1161	0.2095	1.5262	0.4897
	0.25	0.6044	0.3854	0.1386	0.2293	1.5015	0.5266
	0.15	0.6980	0.3899	0.1626	0.2330	1.4879	0.6046
0.05	0.8160	0.3429	0.2055	0.2519	1.6034	0.7313	

Table 7.3 Boundary layer flow at CRIACIV

	z [mm]	z/H	U [m/s]	σ_u	$q_m(z)/q_m(H)$	I_u
CRIACIV: Boundary layer	950	0.95	28.36	0.8022	1.00	0.0283
	850	0.85	28.40	0.8033	1.00	0.0283
	750	0.75	28.26	0.8731	0.99	0.0309
	650	0.65	27.91	1.0020	0.97	0.0359
	550	0.55	27.47	1.2085	0.94	0.0440
	450	0.45	26.79	1.4070	0.89	0.0525
	350	0.35	25.58	1.7340	0.81	0.0678
	250	0.25	23.65	1.9534	0.70	0.0826
	150	0.15	21.03	2.2015	0.55	0.1047
	50	0.05	17.44	2.2339	0.38	0.1281

Table 7.4 Drag coefficients at CRIACIV

	z/H	$C_{D,m}^{EXP}$	$C_{D,m}^{EXP.H}$	$C_{D,\sigma}^{EXP}$	$I_F = \frac{C_{D,\sigma}^{EXP}}{C_{D,m}^{EXP}}$	I_F/I_u	$C_{D,peak}$
CRIACIV: Drag Coeff.	0.95	0.8099	0.8099	0.0539	0.0666	2.3547	0.8337
	0.85	0.6096	0.6113	0.0650	0.1066	3.7681	0.6986
	0.75	0.4717	0.4682	0.0380	0.0806	2.6070	0.4972
	0.65	0.4193	0.4062	0.0375	0.0894	2.4899	0.4400
	0.55	0.4192	0.3932	0.0341	0.0814	1.8498	0.4118
	0.45	0.4164	0.3717	0.0388	0.0931	1.7725	0.4037
	0.35	0.4652	0.3784	0.0552	0.1186	1.7494	0.4465
	0.25	0.5510	0.3831	0.0716	0.1299	1.5729	0.5079
	0.15	0.6830	0.3755	0.1069	0.1564	1.4941	0.6100
0.05	0.8213	0.3106	0.1852	0.2255	1.7602	0.7748	

7.1.2 Mean pressure coefficient distribution

The circumferential distribution of the mean pressure coefficients C_p on the external surface of the tower is described by the following parameters:

- $C_{p,max}$ = maximum pressure coefficient (at stagnation);
- φ_{min} and $C_{p,min}$ = angle and pressure coefficient at maximum lateral suction;
- φ_h and $C_{p,h}$ = angle of separation and pressure coefficient in the wake;

Depending on the circumferential angle φ , three ranges can be identified along the circumference, as shown in Figure 7.5. The distributions in the three ranges are described by expressions (7.9)-(7.11), derived by studies on cooling towers and codified in the VGB guideline (VGB, 2010).

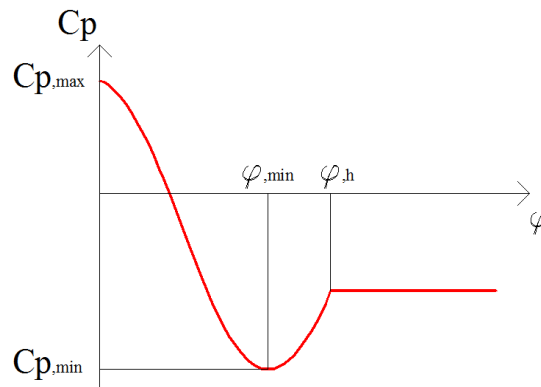


Figure 7.5 Pressure coefficients distribution in the three ranges
($0 < \varphi < \varphi_{min}$; $\varphi_{min} < \varphi < \varphi_h$; $\varphi_h < \varphi < 180^\circ$)

Range I: $0^\circ \leq \varphi \leq \varphi_{\min}$

$$C_P(\varphi) = C_{P, \max} - \left(C_{P, \max} - C_{P, \min} \right) \left(\sin \frac{90}{\varphi_{\min}} \varphi \right)^{\varepsilon_{\min}} \quad (7.9)$$

Range II: $\varphi_{\min} \leq \varphi \leq \varphi_h$

$$C_P(\varphi) = C_{P, \min} - \left(C_{P, \min} - C_{P, h} \right) \left(\sin \frac{90}{\varphi_h - \varphi_{\min}} (\varphi - \varphi_{\min}) \right)^{\varepsilon_h} \quad (7.10)$$

Range III: $\varphi_h \leq \varphi \leq 180^\circ$

$$C_P(\varphi) = C_{P, h} \quad (7.11)$$

This model is adapted to the experimental data of the solar tower along the height (WiSt results). The parameter ε_h has been chosen accordingly to the VGB guideline, while the parameter ε_{\min} has been calibrated by fitting the measured C_p values and matching the value of the measured drag coefficient. The values are reported in Table 7.5 and plotted in the following graphs. In particular, three spanwise regions can be identified along the height of the cylinder:

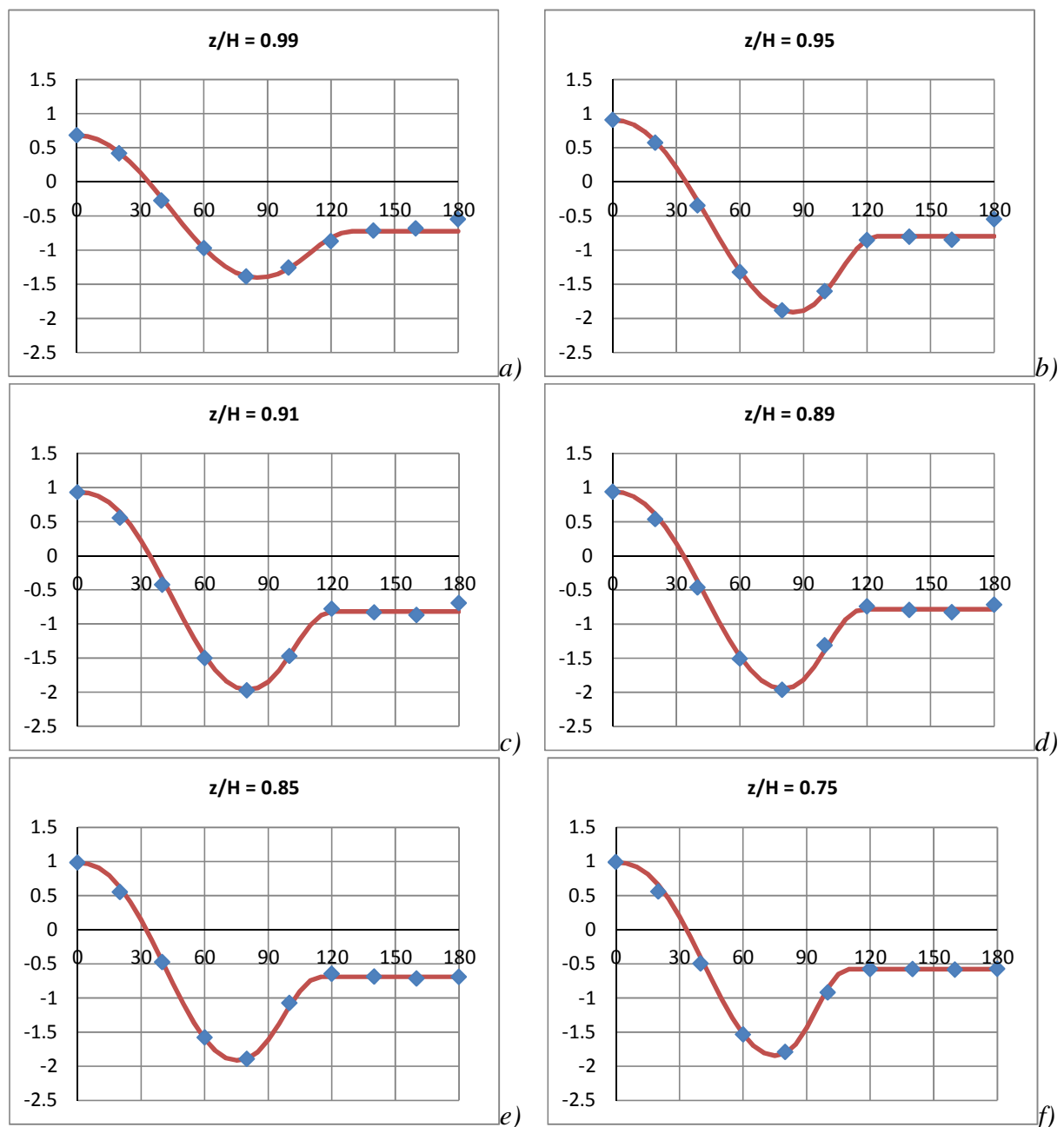
- tip region ($z' \leq 2D$, i.e. $z > 0.7H$, as z' starts at $z = H$ in downwards direction);
- normal region ($z > 0.5H$ and $z' > 2D$);
- low region ($z \leq 0.5H$).

Table 7.5 Mean pressure coefficients

	z/H	$C_{p, \max}$	$C_{p, \min}$	φ_{\min} [°]	$C_{p, h}$	φ_h [°]	ε_{\min}	ε_h	ΔC_p	C_D model	C_D meas.
TIP REGION	0.99	0.7	-1.40	85	-0.73	130	2.085	2.395	0.68	0.72	0.72
	0.95	0.9	-1.91	85	-0.79	125	2.189	2.395	1.11	0.80	0.80
	0.91	0.9	-1.96	80	-0.82	120	2.390	2.395	1.15	0.77	0.77
	0.89	0.9	-1.95	80	-0.78	118	2.277	2.395	1.16	0.72	0.72
	0.85	1.0	-1.91	75	-0.69	115	2.332	2.395	1.23	0.61	0.61
	0.75	1.0	-1.85	75	-0.58	110	2.395	2.395	1.27	0.50	0.50
NORMAL REGION	0.65	1.0	-1.77	75	-0.55	110	2.248	2.395	1.21	0.49	0.49
	0.55	1.0	-1.76	75	-0.54	110	2.238	2.395	1.22	0.49	0.49
LOW REGION	0.45	1.0	-1.86	75	-0.59	110	2.261	2.395	1.26	0.51	0.51
	0.35	1.0	-1.94	75	-0.66	110	2.359	2.395	1.28	0.55	0.55

0.25	1.0	-2.06	75	-0.75	115	2.474	2.395	1.31	0.60	0.60
0.15	1.0	-2.28	80	-0.86	120	2.256	2.395	1.42	0.70	0.70
0.05	1.1	-2.28	80	-0.99	110	2.052	2.395	1.29	0.80	0.80

The following figures (Figure 7.6, Figure 7.7, Figure 7.8) plot the circumferential distributions of mean pressure coefficients along the height. The three figures refer to the tip region, the normal region and the low region, respectively. Further variation of the distribution is also present within each region. Modelling according to equations (7.9), (7.10), (7.11) and experimental data are in good agreement.



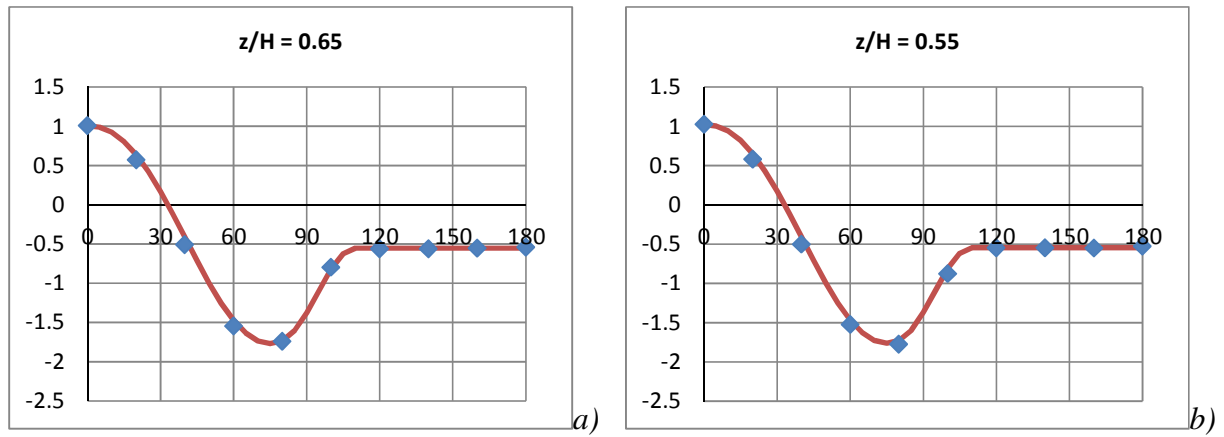


Figure 7.7 a-b) Mean pressure coefficients $C_{p,m}$: proposed model (red) and experimental data (blue) [x -axis = φ ($^\circ$), y -axis = $C_{p,m}$]. Normal region ($z' > 2D$; $z/H > 0.5$)

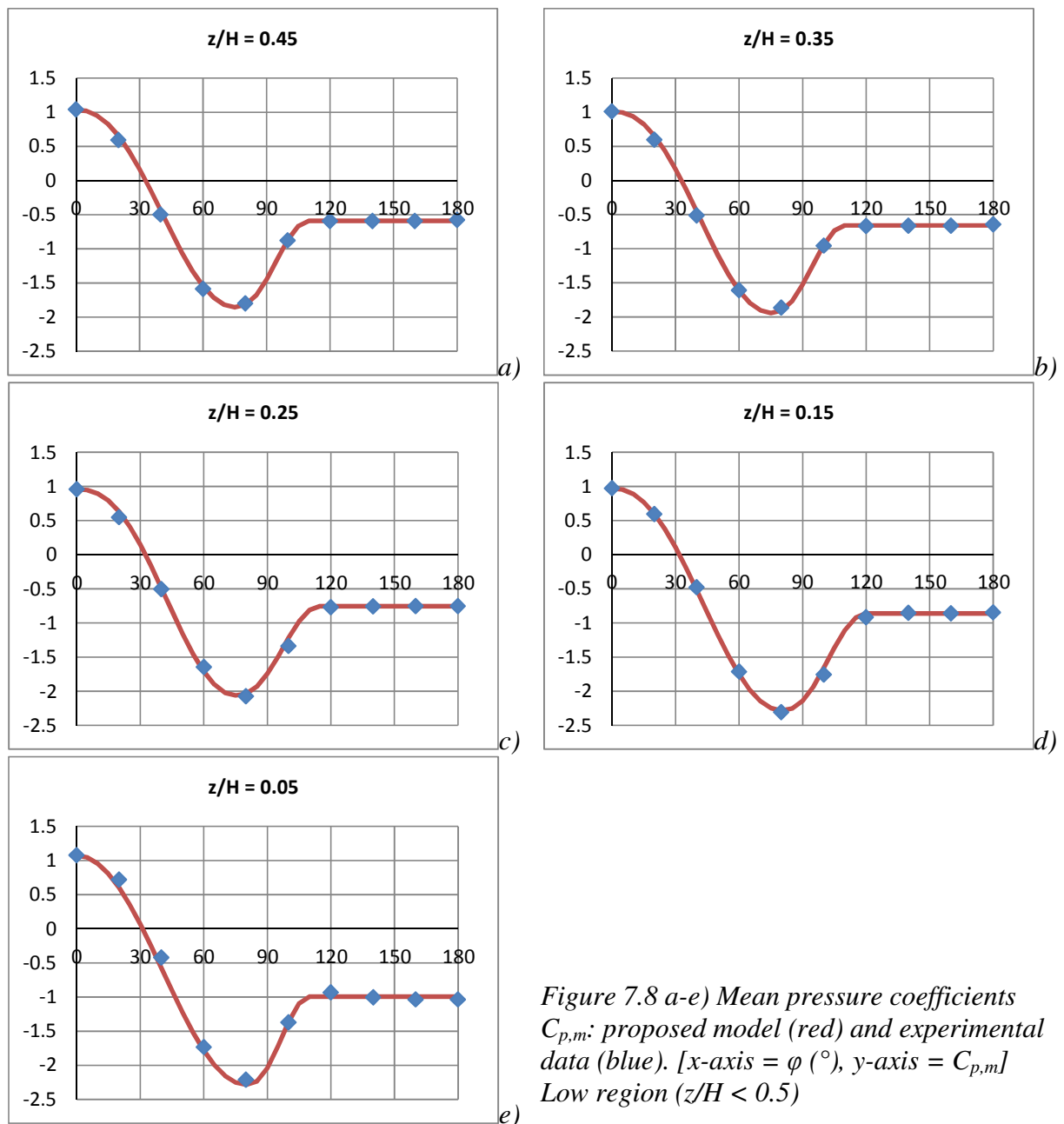


Figure 7.8 a-e) Mean pressure coefficients $C_{p,m}$: proposed model (red) and experimental data (blue). [x -axis = φ ($^\circ$), y -axis = $C_{p,m}$] Low region ($z/H < 0.5$)

Finally, Figure 7.9 shows an overview of the distributions of the mean pressure coefficients along the height.

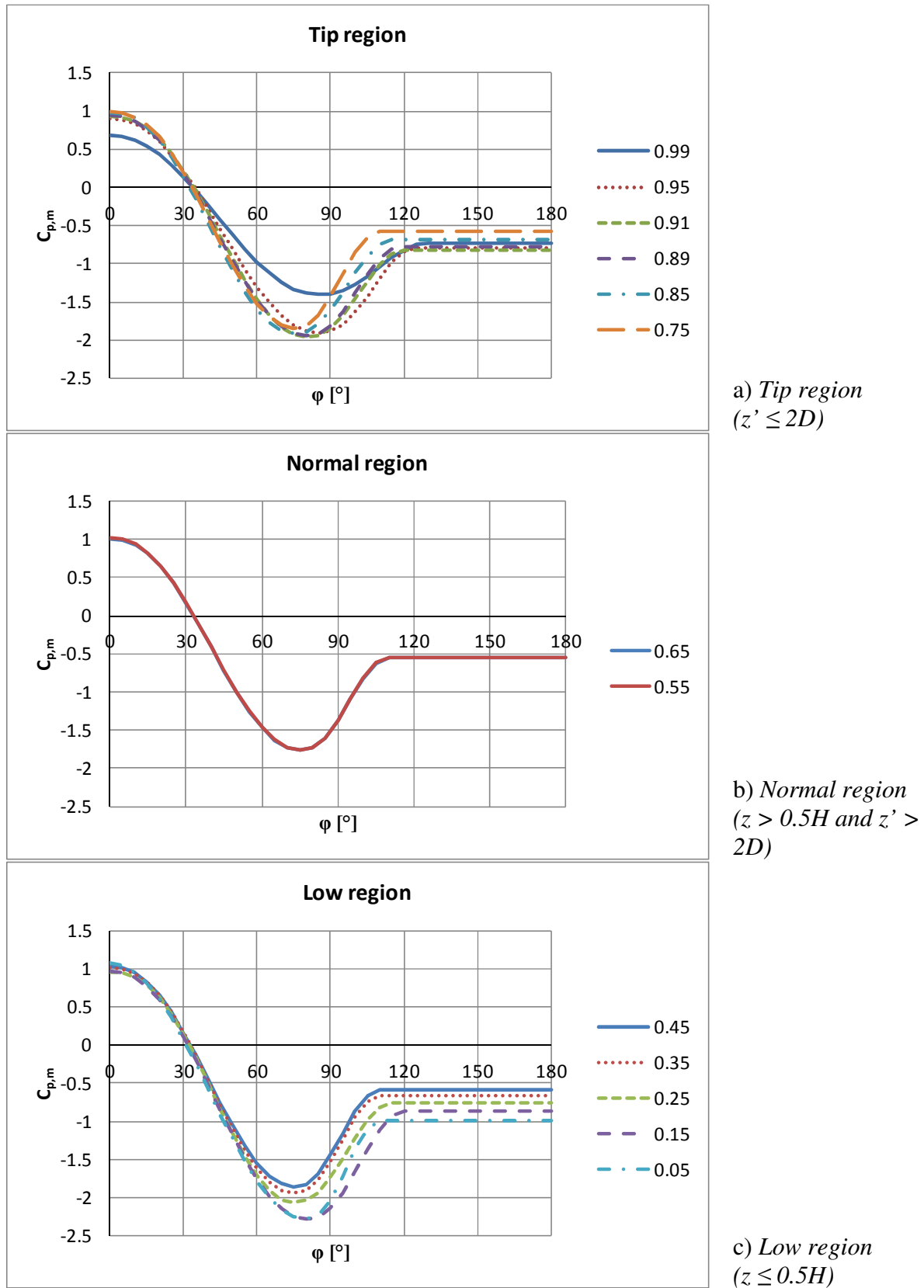


Figure 7.9 a-c) Mean pressure coefficients: variation along the height

7.1.3 Rms pressure coefficients: body-induced and turbulence-induced fluctuations

Pressure fluctuations on the shell surface are both body-induced and turbulence-induced. They are due to vortex shedding and to the turbulence of the incoming flow, respectively. In order to model the turbulence-induced fluctuations with regard to the turbulent properties of the boundary layer, the question arises whether it is possible to separate the two contributions. Then, the easiest approach would be to relate the turbulence-induced fluctuations around the circumference to the fluctuation at stagnation, which in turn depends on $I_u(z)$, and to measure the body-induced pressure fluctuations in smooth flow.

The problem cannot be addressed linearly in the rms values, but in the variances. Furthermore, the question is much more complicated because the turbulence of the incoming flow may be responsible for enhancing body-induced fluctuations. However, the simplifying assumption that body-induced pressure fluctuations ($p_{\sigma, BI}^2$) and turbulence-induced pressure fluctuations $p_{\sigma, TI}^2$ are statistically independent finds support in literature (see, for example, the rapid distortion theory by Hunt (1972/1975/1990), section 3.4) and can be accepted as long as I_u is not too high. This assumption is the basis for the model proposed in the following.

If the covariances between body-induced and turbulence-induced fluctuations are assumed to be zero (in view of the statistical independence), it follows that the pressure fluctuation which is measured during an experiment in turbulent flow is just the sum – in terms of variances – of the two contributions, the turbulence-induced one ($_{TI}$) and the body-induced one ($_{BI}$), as follows:

$$p_{\sigma}^2 = p_{\sigma, TI}^2 + p_{\sigma, BI}^2 \quad (7.12)$$

Although it is apparent in the spectra that higher energy content is around the Strouhal peak, the separation of the two contributions is not immediate, especially in high turbulent flow. In terms of variances, the comparison of results in the two wind tunnels (WiSt and CRIACIV) resulted to be helpful. In fact, at CRIACIV the turbulence intensity is very low at high levels and this allows a first good estimation of the body-induced contribution at those levels. Then, extrapolation is made at $I_u = 0$, so that the actual body-induced fluctuations can be estimated all around the circumference. Since equation (7.12) holds in general, the theory can be further extended at low levels.

The validation of this simplified modelling is through comparison of full-scale results on cooling towers (Pröpper, 1977), as explained later on.

In the following, the level $z/H = 0.85$ is chosen as representative for explanation. At that level, $I_u = 0.028$ at CRIACIV and $I_u = 0.082$ at WiSt.

The circumferential distribution of the total variance of the pressure coefficients ($C_{p,\sigma}^2$) is shown in Figure 7.10. The two sides of the cylinder are not perfectly symmetric due to inhomogeneities of the flow in both wind tunnels. In fact, this is not surprising in experiments in turbulent boundary layer flows. Anyway, the differences between the two sides of the cylinder are small and they do not prevent the development of a model which is, of course, symmetric. Figure 7.10 shows that at stagnation the pressure fluctuations at CRIACIV are very small, resulting from low I_u . At 100° and 260° the fluctuations are instead high and they must be mostly body-induced. An insight in the spectra gives a more clear explanation over frequencies. As can be seen in Figure 7.11, at $z/H = 0.85$ it is not only the Karman vortex shedding that produces the majority of body-induced contribution, but there is a strong interaction with the tip-associated vortices.

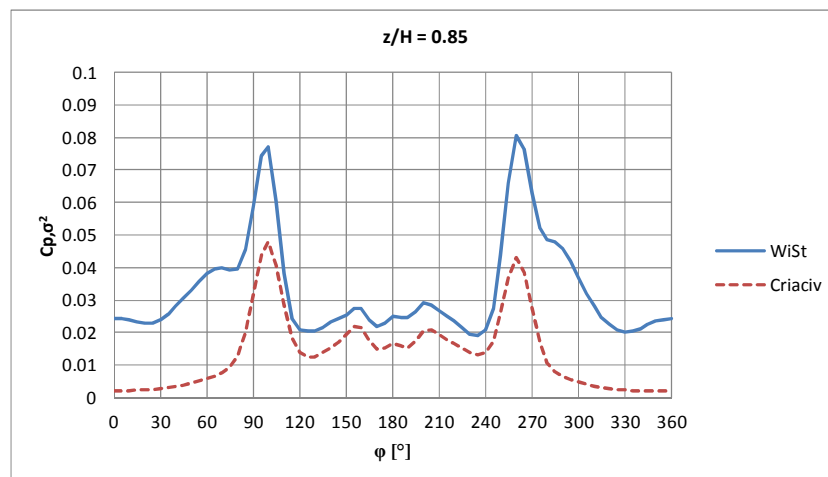


Figure 7.10 Circumferential distribution of the total variance $C_{p,\sigma}^2$ (body+turb.-induced)

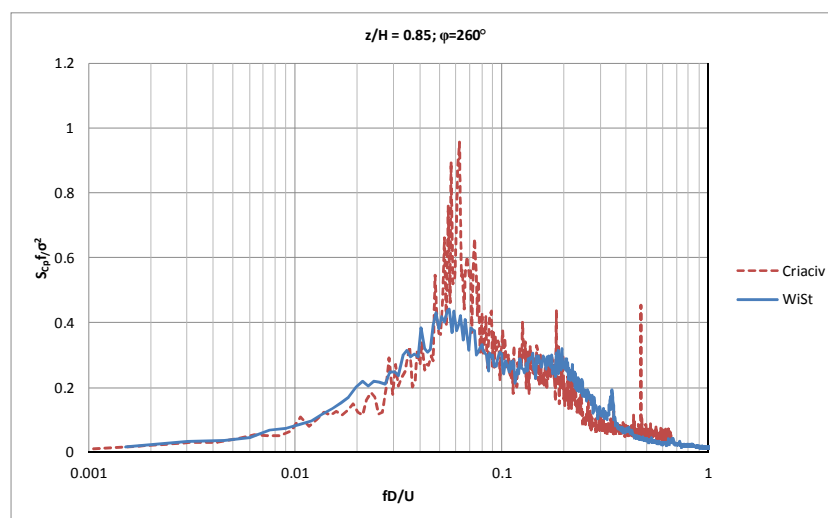


Figure 7.11 Power spectral densities of C_p at $z/H = 0.85$, 260°
 $C_{p,\sigma}^2 = 0.0805$ (WiSt); $C_{p,\sigma}^2 = 0.0400$ (CRIACIV)

In order to separate body-induced and turbulence-induced contributions, the variances measured at CRIACIV (mostly body-induced) are compared to the variances measured at WiSt (mainly, but not only, turbulence-induced). A tentative extrapolation at $I_u = 0$ is proposed in Figure 7.12 and Figure 7.13. Since two experimental points are available at each angle, the extrapolation can only be linear in the plane σ^2, I_u^2 . In any case, a linear extrapolation seems to be rather good for several reasons.

First of all, at 0° and up to 60° the body-induced contribution in smooth flow results to be zero and this confirms the expectations: at those angles the pressure fluctuations are mostly induced by the flow fluctuations. Then, moving downstream, the body-induced percentage increases and at 180° the slope of the line is almost flat (Figure 7.13). It means that the fluctuations in the wake are almost completely body-induced and they do not depend significantly on the upwind turbulence. It is also interesting to see that most of the lines in both figures are approximately parallel. It means that the rate of turbulence-induced fluctuations is almost the same at each circumferential angle. This is a further reason to relate the circumferential turbulence-induced distribution to only one reference angle, e.g. the stagnation angle, that can be related to the flow properties.

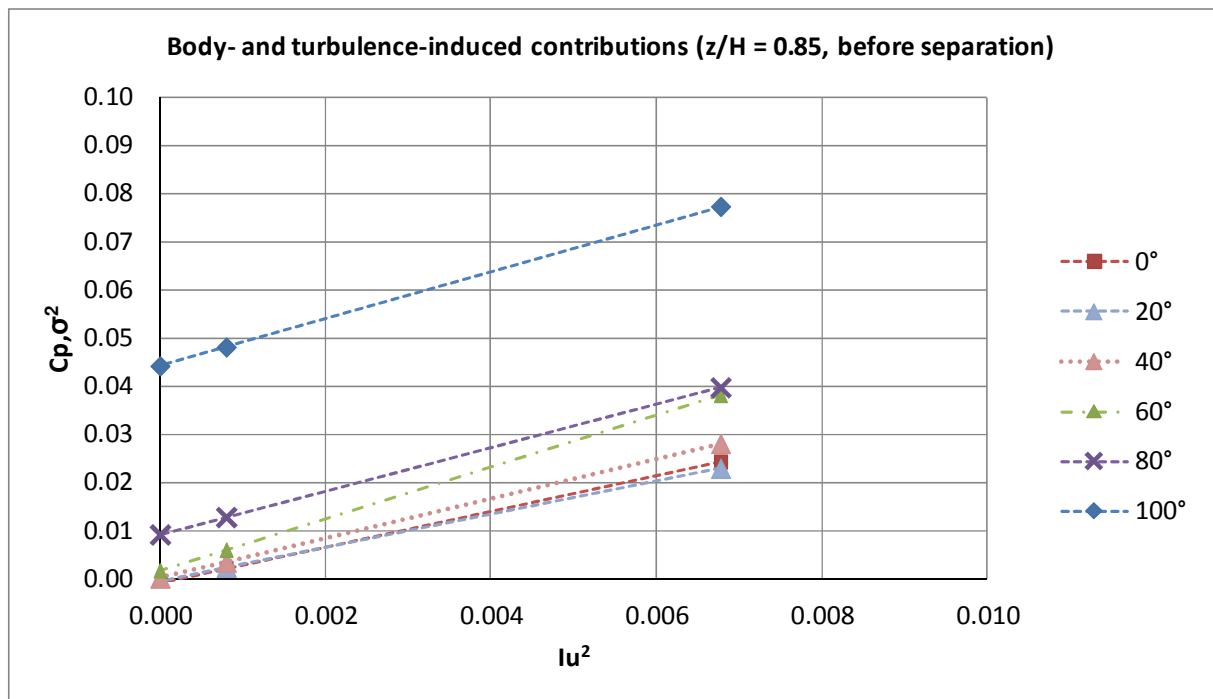


Figure 7.12 Extrapolations of body-induced contributions at angles before separation based on experiments at WiSt ($I_u = 0.082$ at $z/H = 0.85$) and at CRIACIV ($I_u = 0.028$ at $z/H = 0.85$)

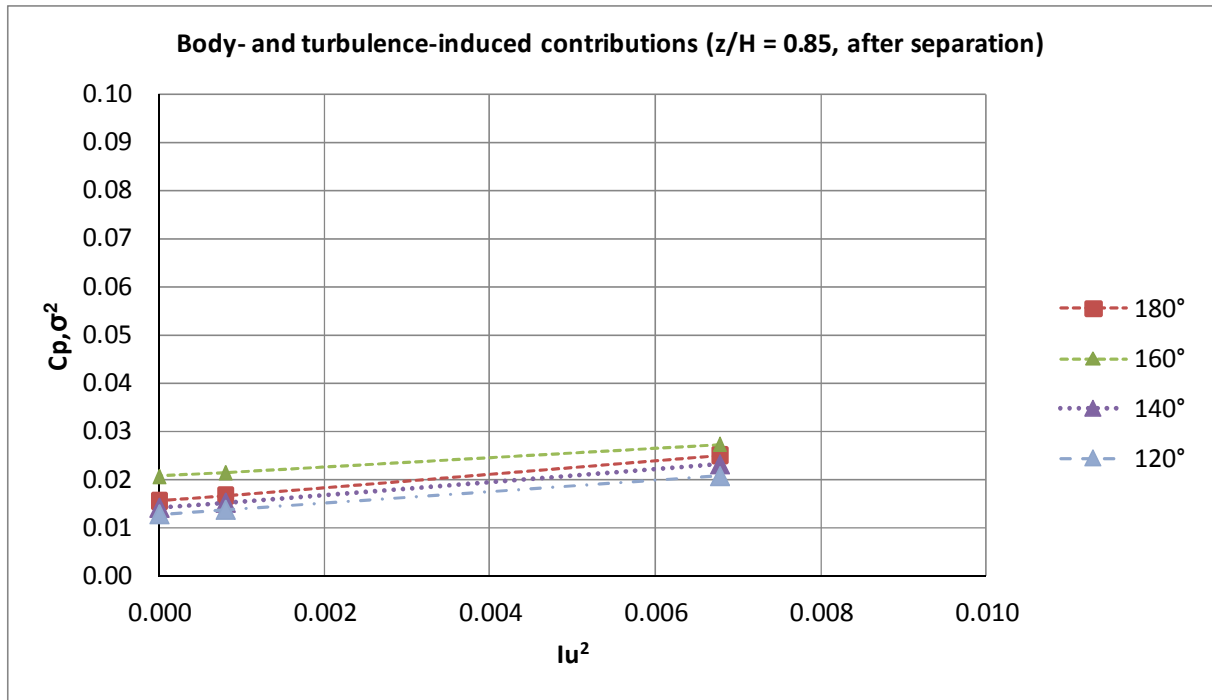


Figure 7.13 Extrapolations of body-induced contributions at angles after separation based on experiments at WiSt ($I_u = 0.082$ at $z/H = 0.85$) and at CRIACIV ($I_u = 0.028$ at $z/H = 0.85$)

The body-induced contribution extrapolated at $I_u = 0$ is then subtracted by the total variance measured at WiSt tunnel in high turbulent flow. The result represents the turbulence-induced part, which can be modeled around the circumference through the factor $a(\varphi)$, defined as follows:

$$a^2(\varphi) = \frac{p_{\sigma^2, TI}(\varphi)}{p_{\sigma^2, TI}(0^\circ)} \rightarrow a(\varphi) = \frac{p_{\sigma, TI}(\varphi)}{p_{\sigma, TI}(0^\circ)} = \frac{C_{P, \sigma_{TI}}(\varphi)}{C_{P, \sigma_{TI}}(0^\circ)} \quad (7.13)$$

$p_{\sigma, TI}(\varphi)$ is the standard deviation of the turbulence-induced contribution of the wind pressure; $C_{p, \sigma, TI}(\varphi)$ is the standard deviation of the corresponding pressure coefficient. In particular, at $z/H = 0.85$ it is:

Table 7.6 Body-induced and turbulence-induced pressure fluctuations ($z/H = 0.85$)

φ [°]	C_{p, σ^2} (Wist)	C_{p, σ^2} (CRIACIV)	$C_{p, \sigma, BI}^2$	$C_{p, \sigma, TI}^2$ (WiSt)	$a^2(\varphi)$	$a(\varphi)$
0	0.0242	0.0021	0.0000	0.0242	1.0000	1.0000
20	0.0229	0.0023	0.0000	0.0229	0.9428	0.9710
40	0.0280	0.0033	0.0000	0.0280	1.1529	1.0737
60	0.0381	0.0059	0.0016	0.0365	1.5044	1.2265

80	0.0397	0.0127	0.0091	0.0306	1.2602	1.1226
100	0.0772	0.0480	0.0441	0.0331	1.3660	1.1688
120	0.0207	0.0137	0.0128	0.0079	0.3271	0.5719
140	0.0231	0.0152	0.0141	0.0090	0.3720	0.6100
160	0.0273	0.0214	0.0206	0.0067	0.2769	0.5262
180	0.0251	0.0167	0.0155	0.0095	0.3929	0.6268
200	0.0290	0.0204	0.0192	0.0098	0.4043	0.6359
220	0.0237	0.0166	0.0156	0.0081	0.3341	0.5780
240	0.0207	0.0138	0.0129	0.0078	0.3226	0.5680
260	0.0806	0.0431	0.0381	0.0425	1.7527	1.3239
280	0.0486	0.0108	0.0058	0.0428	1.7673	1.3294
300	0.0369	0.0047	0.0004	0.0365	1.5056	1.2270
320	0.0225	0.0027	0.0001	0.0224	0.9254	0.9620
340	0.0212	0.0021	0.0000	0.0212	0.8755	0.9357
360	0.0242	0.0021	0.0000	0.0242	1.0000	1.0000

The same principle is attempted at other levels and the coefficient $a(\varphi)$ is calculated according to equation (7.13). The results along the height are plotted in Figure 7.14 and in the following ones. The stagnation value is well representative for the turbulence-induced fluctuations around the circumference in the attached region. In the wake the fluctuations drop at around one half. Relying on that, the following simple model $a^{LM}(\varphi)$ can be used to estimate turbulence-induced fluctuations, for any I_u :

$$a^{LM}(\varphi) = \begin{cases} 1 & \varphi \leq \varphi_h \\ 0.5 & \varphi > \varphi_h \end{cases} \quad (7.14)$$

The apex (LM) stands for load model. According to that, the intensity of pressure fluctuations varies along the circumference: it is constant before separation and drops to 50% in the wake.

The red dotted curve “0.85-tot” in Figure 7.14 represents the ratio $\sigma_p(\varphi) / \sigma_{p,0^\circ}$, where the suffix “tot” means “without subtraction of body-induced fluctuations”. It shows that a considerable contribution of body-induced fluctuations has been removed by the model, although the red curve (namely 0.85) still appears to be higher than 1 before separation. The reason is due to some body-induced contributions which are correlated to turbulent properties of the incoming flow and cannot be removed through tests in

smooth flow. These contributions are mainly at the flanges of the cylinder. In any case, the departure from 1 is neglected in the proposed simplified model (equation (7.14)).

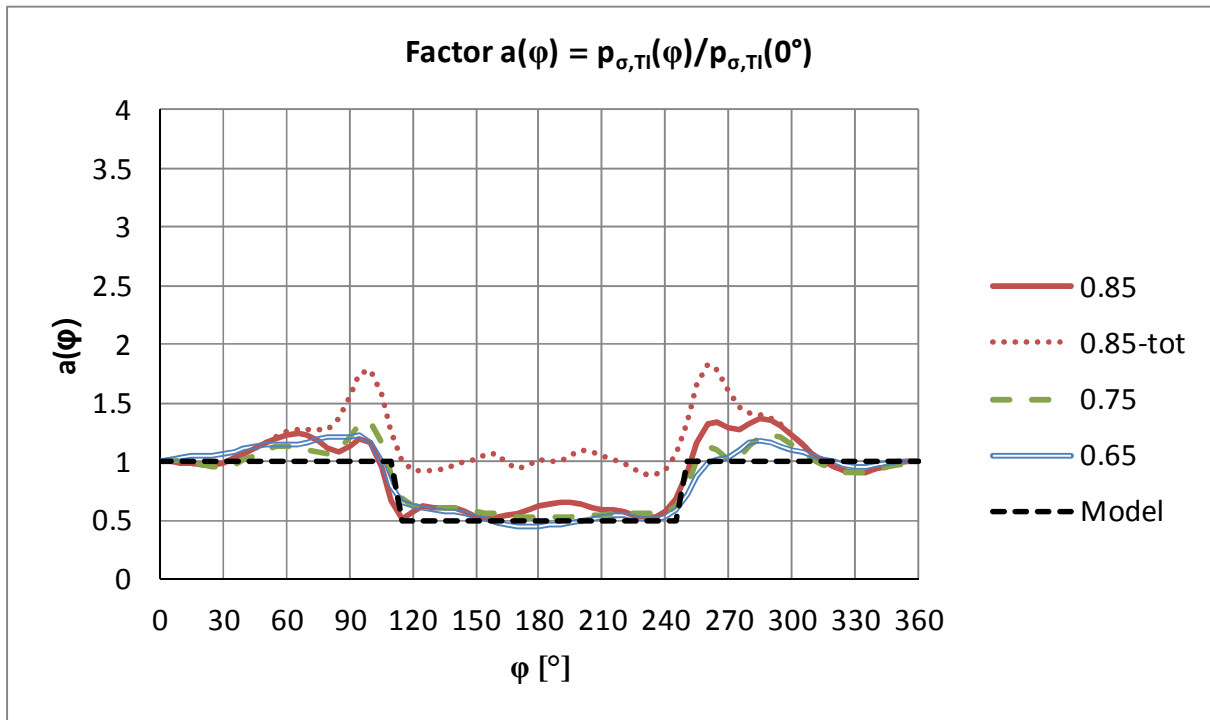


Figure 7.14 Factor $a(\varphi)$ for modelling turbulence-induced pressure fluctuations (highest levels)

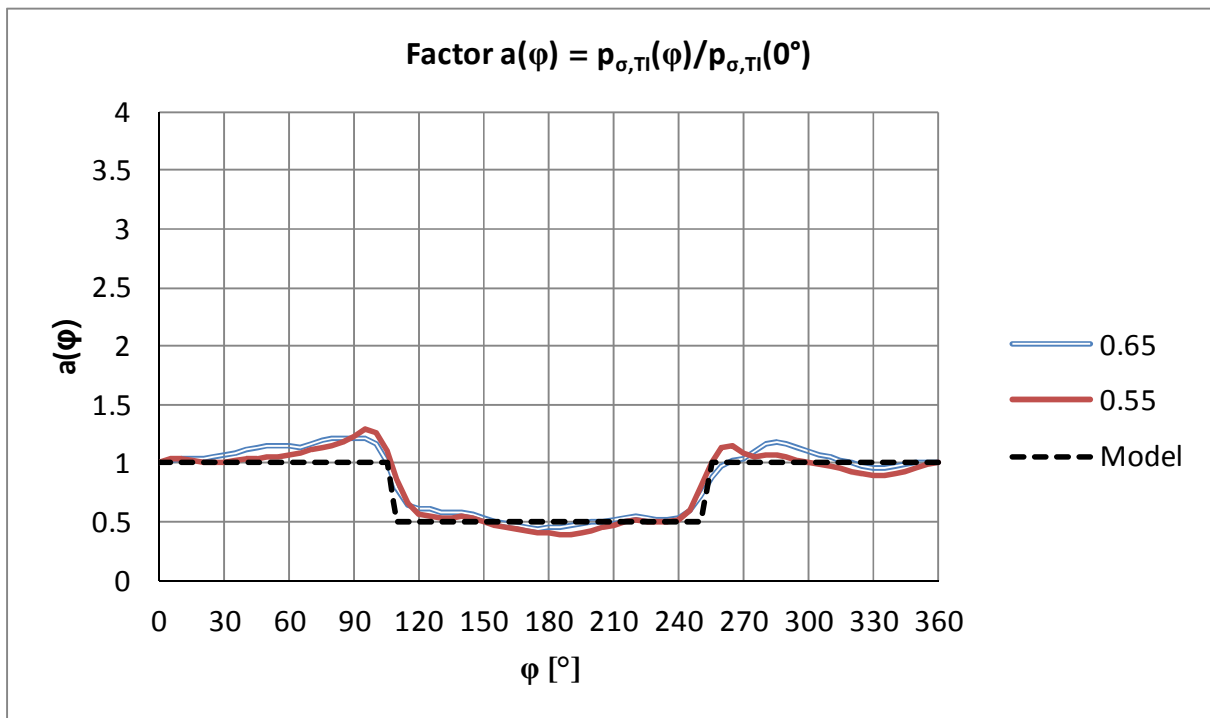


Figure 7.15 Factor $a(\varphi)$ for modelling turbulence-induced pressure fluctuations (intermediate levels)

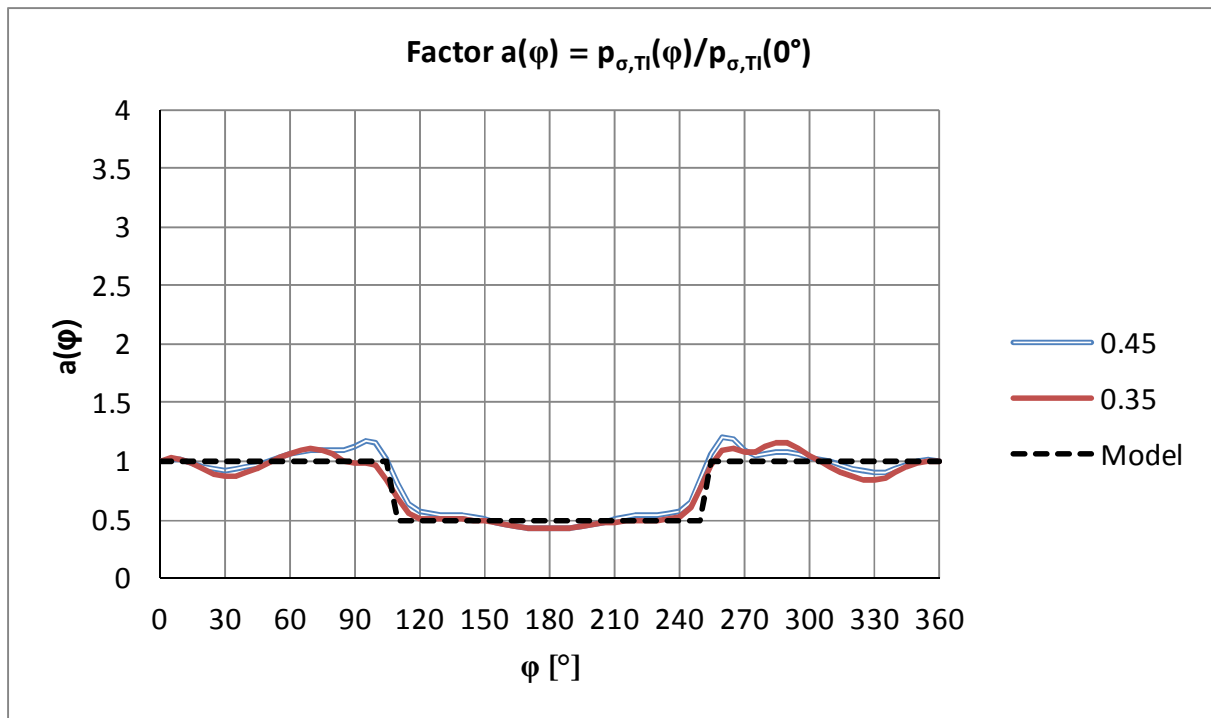


Figure 7.16 Factor $a(\varphi)$ for modelling turbulence-induced pressure fluctuations (low levels)

The comparison with results in literature is a proof of validity of the model, despite its approximations. In particular, similar results are obtained in full-scale data at transcritical Re by Pröpper (1977, fig. 8.8) on cooling towers. In that case, the contribution of vortex separation is low, so that the predominant contribution is turbulence-induced.

A further comment regards the linear extrapolation of the variances at $I_u^2 = 0$ in Figure 7.12 and Figure 7.13. It was an inevitable choice, since only two points per level at different I_u were available at each angle. However, the choice resulted to be rather reasonable. As a proof, the height-dependent variances at stagnation ($C_p, \sigma^2(z) \approx C_p, \sigma_{\text{TI}}^2(z) v c$) are plotted as a function of I_u^2 in Figure 7.17. It shows that a linear relationship, whose extrapolation approximately crosses the origin of axes, is rather correct. The points at the highest turbulence intensity represent pressures on the tower at low levels ($z/H < 0.20$). The reason for which I_u is constant is the presence of the smooth collector roof (Figure 4.8). In any case, at $z/H < 0.20$ the model fails. The reason is that the horseshoe vortex system and the base vortices vary with the free-flow structures and the extrapolation at $I_u = 0$ is strongly non-linear.

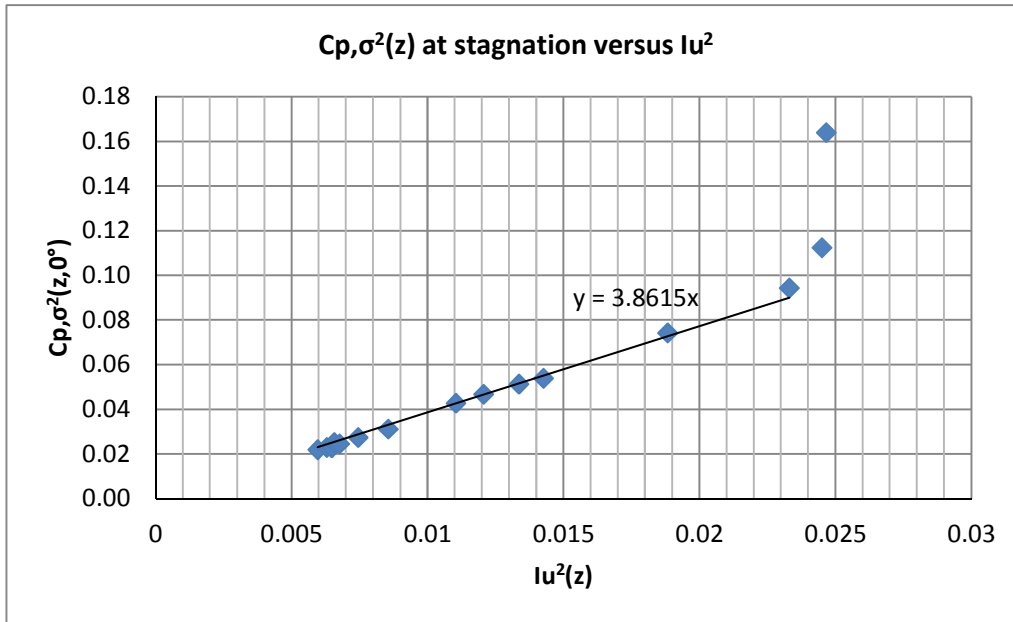


Figure 7.17 Variances C_{p,σ^2} at stagnation versus I_u^2 : a linear relationship (WiSt data)

So far, the factor $a(\varphi)$ has allowed to calculate the turbulence-induced fluctuations around the circumference provided their value at stagnation. Then, the latter can be calculated from the turbulence intensity of the incoming flow. This allows to generalize the model for any boundary layer condition. A first approach has already been proposed in Figure 7.17. A similar approach is based on the factor $A(z)$, which is the ratio between the intensity of pressures at stagnation (the turbulence-induced contribution, namely $I_{p, TI}(z)$) and the intensity of turbulence $I_u(z)$:

$$A(z) = \frac{I_{p, TI}(z)}{I_u(z)} \quad (7.15)$$

The intensity of pressures at stagnation $I_{p, TI}(z)$ is approximately equal to the standard deviation of the pressure coefficient at 0° , being $p_m(z, 0^\circ)$ (mean pressure) approximately equal to the mean velocity pressure $q_m(z)$ (because $C_p(z, 0^\circ) \approx 1$) and $C_{p, \sigma_{TI}}(z, 0^\circ) \approx C_{p, \sigma}(z, 0^\circ)$, as explained by equation (7.16).

$$\begin{aligned} I_{p, TI}(z) &= \frac{p_{\sigma, TI}(z, 0^\circ)}{p_m(z, 0^\circ)} = \frac{p_{\sigma, TI}(z, 0^\circ)}{C_p(z, 0^\circ) q_m(z)} \approx \\ &\approx \frac{p_{\sigma, TI}(z, 0^\circ)}{q_m(z)} = C_{P, \sigma, TI}(z, 0^\circ) \approx C_{P, \sigma}(z, 0^\circ) \end{aligned} \quad (7.16)$$

Therefore:

$$A(z) \approx \frac{C_{P,\sigma}(z,0^\circ)}{I_u(z)} \tag{7.17}$$

The coefficient $A(z)$ calculated on the basis of WiSt results is approximately constant along the height, as shown in Figure 7.18. Its mean value is around 1.93, which is approximately the square root of the slope coefficient of the equation $y = 3.8615$ in Figure 7.17. Only close to the ground ($z/H \leq 0.20$) is the ratio $A(z)$ higher than twice the turbulence intensity, due to the horseshoe vortex system, as previously mentioned with regard to Figure 7.17. Numerical values are reported in Table 7.7. The value $A^{LM}(z) = 2$, on the safe side, can be assumed by the designer without any significant overestimation (see section 7.3). It means that the intensity of pressure at stagnation is about twice the turbulence intensity of the flow.

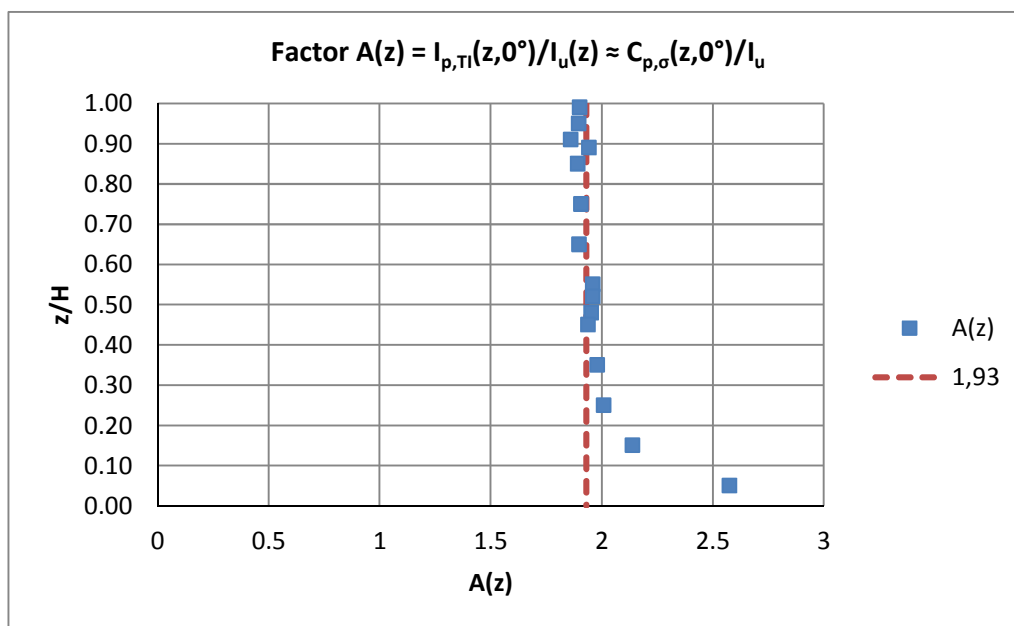


Figure 7.18 Factor $A(z)$

Table 7.7 Factor $A(z)$ and simplified load modelling $A^{LM}(z)$

z/H	WiSt		
	I_u	$C_{p,\sigma}(z,0^\circ)$	$A(z) \approx C_{p,\sigma}(z,0^\circ)/I_u$
0.99	0.0772	0.1469	1.9016
0.95	0.0794	0.1506	1.8970
0.91	0.0806	0.1499	1.8609
0.89	0.0811	0.1578	1.9443

0.85	0.0823	0.1557	1.8917
0.75	0.0863	0.1646	1.9067
0.65	0.0925	0.1757	1.8985
0.55	0.1052	0.2061	1.9598
0.52	0.1099	0.2154	1.9599
0.48	0.1156	0.2259	1.9532
0.45	0.1195	0.2317	1.9394
0.35	0.1373	0.2719	1.9809
0.25	0.1527	0.3068	2.0095
0.15	0.1566	0.3349	2.1392
0.05	0.1571	0.4046	2.5761
Simplified load modelling: $A^{LM}(z) = 2$			

Under the basic assumption that body-induced fluctuations are statistically independent on turbulence-induced fluctuations (Hunt, 1975), the former can be evaluated by an experiment in smooth flow. The result of the extrapolation at $I_u = 0$ at all levels, based on WiSt and CRIACIV results, as previously described, is plotted in Figure 7.19. Numerical values can be found in the appendix (Table A.1). Differences between the two sides due to experimental asymmetries have been averaged out. The figure highlights three distinct regions: the tip region, with a strong effect of tip-associated vortices; the two-dimensional region, where the strength of Karman vortex shedding is practically absorbed by the stochastic fluctuation (the curves as $z/H = 0.55, 0.45, 0.35$ are close to zero); the low region with the ground effect.

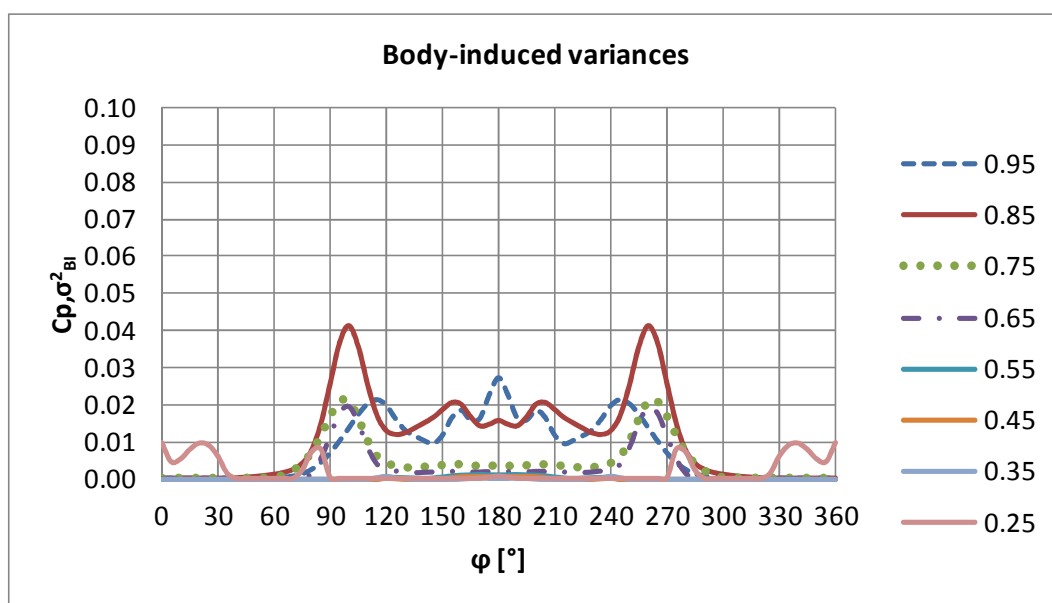


Figure 7.19 Body-induced fluctuations $C_p \sigma_{BI}^2$ all around the tower

7.1.4 Cross-correlation coefficients

The cross-correlation coefficients represent, beside the mean and the rms values, the third piece of information to calculate the quasi-static response of structures to the stochastic wind loading process. They give information about the lack of correlation (size effect). Simple models of cross-correlations of pressure coefficients are proposed in this section, they can be applied for calculation of shell stresses on the solar tower.

The analysis of cross-correlations of pressure coefficients is split up into the vertical and horizontal directions. Their cross product is used to approximate the cross-correlations between points having both horizontal and vertical separation, in case measured data are not available. The goodness of the approximation is discussed at the end of the section and later on in terms of the structural response. This simplification allowed to reduce significantly the total number of simultaneous measurements in the experiments, but a further refinement would be advisable for the future (Chapter 8).

Similarly, since force coefficients are calculated by integration of pressures at each level, the evaluation of their cross-correlations required simultaneous measurements of each level with all the other ones. Simultaneous data of forces at all levels are not available, therefore it is not possible to develop a complete model for cross-correlations of drag and lift coefficients to be used in beam-like calculations. Therefore, cross-correlations of forces are used whenever available for a deeper insight and clarification of pressure cross-correlations.

Vertical cross-correlation coefficients

The vertical correlation of pressures at stagnation depends on the turbulence structure of the incoming flow. As before, it would be important to generalize the results obtained for the specific turbulence condition tested in the wind tunnel to other turbulence conditions. For this purpose, it is mainly referred to results at WiSt, since measurements of both cross-correlations of pressures and velocities are available there. According to Teunissen (1970) the vertical correlation coefficients of wind velocities (along-wind component) in the atmospheric boundary layer have an exponential decay along the height:

$$\rho_u(\Delta z) = e^{-C_{uu} \Delta z} \quad (7.18)$$

By definition, the vertical integral length scale of turbulence (L_{uz}) is given by integration:

$$L_{uz} = \int_0^{\infty} \rho_u(\Delta z) d(\Delta z) \quad (7.19)$$

Therefore $C_{uu} = 1/L_{uz}$. If also the vertical correlations of pressures ($\rho_p(\Delta z)$) can be described by an exponential curve, then the vertical decay of pressure fluctuations can be related to the vertical decay of turbulence fluctuations. In general, it is:

$$\rho_p(\Delta z) = e^{-C_{pp} \Delta z} \quad (7.20)$$

L_{pz} is the pressure correlation length:

$$L_{pz} = \int_0^{\infty} \rho_p(\Delta z) d(\Delta z) \quad (7.21)$$

Similarly, $C_{pp} = 1/L_{pz}$ and a factor “c” is introduced to describe the relationship between L_{uz} and L_{pz} :

$$\rho_p(\Delta z) = e^{-\Delta z / L_{pz}} = e^{-c \cdot \Delta z / L_{uz}} \quad (7.22)$$

where:

$$c = \frac{L_{uz}}{L_{pz}} \quad (7.23)$$

However, provided the information regarding the vertical correlation of turbulence (L_{uz}), the relationship between L_{uz} and L_{pz} is in general unknown. It further depends, according to Hunt (1975), on the diameter of the structure. For example, for a circular cylinder ($L_{uz}/D = 0.2 \div 0.5$) Hunt finds $L_{pz}/L_{uz} = 1.5 \div 2.5$ (the factor c is the inverse value). According to him, the correlation length of pressure fluctuations (L_{pz}) is larger than the integral scale of turbulence L_{uz} because the vortices which are smaller than the diameter of the structure pile up at stagnation. This creates more similarity in the pressure fluctuations field.

In the case of the solar tower tested in the WiSt wind tunnel, the vertical integral length scale of the velocity fluctuation varies along the height around 200 mm (see Table 4.2). It is then of the same order of the tower diameter. Two representative levels at small and large heights ($z_{ref} = 100$ mm, upwards direction; $z_{ref} = 700$ mm, downwards direction) are reported in Figure 7.20, in view of a direct comparison with the pressure correlations. The vertical cross-correlations of pressures at stagnation are fitted with a negative exponential curve. Figure 7.21 reports L_{pz} at two levels, selected as the most suitable ones for the direct comparison with Figure 7.20.

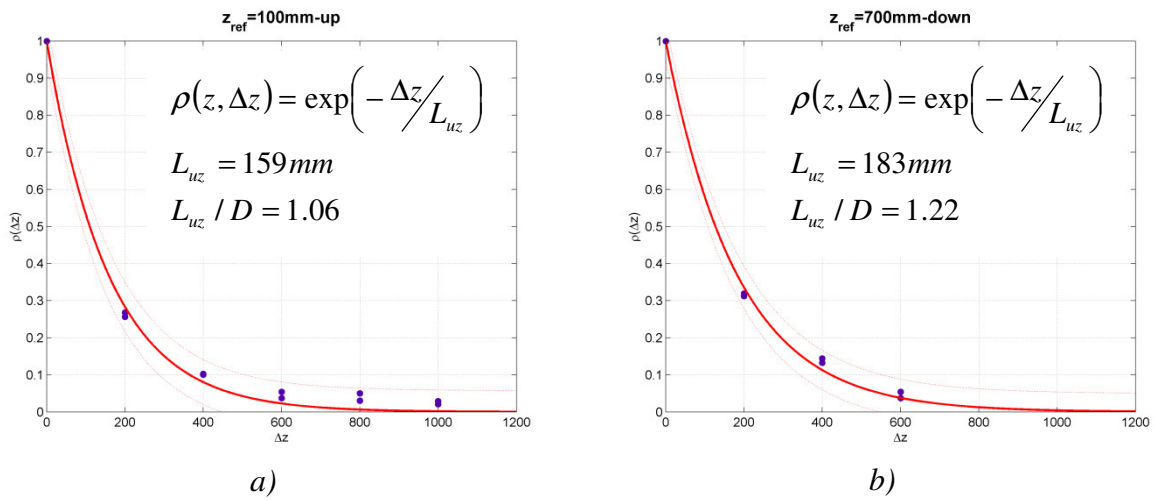


Figure 7.20 Vertical correlation coefficients of wind velocity (u -component)
 a) $z_{ref} = 100$ mm (upwards); b) $z_{ref} = 700$ mm (downwards);

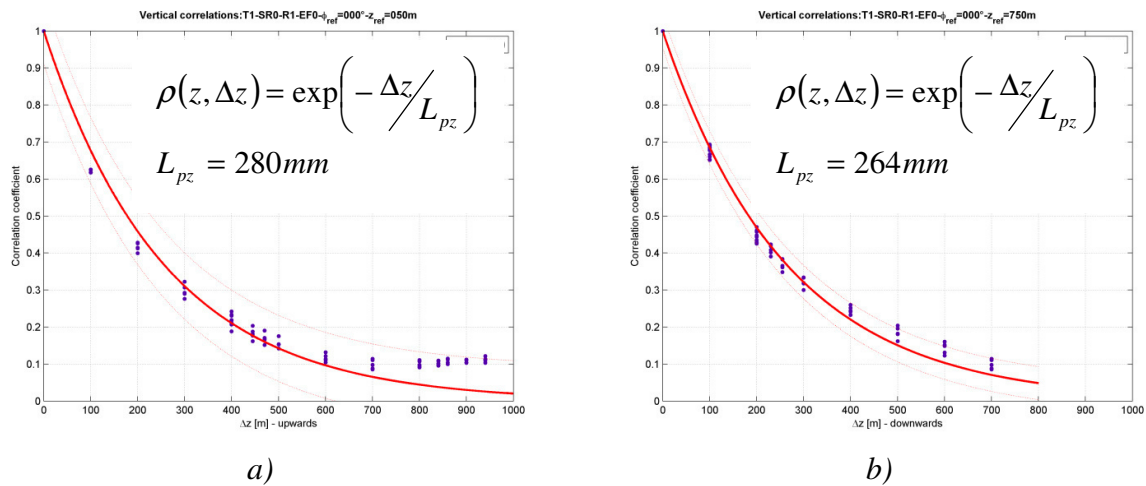


Figure 7.21 Vertical correlation coefficients of wind pressure at stagnation
 a) $z_{ref} = 50$ mm (upwards); b) $z_{ref} = 750$ mm (downwards);

The comparison between Figure 7.20 and Figure 7.21 shows that $L_{pz} > L_{uz}$. It confirms Hunt's theory of the piling up of vortices at stagnation even for integral length scales of turbulence which are comparable to the tower diameter. Then, in order to develop a

general model, a more systematic study is needed at several reference heights and different meridians. It is reported in the following.

In principle, L_{pz} and L_{uz} depend on the direction of movement (Δz upwards, or Δz downwards). However, in view of a simplified model, the correlation coefficients are considered as a function of $|\Delta z|$. Figure 7.22 gives an overview of the pressure correlation lengths in the attached region of the cylinder (i.e. before separation). As said, they are calculated by integration of $\rho(|\Delta z|)$, i.e. assuming independence from the direction of movement. The largest correlation length is the angle $\varphi = 60^\circ$. The figure also plots the integral length scales of the flow L_{uz} . Reference values, averaged along the height, are:

- $L_{uz} \approx 195 \text{ mm}$ ($L_{uz}/D = 195/150 = 1.30$);
- $L_{pz} \approx 285 \text{ mm}$ at $\varphi = 0^\circ$ ($c(0^\circ) = L_{uz}/L_{pz} = 0.68$);
- $L_{pz} \approx 254 \text{ mm}$ at $\varphi = 20^\circ$ ($c(20^\circ) = L_{uz}/L_{pz} = 0.77$);
- $L_{pz} \approx 341 \text{ mm}$ at $\varphi = 300^\circ$ ($c(300^\circ) = L_{uz}/L_{pz} = 0.57$).

Figure 7.23 shows the experimental height-dependent ratio L_{uz}/L_{pz} (the so-called factor “c”, equation (7.23)) at different circumferential angles before separation. The figures shows that the ratio L_{uz}/L_{pz} is different at each angle but it is approximately constant along most of the height.

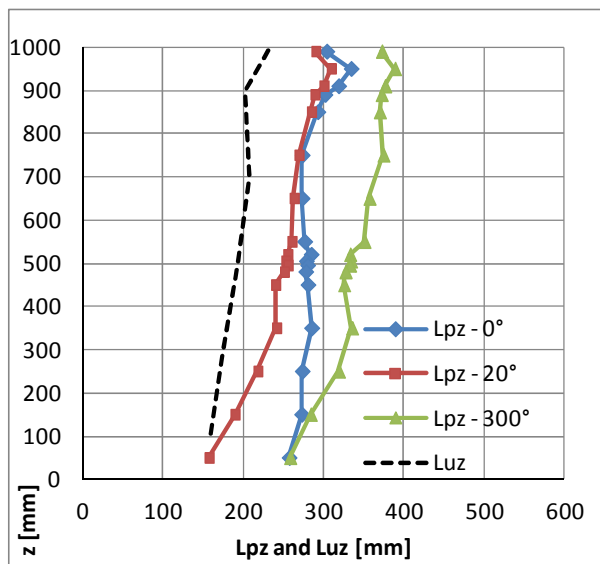


Figure 7.22 L_{pz} and L_{uz} in the attached region before separation, calculated by integration of $\rho(|\Delta z|)$, i.e. assuming independence of direction of movement (WiSt results)

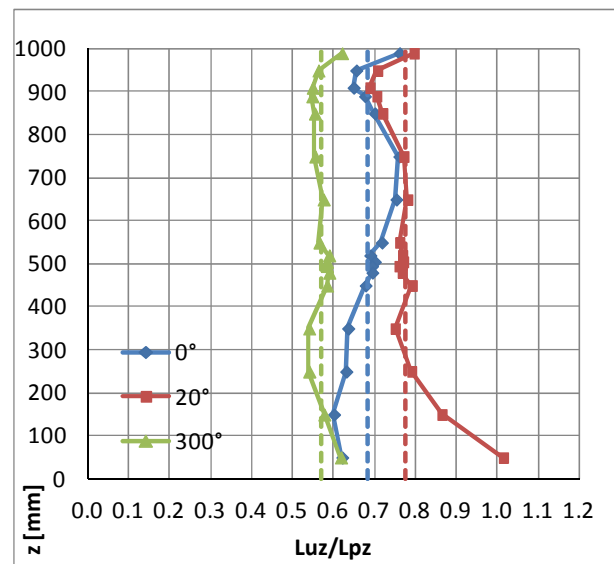


Figure 7.23 Factor $c = L_{uz}/L_{pz}$ (WiSt results)

The cross-correlation coefficients in the wake region drop faster with increasing distance. It would lead to small values of L_{pz} . In fact, at WiSt, the cross-correlation

remains almost constant to a non-zero value, around 0.18, at very large distances of separation (Figure 7.24). Such a constant correlation is not present in the undisturbed flow. The physical reason is probably a big steady vortex in the near-wake, due to the recirculating flow, as discussed in section 6.3 in the comparison with CRIACIV data. From a mathematical point of view, the negative exponential function would force the curve rapidly to zero and would not consider this quasi-asymptotic behaviour, leading to an underestimated value of L_{pz} . A double negative exponential function fits better in the wake (Figure 7.24, red curve). However, in this way the integration of the cross-correlation coefficients from zero to ∞ results in an impressively high value. Therefore, it is decided to calculate a so-called “equivalent correlation length” by integration of the double exponential fitting function along the tower height (from zero to $\Delta z = H$). It can then be used to model the correlations according to equation (7.22). The resulting values of the equivalent correlation lengths for the wake region are reported in Figure 7.25. Apart from the departure in the tip region, it can be approximately said that:

- $L_{pz} \approx 260 \text{ mm}$ at $\varphi = 120^\circ$ ($c(120^\circ) = L_{uz}/L_{pz} = 0.75$);
- $L_{pz} \approx 340 \text{ mm}$ at $\varphi = 180^\circ$ ($c(180^\circ) = L_{uz}/L_{pz} = 0.57$);

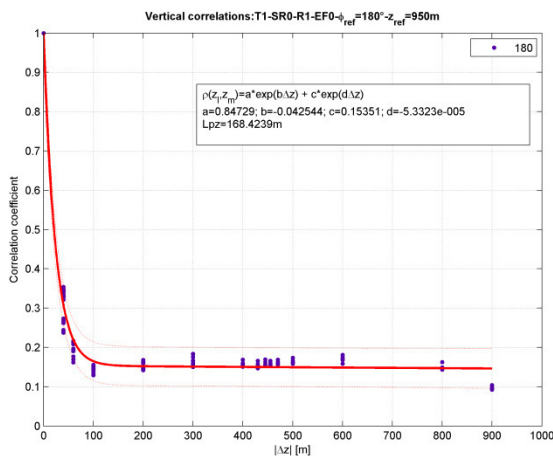


Figure 7.24 $\rho(0.95H, |\Delta z|)$ double negative exponential fitting curve, in order to fit the almost constant correlation at large distances (WiSt results)

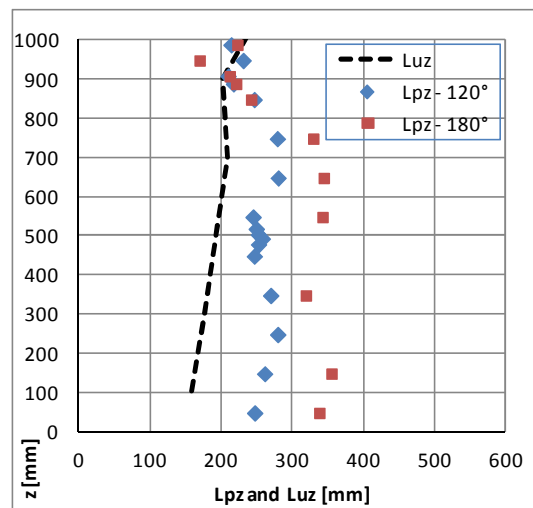


Figure 7.25 Equivalent L_{pz} in the wake region, calculated by integration along the tower height (WiSt results)

It results that around the circumference there is a certain variability of L_{pz} . In any case, provided the values of L_{pz} at different angles, the vertical cross-correlations are easily modelled by applying equation (7.22), i.e. by a negative exponential function.

In order to estimate the goodness of this modelling, Figure 7.26 plots the measured cross-correlations by using the dimensionless x-axis $|\Delta z|/L_{pz}$. The black line is the modeled curve by using a negative exponential function according to equation (7.22). In the dimensionless plane it is just $\rho(|\Delta z|/L_{pz}) = \exp(-|\Delta z|/L_{pz})$. It can be seen (Figure 7.26a), that the use of a negative exponential function provides a good estimation of the vertical cross-correlations in the attached region of the cylinder before separation. In the wake region (Figure 7.26b) the scatter is bigger, also because of the quasi-asymptotic behaviour at large distances. In any case, Figure 7.26b, compared to Figure 7.24, shows that this behaviour is partially removed by the use of the “equivalent” L_{pz} , as previously defined. However, at short distances it tends to overestimate the cross-correlations.

In any case, the goodness of the proposed stochastic model for vertical correlations does not depend on the scatter in the approximation of the load, rather on the effect on the response. A beam-like calculation (through the co-variance method) estimated that an even high non-zero drag correlation at large distance (e.g. 0.3) would produce an increase of around 3% of the base peak bending moment. This increase is further reduced by introducing the equivalent (larger) L_{pz} . Therefore, it can be concluded that a simple negative exponential function according to (7.22) can be used without any significant underestimation.

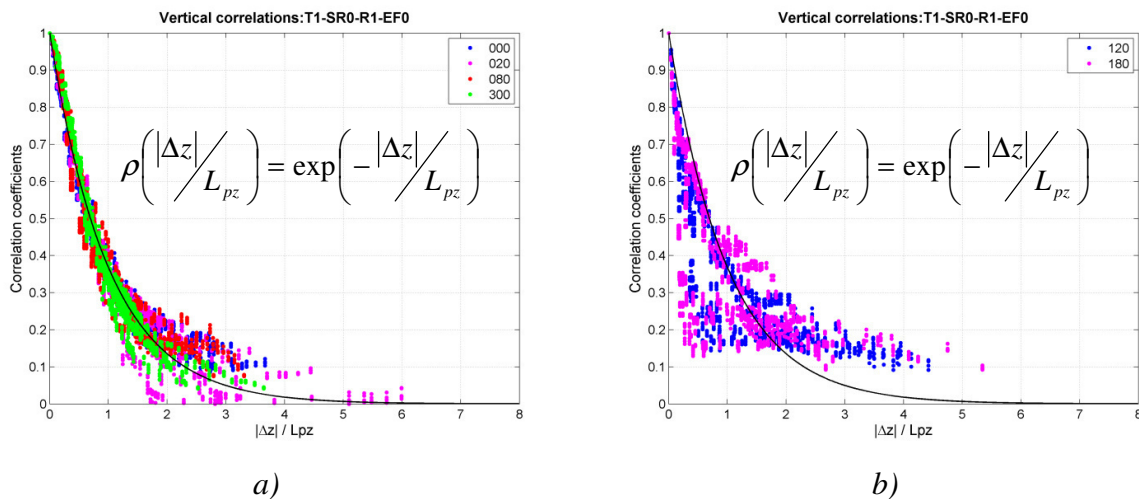


Figure 7.26 Modelling of vertical cross-correlations by negative exponential function
a) attached region before separation; b) wake region

In order to generalize the model to any turbulent boundary layer flow, which is characterized by a certain profile of $L_{uz}(z)$, L_{pz} should be evaluated from L_{uz} by using the factor “c” and equation (7.23). On the basis of WiSt results, such factors around the circumference are summarized in Table 7.8.

A further simplification can be introduced in the load model (LM) by neglecting the circumferential variation of L_{pz} . This is reported in the last row of Table 7.8. Although the load input might be rather approximated, the calculation of the response did not show any significant change. Because of that, the approximation (LM) is recommended.

Table 7.8 The factor “c” to relate L_{pz} and L_{uz}

Luz [mm] - WiSt	φ [°]	L_{pz} [mm] - WiSt	$c = L_{uz}/L_{pz}$
195	0	285	0.68
	20	254	0.77
	60	341	0.57
	80	296	0.66
	120	260	0.75
	180	340	0.57
(LM) Load Model approx.	0-360		2/3

In conclusion, in the general case the vertical cross-correlations of pressures can be modelled as:

$$\rho_p(z, |\Delta z|) = e^{-\left(\frac{2}{3}\right) \frac{|\Delta z|}{L_{uz}(z)}} \quad (7.24)$$

Horizontal cross-correlation coefficients

The horizontal correlation coefficients around the circumference are governed by the mean flow pattern, while the structure of incoming turbulence is of secondary importance (Pröpper, 1977). Therefore, the first parameter to describe the cross-correlation matrix at a certain level is the separation angle φ_h (see Table 7.5).

By definition, $\rho(\varphi_1; \varphi_2) = \rho(\varphi_2; \varphi_1)$, therefore the correlation matrix is symmetric with respect to the main diagonal, whose values are equal to 1. Moreover, due to the symmetry between the two sides of the cylinder, the matrix is also symmetric with respect to the secondary diagonal. The description of one quarter of the matrix will then contain all the necessary information⁷.

⁷ In case of rings, instead, the presence of a bubble on only one side of the cylinder breaks the symmetry with respect to the secondary diagonal.

The correlation coefficients depend on the reference position and on the direction of movement. The reference position is classified in two groups: points before separation ($\varphi < \varphi_h$) and points after separation ($\varphi \geq \varphi_h$). The direction of movement is either downstream or upstream. The cross-correlations of stagnation and of rear stagnation (i.e. 0° and 180°) are the only ones which are symmetric around the circumference.

The circumferential correlations of the stagnation point with all the other points around the circumference resemble the mean pressure distribution (Figure 7.27). Stagnation and maximum suction have a strong negative correlation; stagnation and wake area have small negative correlations. It means that the fluctuations around the circumference appear to be organized by the mean flow and a considerable portion of them may be understood as a “breathing” of the mean flow.

The correlations of rear stagnation prove that the correlation between points in the wake and points before separation is not equal to zero. There is a relatively strong correlation between the maximum lateral suction and the wake ($\rho(180^\circ, 70^\circ) \approx 0.6$) and even at 0° the correlation is not zero: $\rho(180^\circ, 0^\circ) = -0.2$. These values are in agreement with Pröpper’s results on cooling towers (Pröpper, 1977, figure 8.14). Therefore, Hunt’s assumption of statistically independent pressure fluctuations due to incoming turbulence and vortex shedding is not completely confirmed.

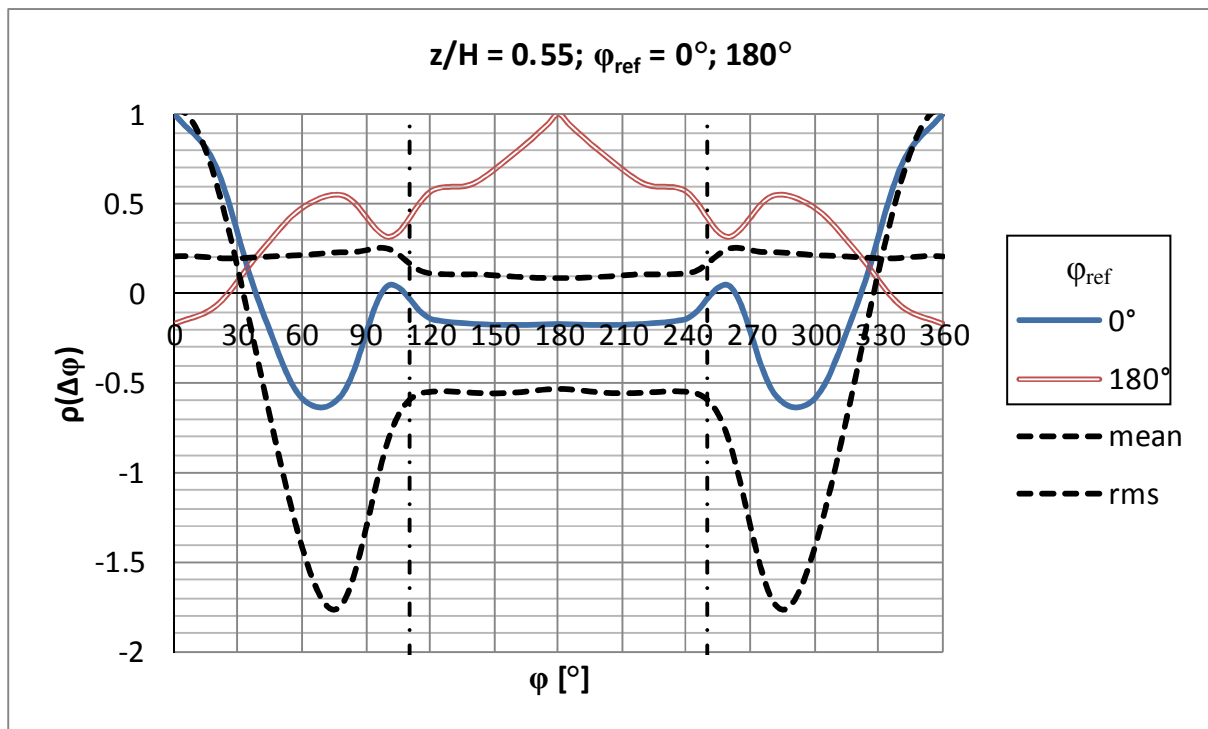


Figure 7.27 Cross-correlation coefficients $\rho(0^\circ, \Delta\varphi)$ and $\rho(180^\circ, \Delta\varphi)$ at $z/H = 0.55$

Figure 7.28 plots the circumferential cross-correlations at $z/H = 0.55$ when the reference position (listed in the legend, corresponding to $\rho=1$) is before separation. The downstream movement from the reference position has to be read in the graph from left to right, while the direction towards left refers to the upstream direction of movement. Similarly, Figure 7.29 plots the circumferential cross-correlations at $z/H = 0.55$ when the reference position is in the wake. All these pieces of information are then synthesized together in the correlation matrix in Figure 7.30.

Let us consider the cross-correlations to a reference angle φ_{ref} before separation (Figure 7.28). A significant difference between going downstream or upstream the cylinder from the reference position is the extension of the range of the negative correlations. In particular, in the downstream direction there is a weak negatively correlated range, which disappears in a positive plateau as the reference position approaches separation. Referring to $\rho(20^\circ, \varphi)$, for example, the negative correlated range lies between $\rho(20^\circ, 60^\circ)$ and $\rho(20^\circ, 100^\circ)$, i.e. $\Delta\varphi = 40^\circ$. The position $\varphi_{\text{ref}} = 60^\circ$ is always positively correlated with the downstream positions. The upstream cross-correlations, instead, drop in a deep negatively correlated area when the two points belong to opposite sides of the cylinder. For example, at $\varphi_{\text{ref}} = 20^\circ$ the negative range with circumferential positions on the other side lies between $\rho(20^\circ, 340^\circ)$ and $\rho(20^\circ, 270^\circ)$, i.e. $\Delta\varphi = 70^\circ$ and the correlation drops till -0.7. The negative correlation between the two sides of the cylinder is marked by the dark blue on the upper right-hand-side corner in Figure 7.30 (or, similarly, the lower left-hand-side corner).

Along the height, the spanwise variation of the circumferential correlations follows the same organization of the mean flow. The following three main regions are detected along the height (Table 7.5):

- tip region ($z' < 2D$ from the top, i.e. $z' < 0.3H$ in the case study), Figure 7.31;
- normal region ($z/H > 0.5$ and $z' > 0.3H$), Figure 7.30
- low region ($z/H < 0.5$), Figure 7.32;

For simplicity, only one correlation matrix is proposed for the low region (Figure 7.32), that is an envelope of values on the safe side. Instead, the tip region can be further subdivided as follows:

- tip region ($z' < 2D$):
 - a) $z' < 0.3D$ (Figure 7.31a)
 - b) $0.3D \leq z' \leq 0.5D$ (Figure 7.31b)

c) $0.5D \leq z' \leq D$ (Figure 7.31c)

d) $D \leq z' \leq 2D$ (Figure 7.31d)

Numerical values of correlation matrices for calculations are reported in the appendix (section 10.1).

Correlations between points with horizontal and vertical separation

The cross-correlations between points with horizontal and vertical separation ($\Delta\varphi$ and Δz) are approximated by the cross-products (equation (7.25)). The approximation is unavoidable, because the streamlines of the flow descend while flowing round the body. These movements are even enhanced by the velocity gradients in shear flow. Therefore, it is generally not possible to split the correlation into a height-dependent and a circumferential distribution. The topic is also addressed in Kasperski&Niemann (1988). However, the three dimensional correlation field has not been completely measured in the experiments on the tower. Because of that, the use of approximation (7.25) cannot be avoided. Further tests are advisable in the future for refinement of this model.

$$\rho(z_1, \varphi_1; z_2, \varphi_2) \cong \rho(z_1; z_2) \cdot \rho(\varphi_1; \varphi_2) \quad (7.25)$$

Equation (7.25) can be applied in two ways: the vertical correlation can be evaluated at $\varphi = \varphi_1$ and the horizontal correlation at $z = z_2$ or viceversa. Numerically, the results are different, but a general rule does not exist. Therefore, in this work the cross-product was calculated in both ways and the safest result was considered. Whenever measured, $\rho(\varphi_1, z_1; \varphi_2, z_2)$ is compared to its approximated modelling. The modelling results to be mostly on the safe side. Only the cross-correlations in the wake might be underestimated.

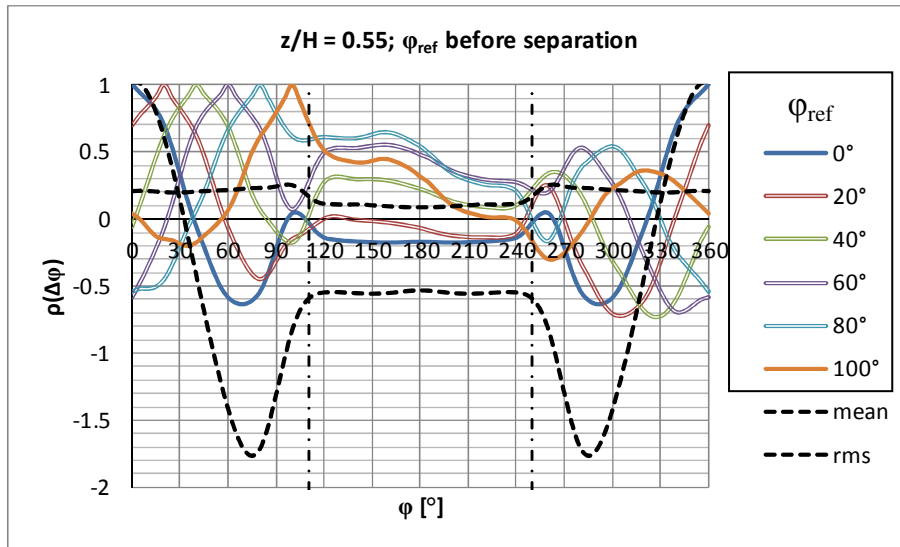


Figure 7.28
Horizontal cross-correlation coefficients at $z/H = 0.55$; φ_{ref} before separation

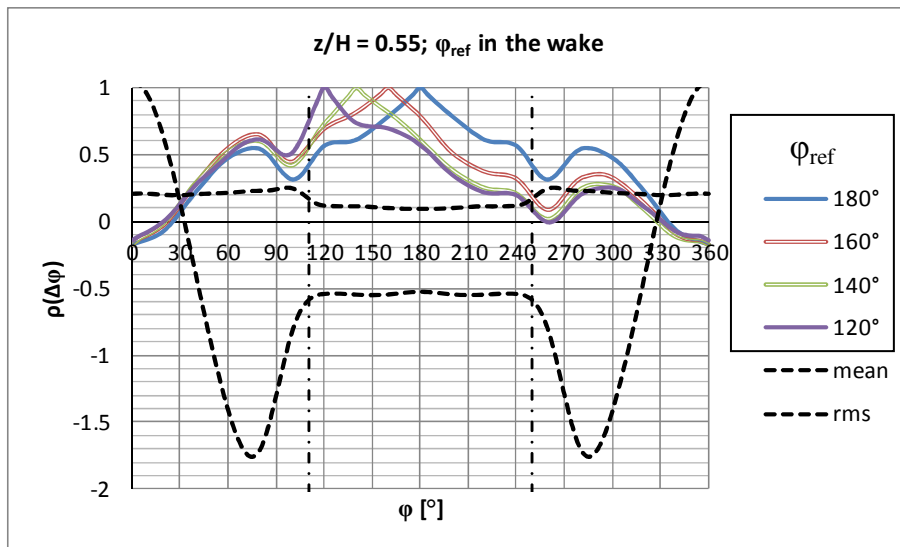


Figure 7.29
Horizontal cross-correlation coefficients at $z/H = 0.55$; φ_{ref} in the wake

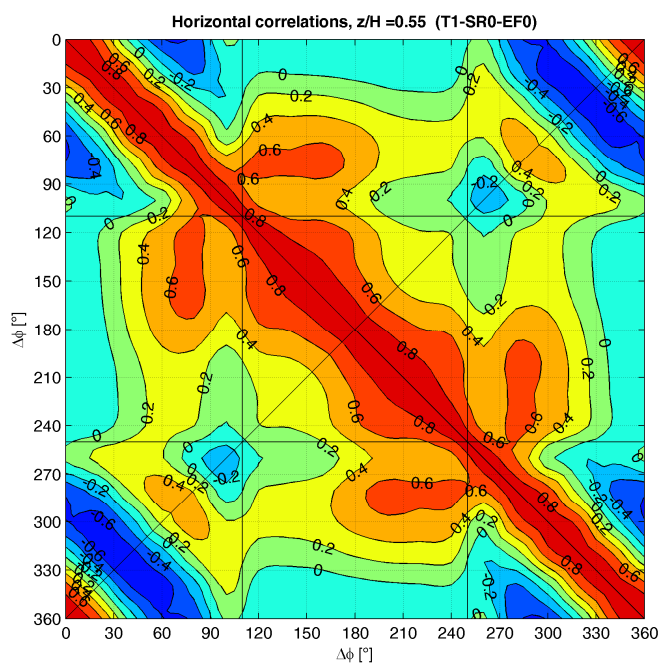


Figure 7.30
Horizontal cross-correlation coefficients at $z/H = 0.55$

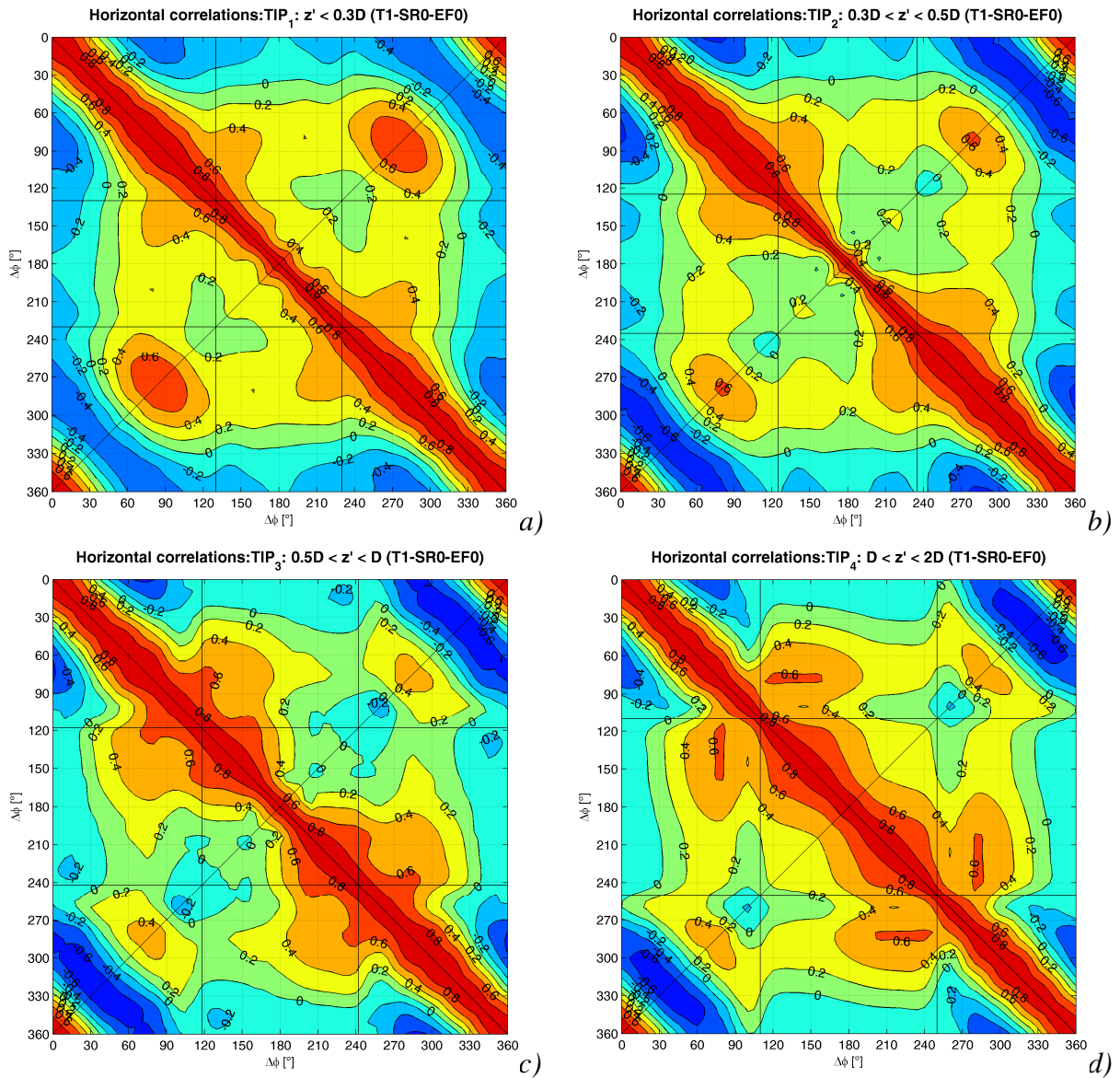


Figure 7.31 a-d) Horizontal cross-correlation coefficients in the tip region ($z' < 2D$)

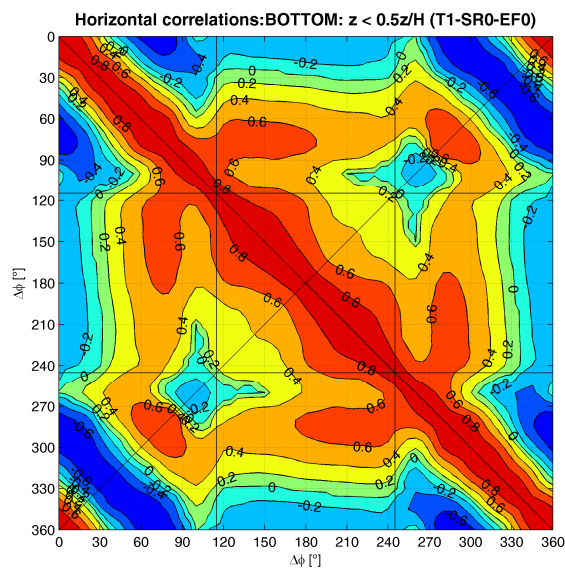


Figure 7.32 Horizontal cross-correlation coefficients in the low region ($z/H < 0.5$)

7.2 The beam response

The beam response of the solar tower is governed by the first natural vibration mode ($n_1 = 0.17$ Hz, Figure 2.20). Being $S_t \approx 0.2$ (Chapter 4), the critical velocity for vortex resonance is about $n_1 D / S_t = 0.17 \cdot 150 / 0.2 = 127$ m/s. This is much higher than the design velocity $U(1000) \approx 55$ m/s (Deaves&Harris model, Figure 2.4), so that resonance between the Strouhal frequency and the (transversal) vibration frequency is not expected. In these conditions, the design is led by the drag force, even though the cross-wind response remains an important contribution.

This section addresses both the along- and the across-wind beam response to the stochastic wind loading process. The background contribution is at first evaluated by the covariance method. Then, it is split up in the frequency domain by using time histories and influence coefficients. This calculation is then repeated by using the software Ansys, including inertial and damping forces. The first sub-section (7.2.1) considers the reference load condition, i.e. without any load modification produced by the rings. The effect of the rings is estimated in the second sub-section (7.2.2).

7.2.1 Quasi-static and dynamic beam response

The beam response of the tower is evaluated in this section by using the reference load condition, i.e. the effect of the rings on the load is not considered. This load configuration corresponds to the experimental results SR0.

At first, the background response to the drag force (σ_B^2), i.e. the response to the excitation that is transmitted without resonant amplification, is estimated without any split into frequencies through the covariance method (Niemann et al., 1996). This method uses statistical averages obtained from measured time series rather than the time series themselves.

$$\sigma_B^2 = \boldsymbol{\eta}^T \cdot \mathbf{cov}_D \cdot \boldsymbol{\eta} \quad \text{and} \quad \mathbf{cov}_D = \mathit{diag}[F_\sigma] \cdot \boldsymbol{\rho}_D \cdot \mathit{diag}[F_\sigma] \quad (7.26)$$

The matrix \mathbf{cov}_D contains the covariances between drag forces at different levels and the vector $\boldsymbol{\eta}$ contains the influence coefficients for a certain effect at a certain cross-section. The covariances can be further split up into the product between rms values and correlation coefficients. The peak value of the bending moments ($M_{D,peak}$) is defined as:

$$M_{D,peak}(z) = M_{D,m}(z) + k_p M_{D,\sigma}(z) \quad \text{where } k_p = 3.5. \quad (7.27)$$

The load data ($C_{D,m}$, $C_{D,\sigma}$ and ρ_D) in the basic load configuration (without rings) and the results are listed in the appendix (Table A.8, Table A.9, Table A.10). A synthetic summary is reported here in Table 7.9 and plotted in Figure 7.33.

The base peak bending moment results in the order of $8.7 \cdot 10^7$ kNm. The calculation does not include the quasi-asymptotic contribution due to the steady recirculation region in the near-wake (Figure 7.24 showed such a contribution in terms of pressure correlations at 180°). This would result in non-zero values of the cross-correlations of drag force at large distance. However, it has been estimated that even high asymptotic correlation in the drag to the constant value 0.3 instead of 0 would imply an increase in the base peak bending moment of only 3% (i.e. $M_{\text{peak,base}} = 9.01 \cdot 10^7$ kNm). It is then negligible.

Table 7.9 Quasi-static beam response to drag force (effect of the rings on the load not included)

z [m]	$M_{D,m}$ [kNm]	M_{D,σ^2} [kNm] ²	$M_{D,\text{peak}}$ [kNm]
0	6.45E+07	4.26E+13	8.74E+07
650	9.90E+06	1.45E+12	1.41E+07
750	5.42E+06	4.64E+11	7.80E+06
850	2.06E+06	7.17E+10	3.00E+06
950	2.14E+05	1.25E+09	3.38E+05

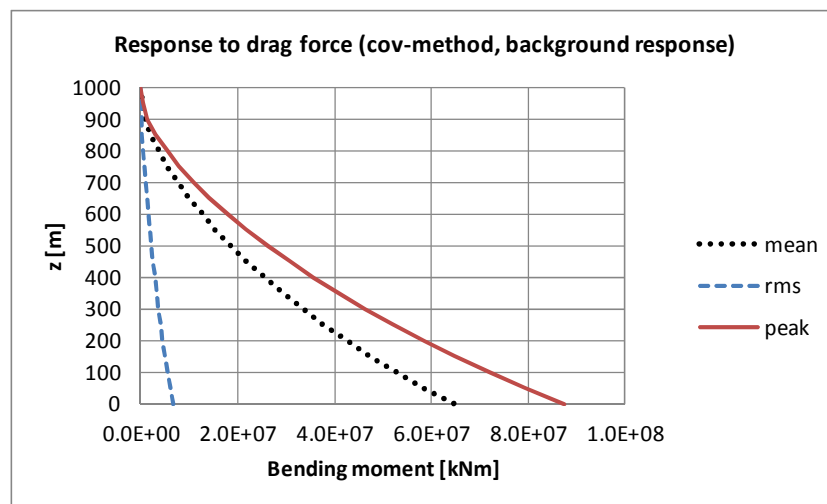


Figure 7.33 Quasi-static along-wind beam response (effect of rings on the load not included)

Then, the across and the along wind beam responses are calculated in the time domain. The background response to the stochastic process is evaluated by the use of measured time histories and influence coefficients, i.e. it is “manually” calculated by applying statically at each time step the influence coefficients of forces along the height. The

influence coefficients for the bending moment at the base are just the heights of the forces. The full dynamic response is calculated with the software Ansys by integration of the dynamic equations of motion (including damping and mass forces) and it shows the dynamic amplification at the first two vibration modes. Simultaneous time histories have to be used in the calculation. They have been measured at four levels (950-850-750-650 m) and - for the purpose of this analysis - all the other time histories are considered fully correlated with them.

The spanwise variation of the tower diameter (Figure 1.13) has been included in the calculation, in order not to underestimate the mass of the structure. The data in the wind tunnel (w_T) are transferred into full-scale (f_S) by scale factors applied on the length ($\lambda_L = L_{FS}/L_{WT}$), on the velocity ($\lambda_U = U_{FS}/U_{WT}$) and consequently on the frequency ($\lambda_F = \lambda_V/\lambda_L$) and on the time ($\lambda_T = 1/\lambda_F$), as explained in section 4.1.2. The reference length scale is the scale of the model (1:1000), because the tower diameter enters the Strouhal number. It is then assumed that the boundary layer in the wind tunnel is scaled similarly.

The main input data of the analyses are:

- $D_{FS}(H) = 150$ m; $D_{WT}(H) = 0.15$ m $\rightarrow \lambda_L = 1000$;
- $U_{FS}(H) = 51.31$ m/s (H&D model, $V_b = 25$ m/s, II terrain cat.); $U_{WT}(H) = 25.07$ m/s $\rightarrow \lambda_V = 2.05$;
- $\lambda_F = 1/488$; $\lambda_T = 488$; it is not too far from the time scale that would have been obtained by comparing T_{ux} in the wind tunnel and T_{ux} in full-scale, even though T_{ux} in full-scale is an uncertain parameter (see section 4.1.2).

In addition, the time domain analysis includes damping and inertial forces (full-transient analysis, Ansys):

- Integration time step = 0.244 s = $(1/n_{\text{sampl}})*\lambda_T = (1/2000)*488 < 1/20n_1 = 1/(20*0.17) = 0.29$;
- Rayleigh damping: $[D] = \alpha[M] + \beta[K]$. The coefficients are calculated assuming modal damping ratios ξ_i equal to 0.01 (corresponding to a logarithmic decrement $\delta = 2\pi\xi \approx 0.06$) at $n_1 = 0.17$ Hz (beam bending mode) and $n_3 = 0.65$ Hz (beam mode with two nodes), according to the formula $\xi_i = \alpha/2\omega_i + \beta\omega_i/2$, where $\omega_i = 2\pi n_i$.

Tapered elements “beam188” in Ansys library have been used in the finite element model of the tower.

Figure 7.34 shows the spectrum of the loading process in the across-wind direction (S_{CL}). Figure 7.35 and Figure 7.36 show the quasi-static and the dynamic responses, respectively, in the across-wind direction. Since the methods and the tools of

calculations are different, the good agreement of results is a further proof of validity. Instead, Figure 7.37, Figure 7.38, Figure 7.39 refer to the along-wind direction. In this regard, it is interesting to note the similarities to the undisturbed flow fluctuations (Figure 4.11).

Figure 7.34 shows the typical two-peaks lift spectra, due to tip-associated vortices. They are shed only in absence of ring beams (basic load configuration), that is the one considered in this section. The critical wind speed for the lower Strouhal number (around 0.07) is very high, so resonance between the structural mode the low-frequency peak will not occur⁸. On the other hand, there will be a quasi-static low frequency oscillation on which the Karman resonance is superimposed. It is then important to quantify the response contribution of the tip-associated vortices.

In the background response, the contribution of the low frequency peak in the bending moment at the base is around 7% (Figure 7.35). If resonance is included (Figure 7.36), the tip-associated vortices increase the variance of the total response of only 3%⁹. Therefore, the contribution of tip vortices in the total response is not so significant. Moreover, Figure 7.36 highlights the dynamic amplification at the base due to the structural vibration modes. The first mode ($n_1 = n_2 \approx 0.17$; $n_1 D/U \approx 0,50$) is the beam bending mode, typical of the solar tower (see section 2.4). The filtering effect of the structure at higher frequencies (mechanical transmittance) is also evident in the graph: the black spectrum goes below the blue one after the resonant peak. The second vibration mode ($n_3 \approx 0.65$; $n_3 D/U \approx 1,9$) is a beam mode with two nodes of inversion in the shape. It is typical for beams but its frequency is not the same as in the shell model of the solar tower. In the shell tower, the second beam mode has a much higher frequency. Many shell-like modes precede it. Therefore, the beam FE model does not reproduce faithfully the real structure, which is not, in fact, a beam. In any case, the vibration frequency of the second beam mode is high and it lies in a frequency range which is not reproduced accurately even in the load. In fact, as explained in section 4.1.3, the damping effect of 1.5m pressure tubes predominates at $n > 200$ Hz (wind tunnel scale), that is $nD/U > 1.2$. This is the cut-off frequency for the spectra.

⁸ In this work, non-linear geometrical effects arising from low frequencies of excitation are not considered, as well as the reduced stiffness due to concrete cracking. Further investigation in the non-linear behaviour is a future outlook.

⁹ In Figure 7.36 the spectra do not seem to decrease to zero as $n \rightarrow 0$. This is a matter of the log plot and Δn . For example, in the “0-qs” curve the first point has coordinate ($nD/U = \Delta nD/U = 0,00146074$; $S_n = 3,57E+11$). The ordinate is more than two orders smaller than the highest magnitude. Moreover, the ordinate is a very small number close to zero once it is divided by the variance, as it is in the dimensionless plot ($3,57E+11/1,61E+14 = 2.2*10^{-3}$).

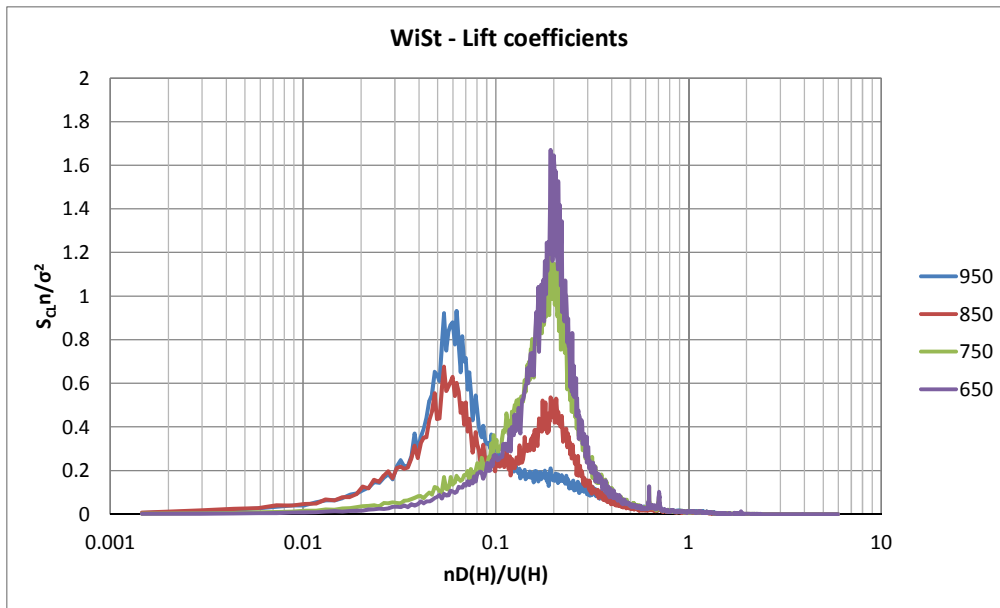


Figure 7.34
Spectra
along the
height of lift
coefficient

(SR0,
effect of the
rings on the
load not
included,
WiSt data)

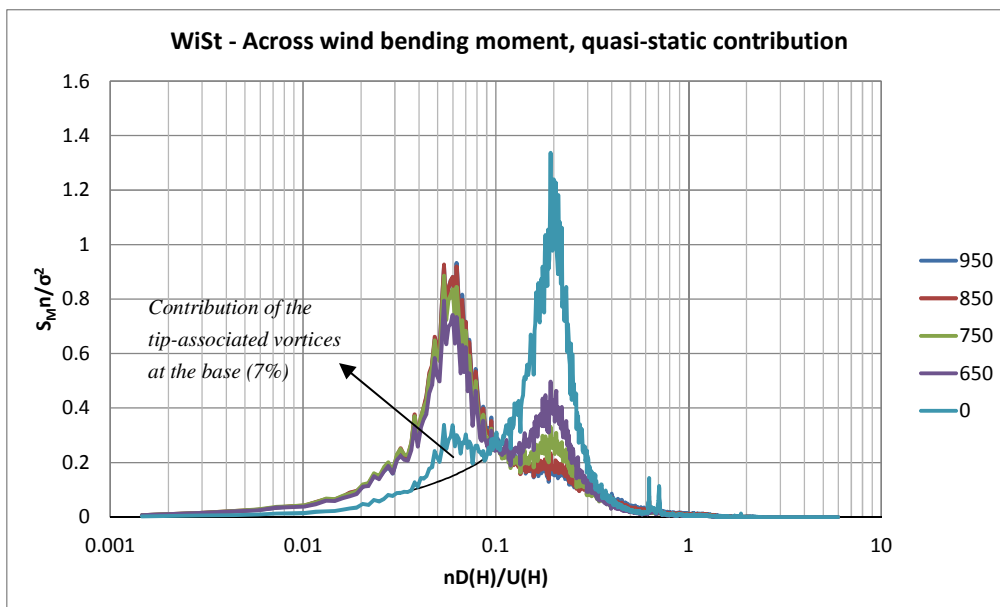


Figure 7.35
Structural
response in
the across-
wind
direction.
Resonance
not included.

(SR0,
effect of the
rings on the
load not
included,
WiSt data)

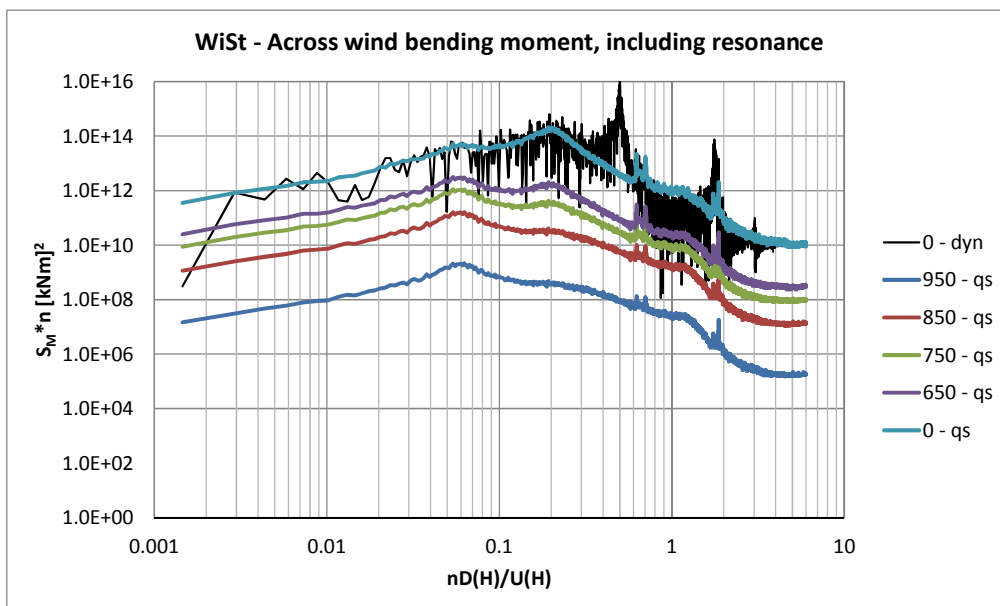


Figure 7.36
Structural
response in
the across-
wind
direction.
Resonance
included.

(SR0,
effect of the
rings on the
load not
included,
WiSt data)

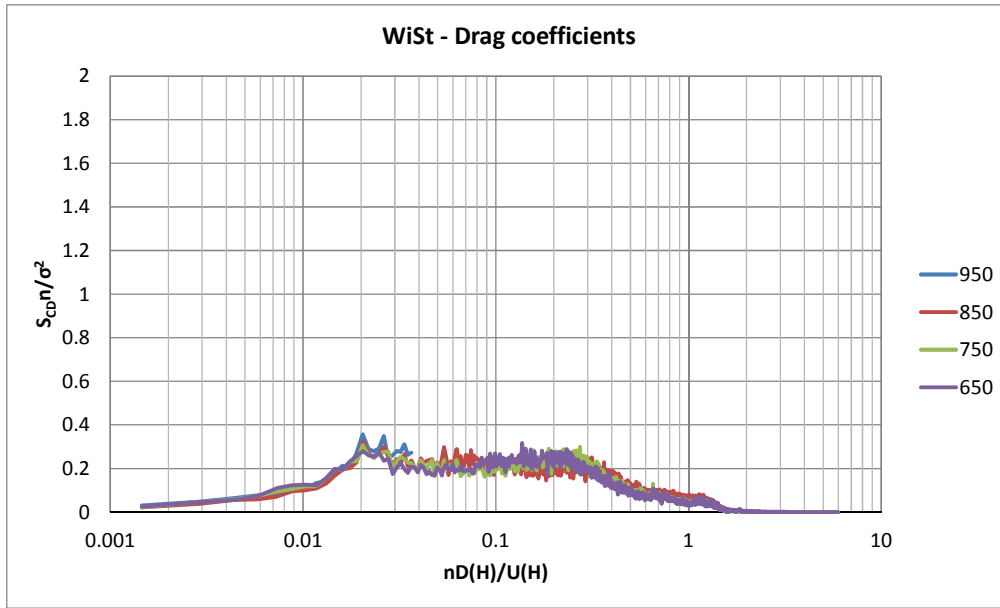


Figure 7.37
Spectra along the height of drag coefficient (SR0, effect of the rings on the load not included, WiSt data)

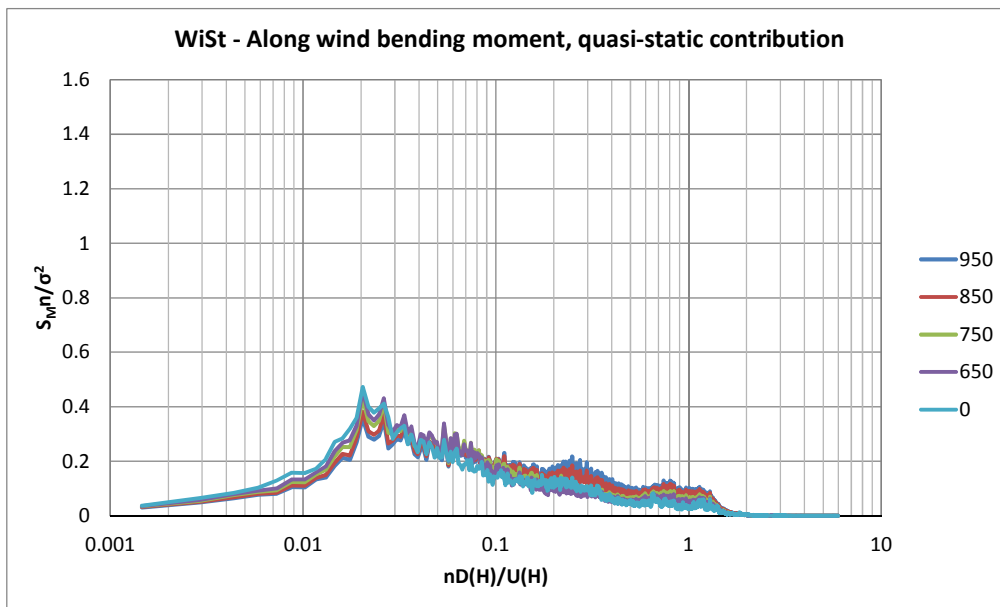


Figure 7.38
Structural response in the along-wind direction. Resonance not included. (SR0, effect of the rings on the load not included, WiSt data)

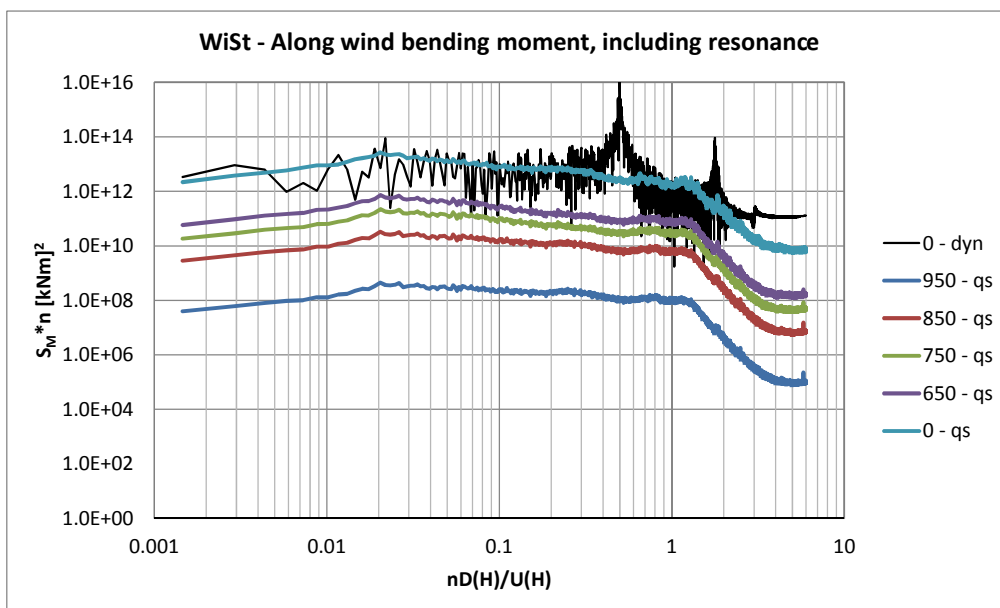


Figure 7.39
Structural response in the along-wind direction. Resonance included. (SR0, effect of the rings on the load not included, WiSt data)

Table 7.10 summarizes the results of the quasi-static and dynamic beam response. Results are separated in the along wind and across wind direction. The variance of the response in the across-wind direction is higher than in the along-wind direction. This can be explained by looking at Figure 4.13. At sufficiently high frequencies, the energy contribution of the v-component of wind speed is higher than the energy contribution of the u-fluctuations.

The effects in the two directions need to be combined in the resultant bending moment, which is a function of the along- and across-wind bending moments:

$$M_{\text{res}} = g(M_D, M_L) \rightarrow M_{\text{res}} = \sqrt{M_D^2 + M_L^2} \quad (7.28)$$

The resultant bending moment can be linearized with Taylor expansion around the middle value; in general it is:

$$\begin{aligned} M_{\text{res}} &\cong g(M_{D,m}, M_{L,m}) + \\ &+ \frac{\partial g}{\partial M_D} \bigg|_{(M_{D,m}, M_{L,m})} (M_D - M_{D,m}) + \\ &+ \frac{\partial g}{\partial M_L} \bigg|_{(M_{D,m}, M_{L,m})} (M_L - M_{L,m}) \end{aligned} \quad (7.29)$$

Therefore, the mean and the variance of the resultant bending moment are:

$$M_{\text{res},m} = g(M_{D,m}, M_{L,m}) = \sqrt{M_{D,m}^2 + M_{L,m}^2} \quad (7.30)$$

$$\begin{aligned} M_{\text{res},\sigma^2} &\cong \left(\frac{\partial g}{\partial M_D} \right)^2 M_{D,\sigma^2} + \left(\frac{\partial g}{\partial M_L} \right)^2 M_{L,\sigma^2} + \\ &+ \left(\frac{\partial g}{\partial M_D} \right) \left(\frac{\partial g}{\partial M_L} \right) M_{D,\sigma} M_{L,\sigma} \rho(M_D, M_L) \end{aligned} \quad (7.31)$$

Where the derivatives are taken at the mean value of the independent variables. If $M_{L,m} = 0$, by linearizing at the first order it results that $M_{res,\sigma^2} \approx M_D,\sigma^2$.

By combining the effects at each time step in the time domain (equation (7.32)), the variance can be exactly evaluated by the resulting time history. It is reported in Table 7.10 and it allows to quantify the approximation by linearization. It can be seen that in the dynamic calculation $M_{res,\sigma_B^2} + \sigma_R^2$ and $M_D,\sigma_B^2 + \sigma_R^2$ differ of only 6% at $z/H = 0$. The difference is higher in the quasi-static calculation (M_{res,σ_B^2} compared to M_D,σ_B^2).

$$M_{res}(t) = \sqrt{M_D^2(t) + M_L^2(t)} \quad (7.32)$$

The dynamic amplification at the base ($z/H = 0$) is 22%, calculated according to equation (7.33):

$$dyn = \frac{M_{res, peak, B+R}}{M_{res, peak, B}} = \frac{M_{D,m} + k_p M_{res, \sigma, B+R}}{M_{D,m} + k_p M_{res, \sigma, B}} \quad (7.33)$$

Table 7.10¹⁰ Beam response without and with resonance (effect of the rings on the load not included, WiSt results)

z	950	850	750	650	0	m		
C_D,σ^2	0.013	0.010	0.007	0.006	0.006		drag coeff.	variance
C_L,σ^2	0.024	0.036	0.021	0.020	0.020		lift coeff.	variance
$M_{D,m}$	2.14E+05	2.06E+06	5.42E+06	9.90E+06	6.45E+07	kNm	along wind	mean
M_{D,σ_B^2}	1.25E+09	8.65E+10	5.20E+11	1.61E+12	5.75E+13	[kNm] ²	along wind	background
$M_{D,\sigma_B^2} + \sigma_R^2$	2.98E+10	5.93E+11	2.94E+12	8.53E+12	1.80E+14	[kNm] ²	along wind	with resonance
M_{L,σ_B^2}	2.31E+09	1.75E+11	1.28E+12	4.06E+12	1.58E+14	[kNm] ²	across wind	background
$M_{L,\sigma_B^2} + \sigma_R^2$	4.24E+10	9.10E+11	4.75E+12	1.40E+13	3.28E+14	[kNm] ²	across wind	with resonance
M_{res,σ_B^2}	1.82E+09	1.02E+11	6.06E+11	1.85E+12	6.32E+13	[kNm] ²	tot. response	background

10 The mean response in Table 7.10 is evaluated by using the same load distribution as in Table 7.9. Instead, the background and the dynamic responses reported in Table 7.10 are evaluated by using simultaneous time histories measured in the wind tunnel. Since only four levels of simultaneous measurements were available ($z/H = 0.95; 0.85; 0.75; 0.65$, 18 pressure taps at each level), for the purpose of this analysis all the other time histories at other levels are considered fully correlated with them. Consequently, a higher value of the stochastic response is obtained. Even from the dynamic point of view, the fact that the time histories are fully correlated at lower levels is an overestimation on the safe side, because the first vibration mode does not have inversions of shape along the height.

$M_{\text{res}}, \sigma_B^2 + \sigma_R^2$	3.06E+10	6.17E+11	3.09E+12	9.02E+12	1.92E+14	[kNm] ²	tot. response	with resonance
---	----------	----------	----------	----------	----------	--------------------	---------------	----------------

In the dynamic calculation, time histories of around 80 minutes (full-scale time, based on the previously mentioned scale factor $\lambda_T = 488$) were applied as input in Ansys. This time window corresponds to 10 s in the acquisition of wind tunnel data. A zoom on a time window of 0.5 s (in the wind tunnel scale), which corresponds to 244 s in full scale, is plotted in Figure 7.40 and in the following ones. The aim of these figures is to study, in the time domain, the vortex separation and the structural vibration, both in the stochastic loading process and in the structural response.

The full-scale period of vortex separation is around 15 s ($S_t D/U \approx 0.2 \cdot 51/150 = 0.068$ Hz). It corresponds to about 0.03 s in the wind tunnel. Therefore, about 16 vortex shedding periods occur in the time window of Figure 7.40. This oscillation is evident in the time history of the loading process (Figure 7.40), superimposed to the stochastic contribution due to turbulence fluctuations. In order to highlight vortex separation, the time histories have been filtered with a passband filter around the Strouhal peak (nD/U between 0.18 and 0.22). The blue lines represent the filtered time histories.

In particular, Figure 7.40 plots the lift coefficient at a representative level ($z = 650$ m). Figure 7.41 plots the corresponding effect, i.e. the across-wind bending moment, at the same level, both without and with filtering around Strouhal (magenta and blue lines, respectively). The magenta line highlights, in the response, the dominant oscillation at the frequency of the structural vibration: the structure is, itself, a filter. While the vortex shedding period is about 0.03 s in the wind tunnel scale, the structure vibrates with a shorter period, about 0.01 s ($1/n_1/\lambda_T = 1/0.17/488$). It results that about 40 cycles occur in the time window of Figure 7.41 (that is 0.5 s).

It is interesting to analyze the response that there would be in conditions of resonance between vortex separation and structural vibration frequency (Figure 7.42). This is not a design condition, resonance has been imposed just for the purpose of this analysis by reducing the Young modulus of the material and increasing the wind speed. Resonant conditions are obtained at $U_H = 74$ m/s and reduced stiffness so that $n_1 = 0.10116$ Hz ($n_1 D/U = 0.20 = S_t$). Figure 7.42 proves that in this condition stochastic properties of the load are completely filtered out in the response by the resonant vibration. The magnitude of amplitudes is also much higher (one order of magnitude, if compared to Figure 7.41). The cross-correlation functions in the resonant condition assume a value close to 1 along the whole height and decrease slowly in time.

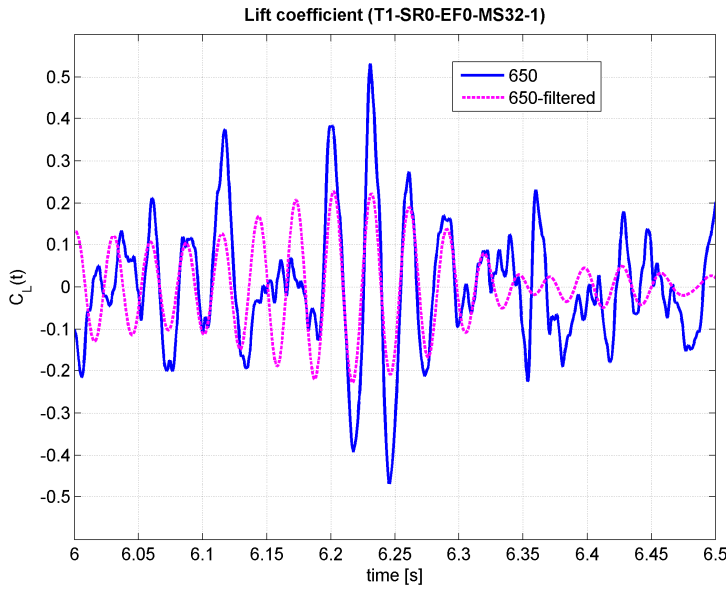


Figure 7.40 Stochastic loading process: time history of C_L , level 650 m. (SR0, effect of the rings on the load not included, WiSt data)
Blue line: bandpassfilter around $S_t(0.18-0.22)$
x-axis in wind tunnel scale

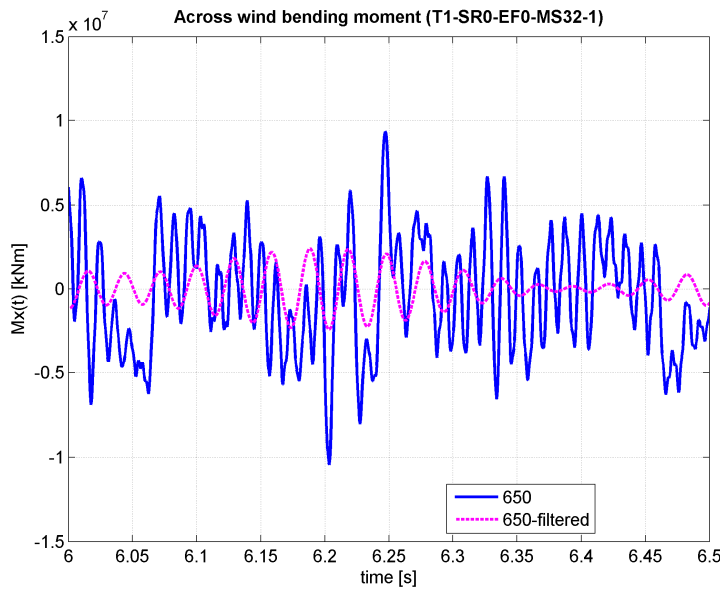


Figure 7.41 Structural response to the stochastic process: across wind bending moment, level 650 m.
 $S_t = 0.2$; $n_1 D/U = 0.5$
Blue line: bandpassfilter around $S_t(0.18-0.22)$
x-axis in wind tunnel scale

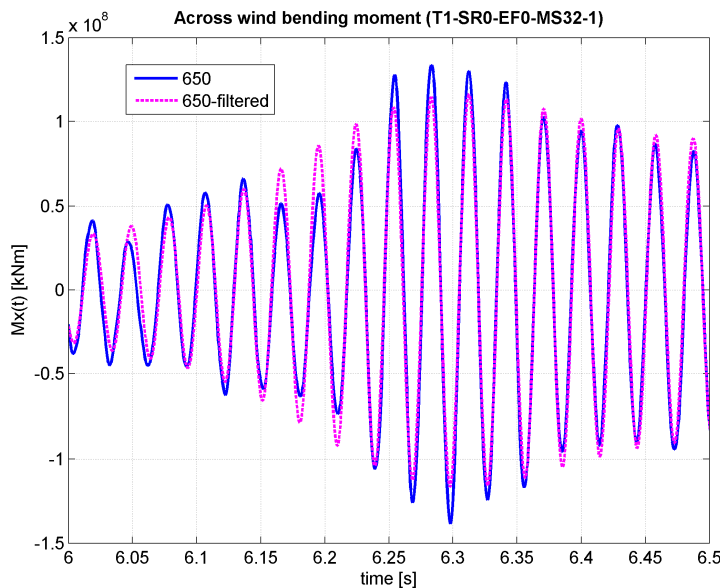


Figure 7.42 Across wind bending moment, level 650 m. Resonant conditions:
 $S_t = n_1 D/U = 0.2$
Blue line: bandpassfilter around $S_t(0.18-0.22)$
[The y-axis is one order of magnitude larger than in Figure 7.41]
x-axis in wind tunnel scale

Another important issue is the correlation along the height of the lift force and across-wind response.

The cross-correlations of the lift coefficients ($z_{ref} = 650$ m) are plotted in Figure 7.43. The correlation length of the “total” lift (i.e. unfiltered) is small, around one diameter ($L_{LIFT} = 154$ m), because of the stochastic effect of turbulence. The correlation length of the filtered time histories (so-called vortex shedding lift) is higher because the stochastic effect is largely removed. Nevertheless, it is still small ($L_{VS} = 262$ m), less than two diameters. However, the correlation of the response is much higher, being the structure itself, with its vibration frequency, a filter. In the time domain, this effect was clearly evident in Figure 7.41, where the structural oscillation governs the magenta line. In fact, the across-wind response is almost fully correlated along the whole height: Figure 7.44 shows $\rho(950, \Delta z)$ and proves that $\rho(950, 1000)$ is more than 0.8.

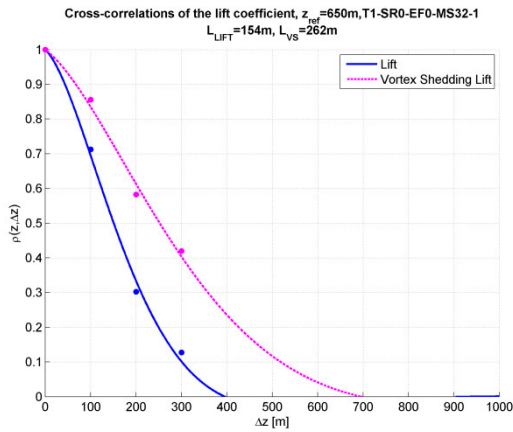


Figure 7.43 Cross-correlation coefficients of lift and vortex shedding lift ($z_{ref} = 650$ m)

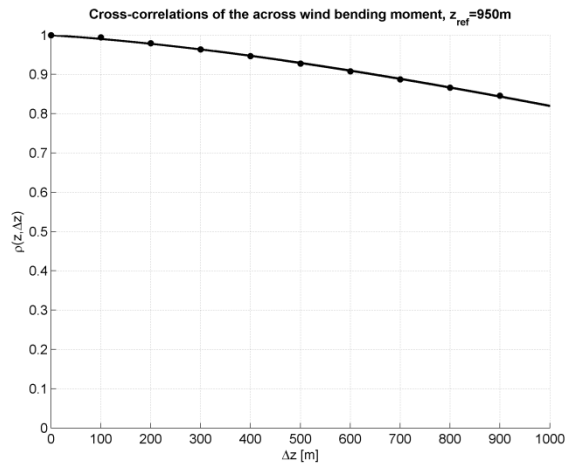


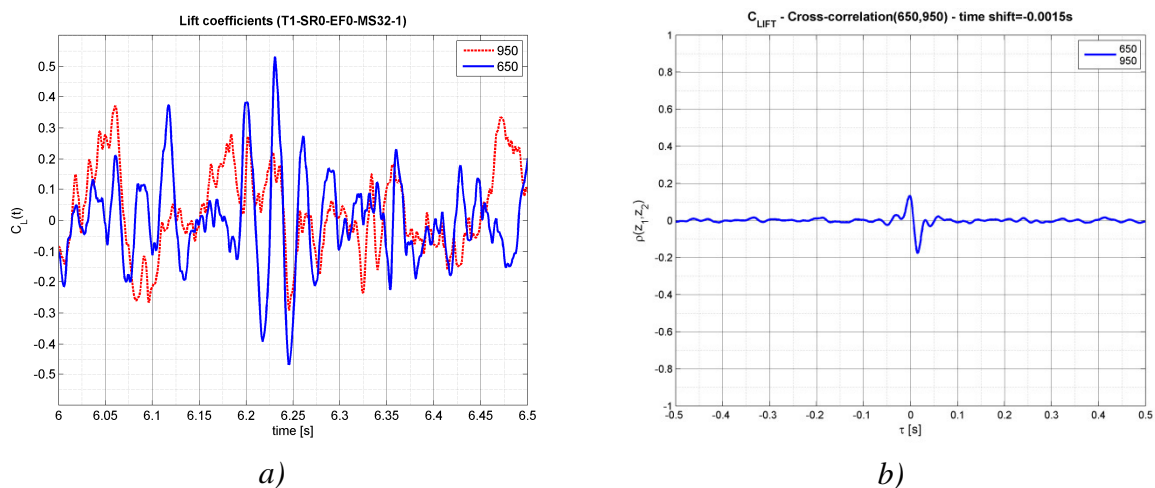
Figure 7.44 Cross-correlation coefficients of the response (across wind bending moment, $z_{ref} = 950$ m)

The spanwise correlation of the lift force and of the across-wind response is further analyzed in Figure 7.45, Figure 7.46, Figure 7.47. Two levels, 650 and 950 m, are chosen as representative. Load and response at these two levels are compared. Even if the fluctuations at 950 m are small, these levels are selected because simultaneous time histories were available at the largest separation distance ($\Delta z = 300$ m). Moreover, Figure 7.44 proves that, even if the fluctuations at 950 m are small, their correlation is high all along the tower, so that even this high level is representative.

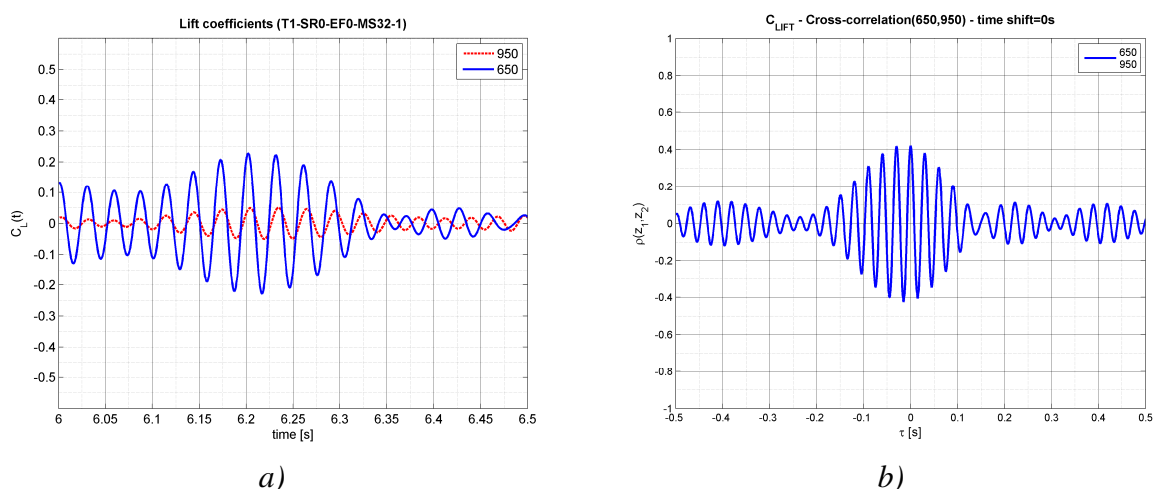
Figure 7.45 shows that in the stochastic process the load correlation due to vortex separation is strongly diminished by turbulence ($\rho = 0.1273$). Once the time histories are filtered around the Strouhal peak (Figure 7.46), the cross-correlation is expectedly higher ($\rho = 0.4197$).

The modulation in amplitude of the filtered time histories is due to the beats phenomenon. It is produced by vortex shedding frequencies which are very close to each other, so that when the different waves are out of phase they tend to cancel each other and the resulting amplitude is small. Instead, when they are in phase they sum up and the resulting amplitude of oscillation is higher. This enhances the cross-correlation between different levels, too.

Figure 7.46 shows the correlation of the response at $z_1 = 950$ m and $z_2 = 650$ m. Consistently with Figure 7.44, the response has a much stronger correlation. The predominant oscillation is the bending vibration mode. The cross-correlation between the responses at the two levels is still close to 1 ($\rho = 0.9638$), although the two levels are at a distance of 300 m.



a) b)
 Figure 7.45 Lift coefficients at $z = 650$ and 950 m
 a) time histories; b) cross-correlation function. $\rho(650,950) = 0.1273$



a) b)
 Figure 7.46 Lift coefficients at $z = 650$ and 950 m: filtered time histories, bandpass filter around Strouhal (0.18-0.22).
 a) time histories; b) cross-correlation function. $\rho(650,950) = 0.4197$

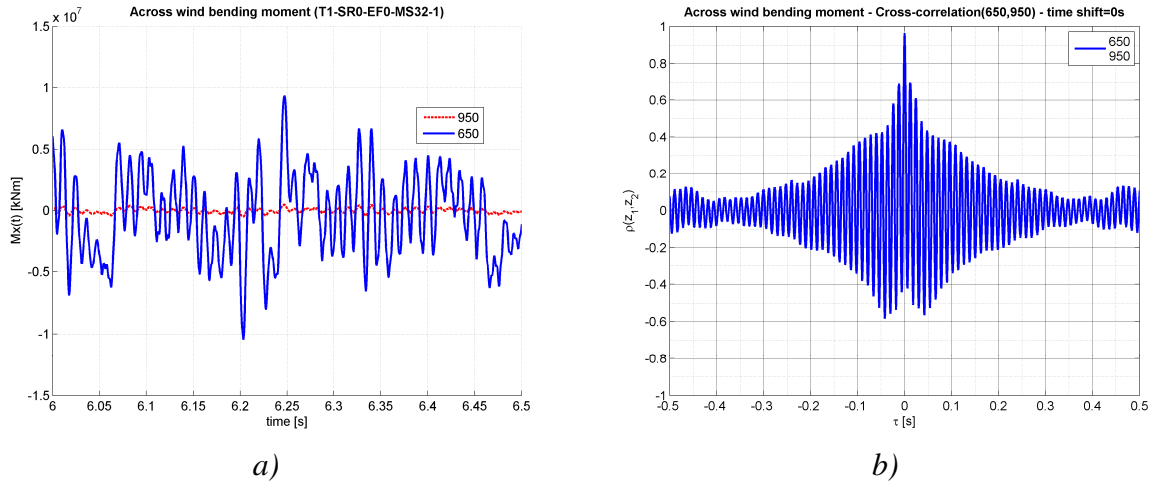


Figure 7.47 Cross-wind response at $z = 650$ and 950 m: a) time histories; b) cross-correlation function. $\rho(650,950) = 0.9638$

7.2.2 The structural response to the asymmetric load

The mean asymmetric load created by the rings is characterized by higher drag (Figure 5.39) and mean steady lift. $C_{L,m}$ is in any case considerable smaller than $C_{D,m}$. Moreover, the effect of the steady lift at the base is partially balanced by the inversion of the force along the height. In case of rings, the force coefficients (obtained by pressure integration) were not measured all along the height, therefore some approximation has been introduced in the calculation.

Relying on the measurements, a suitable resulting load model is plotted in Figure 7.48, together with its structural response in Figure 7.49. Numerical values are reported in the appendix (Table A.11, Table A.12).

At $z = 0$:

NO RINGS: $M_{D,m} = 6.45 \cdot 10^7$ kNm (along wind, mean response)

$$M_{res,m} = M_{D,m} = 6.45 \cdot 10^7 \text{ kNm}$$

10 RINGS: $M_{D,m} = 7.01 \cdot 10^7$ kNm (along wind, mean response)

$$M_{L,m} = 3.14 \cdot 10^6 \text{ kNm (across wind, mean response)}$$

$$M_{res,m} = (M_{D,m}^2 + M_{L,m}^2)^{0.5} = 7.02 \cdot 10^7 \text{ kNm}$$

Globally, in case of 10 rings, an increase in the mean bending moment at the base is estimated of about 9%:

$$M_{res,m}(10 \text{ rings}) / M_{res,m}(\text{no rings}) = 7.02 \cdot 10^7 / 6.45 \cdot 10^7 = 1.09$$

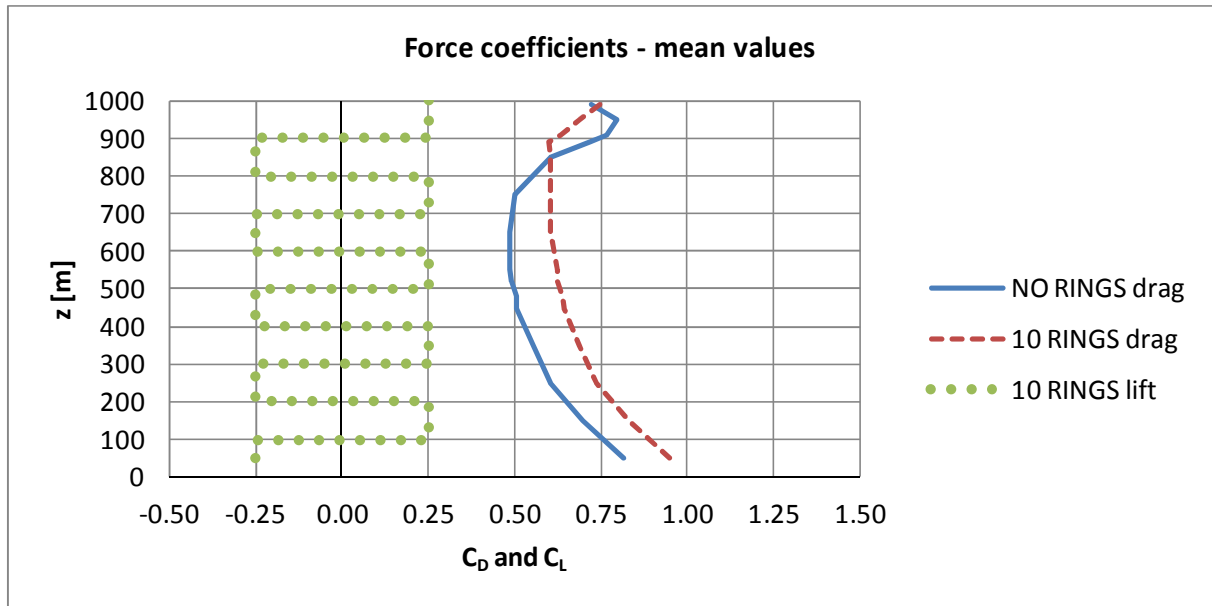


Figure 7.48 Effect of asymmetric flow due to ring beams: mean load

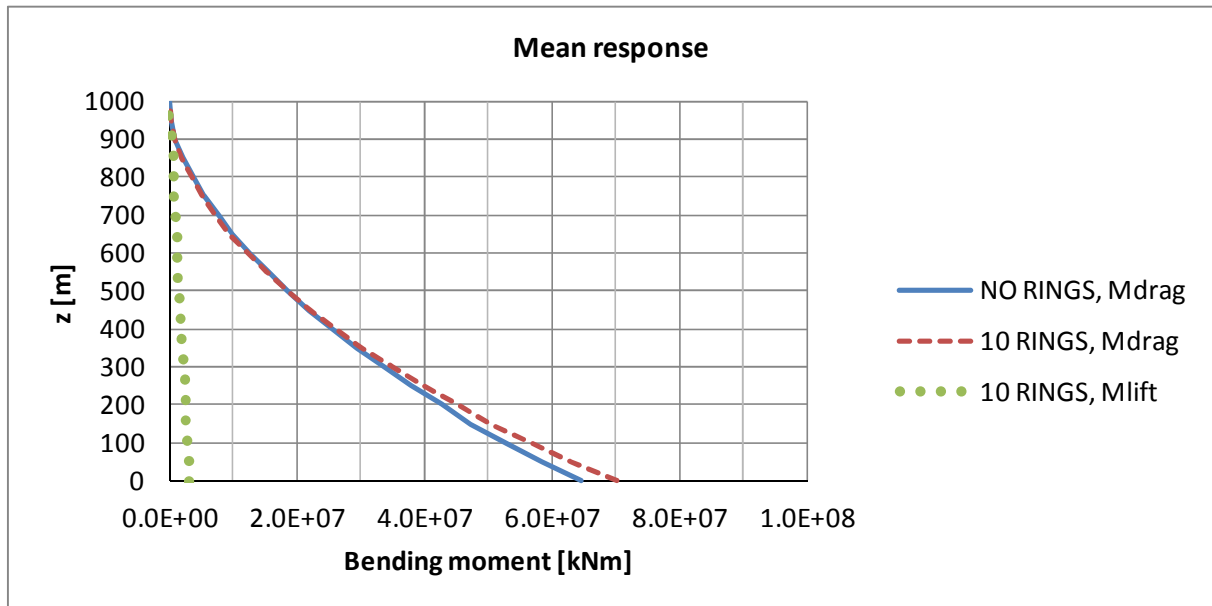


Figure 7.49 Effect of asymmetric load due to ring beams: mean response

Then, the effect on the response is evaluated by applying simultaneous time histories in a quasi-static and a dynamic calculation. The calculation is performed like in section 7.2.1. Results are reported in Table 7.11.

Table 7.11 Beam response (along and across wind bending moment) without and with resonance (load configuration with 10 rings, WiSt data)

z	950	850	750	650	0	m		
C_D, σ^2	0.101	0.095	0.095	0.104	0.104		drag coeff.	variance
C_L, σ^2	0.014	0.017	0.022	0.039	0.039		lift coeff.	variance
M_D, σ_B^2	9.24E+08	6.39E+10	3.92E+11	1.28E+12	6.59E+13	[kNm] ²	along wind	background

$M_{D,\sigma_B^2+\sigma_R^2}$	4.08E+10	8.12E+11	4.08E+12	1.20E+13	2.60E+14	[kNm] ²	along wind	with resonance
M_{L,σ_B^2}	1.37E+09	9.56E+10	6.24E+11	2.20E+12	1.66E+14	[kNm] ²	across wind	background
$M_{L,\sigma_B^2+\sigma_R^2}$	4.20E+10	8.50E+11	4.37E+12	1.32E+13	3.60E+14	[kNm] ²	across wind	with resonance
M_{res,σ_B^2}	1,30E+09	7,19E+10	1,36E+12	1,36E+12	7,19E+13	[kNm] ²	tot. response	background
$M_{res,\sigma_B^2+\sigma_R^2}$	3,88E+10	7,82E+11	3,97E+12	1,18E+13	2,69E+14	[kNm] ²	tot. response	with resonance

Finally, through the comparison of Table 7.10 and Table 7.11, it can be quantified that the increase in the peak response at the base in case of ten rings is about 13% (Table 7.12, Table 7.13). It is basically an effect in the along-wind direction; in fact, the contribution given by the steady lift is one order of magnitude lower. Therefore, the effect of the rings on the beam response is not dramatic. Furthermore, the results presented here represent the highest limit, i.e. many rings (ten) and rather big.

Table 7.12 Across and along wind beam response (including resonance) without and with rings:

	Along wind response (at z = 0)			Across wind response (at z = 0)		
	$M_{D,m}$ [kNm]	$M_{D,\sigma}$ [kNm]	$M_{D,peak}$ [kNm]	$M_{L,m}$ [kNm]	$M_{L,\sigma}$ [kNm]	$M_{L,peak}$ [kNm]
SR0	6.45E+07	1.34E+07	1.12E+08		1.81E+07	6.34E+07
SR1	7.01E+07	1.61E+07	1.27E+08	3.14E+06	1.90E+07	6.96E+07
SR1/SR0	1.09	1.20	1.13		1.05	1.10

SR0 = load modification due to the rings not included;
SR1 = load modification due to 10 rings included

Table 7.13 Resultant beam response (including resonance) without and with rings

	Resultant response (at z = 0)		
	$M_{res,m}$ [kNm]	$M_{res,\sigma}$ [kNm]	$M_{res,peak}$ [kNm]
SR0	6.45E+07	1.39E+07	1.13E+08
SR1	7.02E+07	1.64E+07	1.28E+08
SR1/SR0	1.09	1.18	1.13

SR0 = load modification due to the rings not included;
SR1 = load modification due to 10 rings included

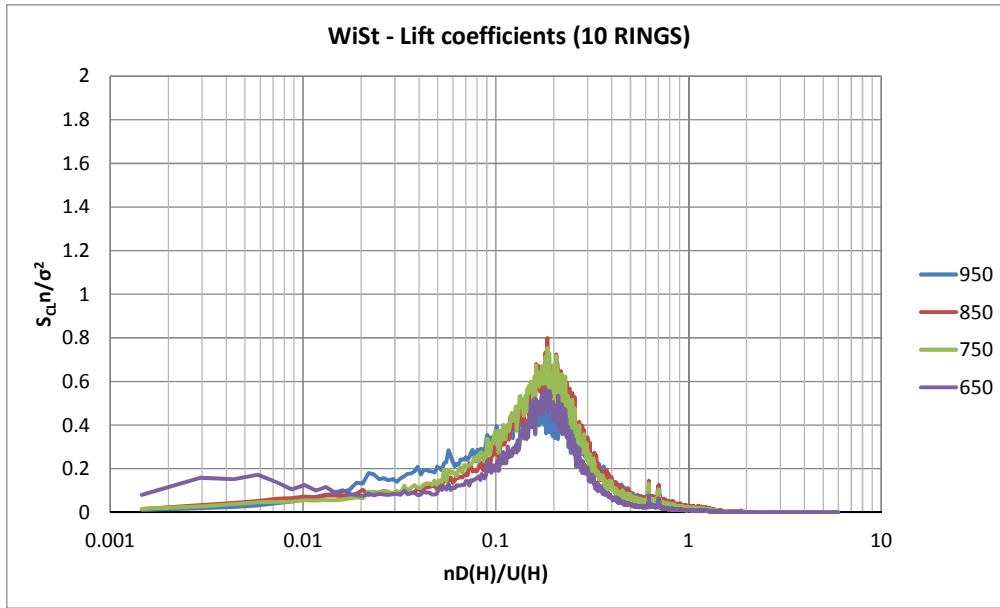


Figure 7.50
Spectra
along the
height of lift
coefficient

(SR1,
effect of 10
rings on the
load
included,
WiSt data)

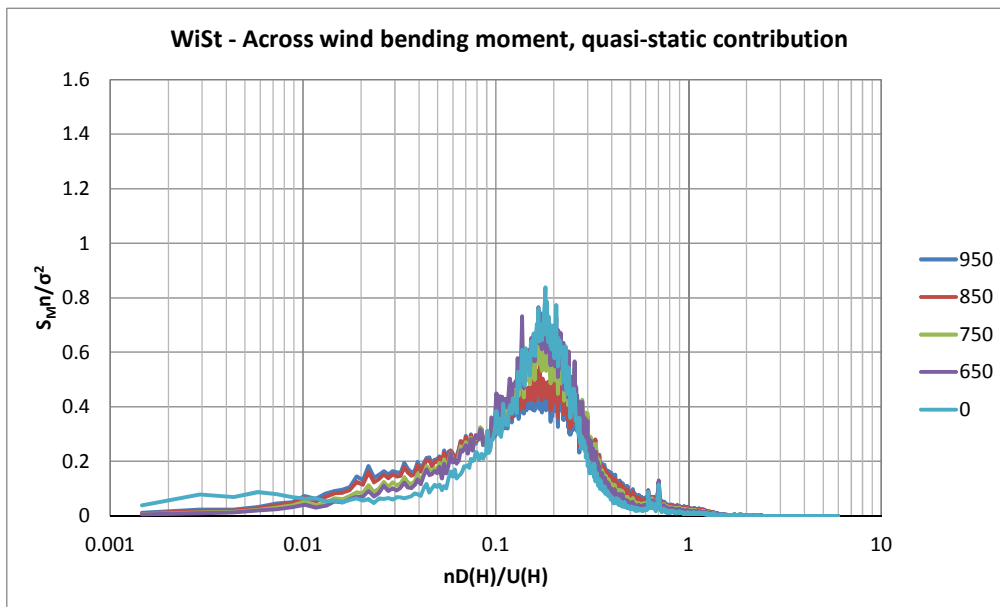


Figure 7.51
Structural
response in
the across-
wind
direction.
Resonance
not included.

(SR1,
effect of 10
rings on the
load
included,
WiSt data)

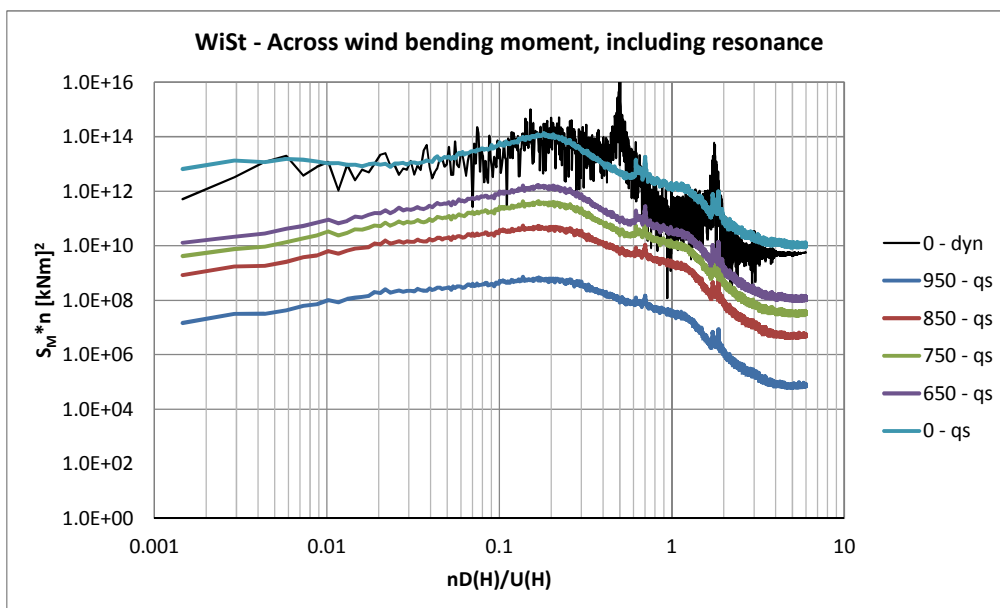


Figure 7.52
Structural
response in
the across-
wind
direction.
Resonance
included.

(SR1,
effect of 10
rings on the
load
included,
WiSt data)

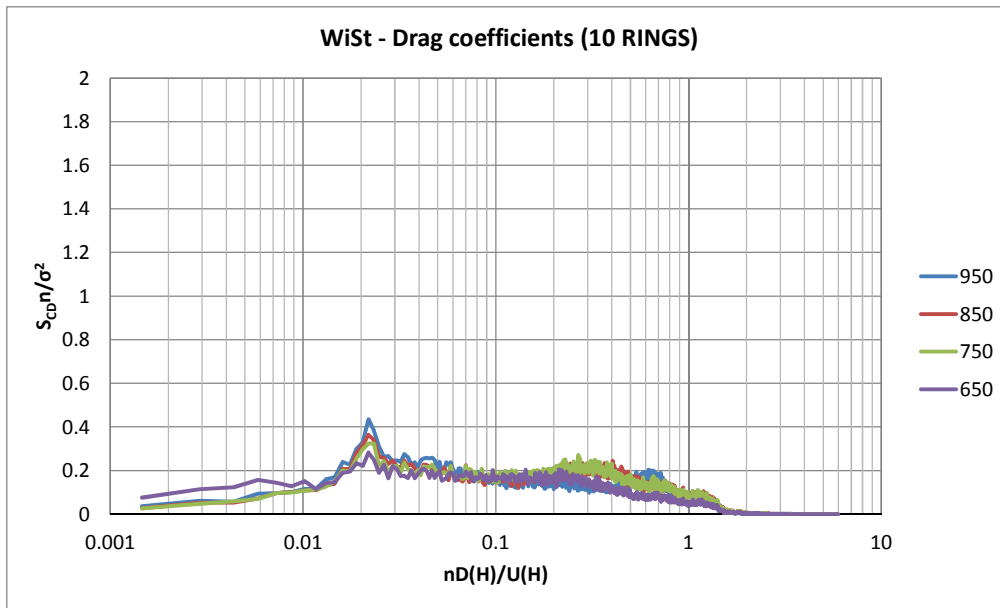


Figure 7.53
Spectra
along the
height of
drag
coefficient

(SR1,
effect of 10
rings on the
load
included,
WiSt data)

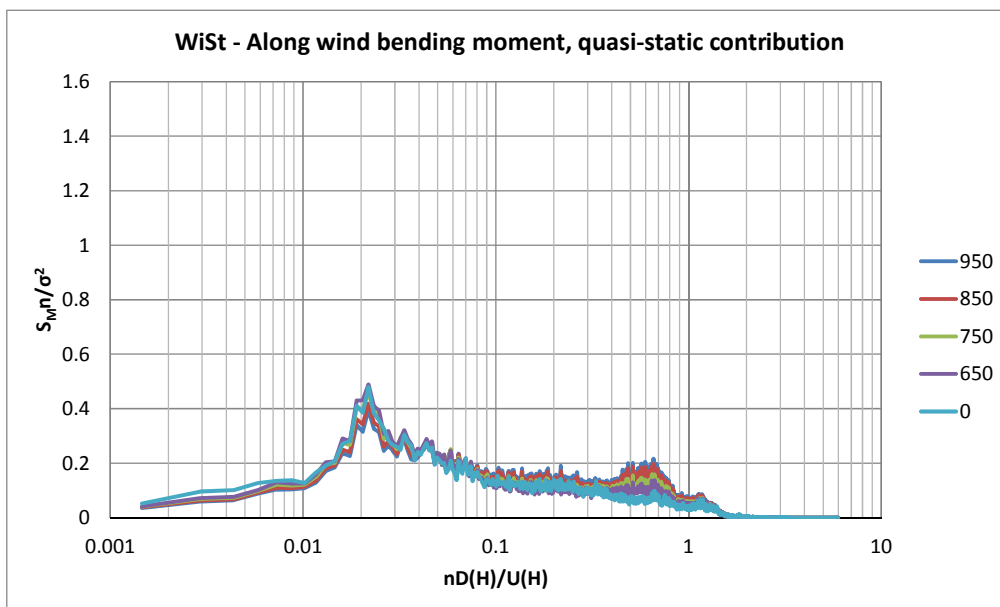


Figure 7.54
Structural
response in
the along-
wind
direction.
Resonance
not included.

(SR1,
effect of 10
rings on the
load
included,
WiSt data)

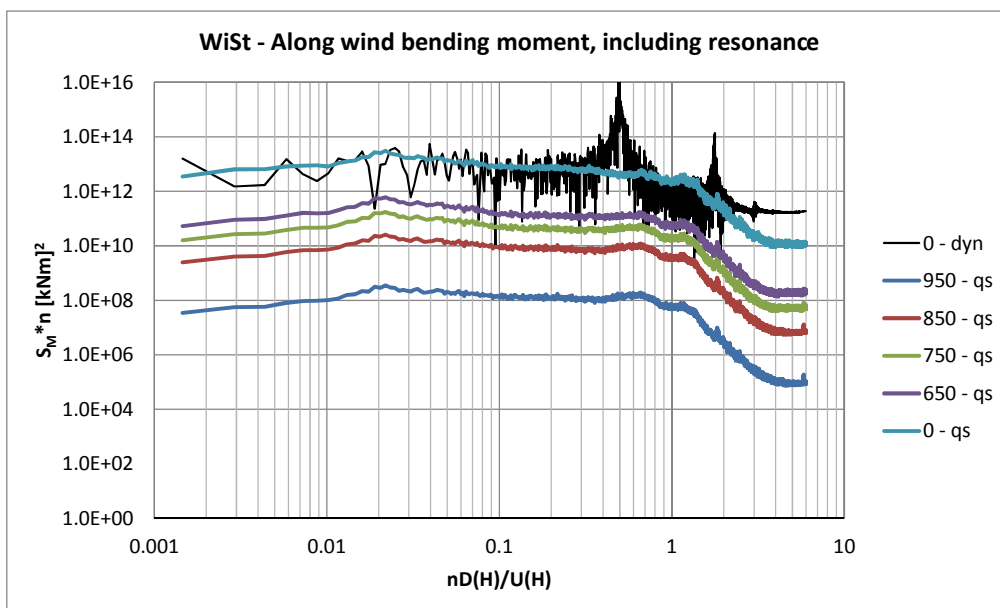


Figure 7.55
Structural
response in
the along-
wind
direction.
Resonance
included.

(SR1,
effect of 10
rings on the
load
included,
WiSt data)

7.3 The shell response

The shell response to the stochastic wind loading process is at first investigated through the covariance method. It is a quasi-static calculation (resonance not included) and it allows to consider the wind effect due to correlation of pressure. Input data are $C_{p,m}$, $C_{p,\sigma}$, $\rho(\Delta z, \Delta\phi)$. They are all available by the experiments¹¹. Then, dynamic calculations which include inertial and damping forces are performed on the tower by the software Ansys. The structural calculations always assume the presence of stiffening rings along the height (see Figure 1.13 and Figure 1.14 for the reference tower geometry), while the modification the rings create on the load is included only if specified.

In section 7.1 the big amount of experimental data has been simplified in a few parameters, which are of general application by the designer in any design condition. This simplified model is now validated through comparison of responses by applying either the experimental load data (directly measured) or the simplified load model. Results of the simplified model turn to be well representative of the experimental situation, so they can be extended in further applications to different boundary layer flows (and to structures of different aspect ratios). They allow to calculate the background response to the stochastic process in case of linear structural behaviour.

The wind load model derived from the wind tunnel investigation is then applied to a codified design wind profile for a certain location and terrain category. The local effects in the vicinity of the ring beams represent the substantial difference which is not included in the beam model presented before.

As the wind load is influenced by the actual number and size of rings, the quantification of the expected increase in stresses in the response due to the rings is another object of this section (see 7.3.4).

7.3.1 Validation of the simplified wind load model

The stochastic wind load model proposed in section 7.1 is suitable for being used in the quasi-static calculations through the covariance method (Niemann et al., 1996). The input data which are required are: $C_{p,m}$, $C_{p,\sigma}$, $\rho(\Delta\phi)$ and $\rho(\Delta z)$. They have been modelled in section 7.1 with regard to the flow properties (especially I_u and L_{uz}) and summarized in the appendix (section 10.1).

¹¹ For locations where $\rho(\Delta z, \Delta\phi)$ is not measured, it is substituted by the product between $\rho(\Delta z)$ and $\rho(\Delta\phi)$.

In this section, the structural response of the tower is evaluated through the covariance method, both under the experimental data (directly measured at WiSt tunnel) and the simplified load model, applied to the same flow condition (the one at WiSt wind tunnel). The results are compared in order to identify to which extent the simplifying assumptions on the stochastic load in section 7.1 may affect the response. The aim is to validate the general use of the simplified stochastic load model for any atmospheric boundary layer flow. The wind load model (proposed in section 7.1) introduced the following approximations:

- the cross-correlations between points with horizontal and vertical separation are modeled as a product of $\rho(\Delta\phi)$ and $\rho(\Delta z)$;
- $A(z) = 2$ constant along the height is a value on the safe side only at $z/H > 0.2$ (section 7.1.3) because it does not include horseshoe and base vortices;
- the body-induced fluctuations (Figure 7.19) are extrapolated at $I_u = 0$, through the assumption that they are not correlated to turbulence-induced fluctuations, although the wake fluctuations show a certain correlation with points before separation (Figure 7.27);
- the vertical correlations refer to the unified value around the circumference $L_{pz} = (3/2)L_{uz}$ (Table 7.8) and the constant almost asymptotic correlation at large distances, due to a large recirculation bubble in the near-wake, is neglected.

These approximations are accepted in view of the following results. Only the first simplifying assumption cannot be completely assessed because of the lack of the complete three dimensional correlation field; further experiments would be necessary (Chapter 8). The lack of a three dimensional correlation field might be one of the main reasons for the differences in the standard deviation of the stresses. In the following figures, the blue lines represent the effect that result from the experimental data, the red dots/lines from the simplified stochastic model applied to the same flow condition. The stochastic model underestimates of about 10% the rms values of internal forces. As regards the bending moments, the differences are less than 1 kNm/m. Moreover, the approximation is strongly reduced once the peak values are considered, so that the model can be accepted (Figure 7.56). The peak values of the structural response ($S =$ either n_{11} , n_{22} , m_{11} or m_{22} , i.e. circumferential or meridional forces and bending moments (direction 1 is circumferential, 2 is meridional)) are calculated as follows:

$$S_p = S_m + 3.5\sigma_s \quad \text{if } S_m \geq 0 \quad (7.34)$$

$$S_p = S_m - 3.5\sigma_s \quad \text{if } S_m < 0$$

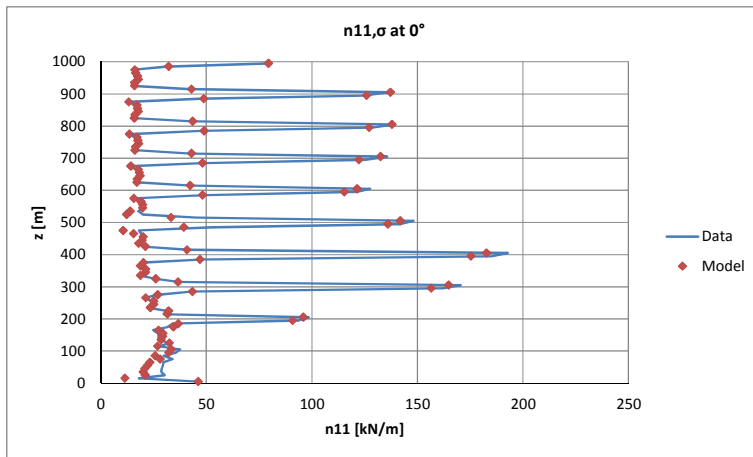


Figure 7.56 a)
Circumferential force,
rms values.
(continued)

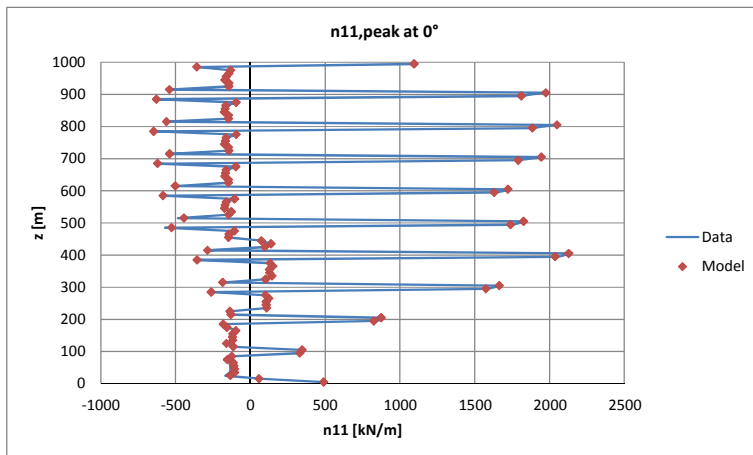


Figure 7.56 b)
Circumferential force,
peak values.
(continued)

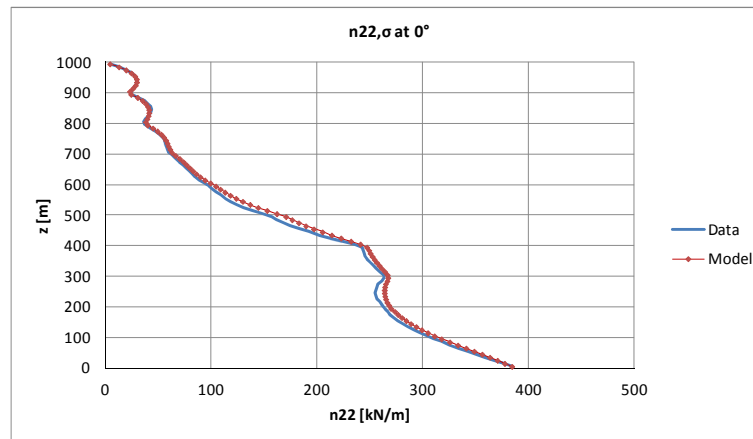


Figure 7.56 c)
Meridional force,
rms values
(continued)

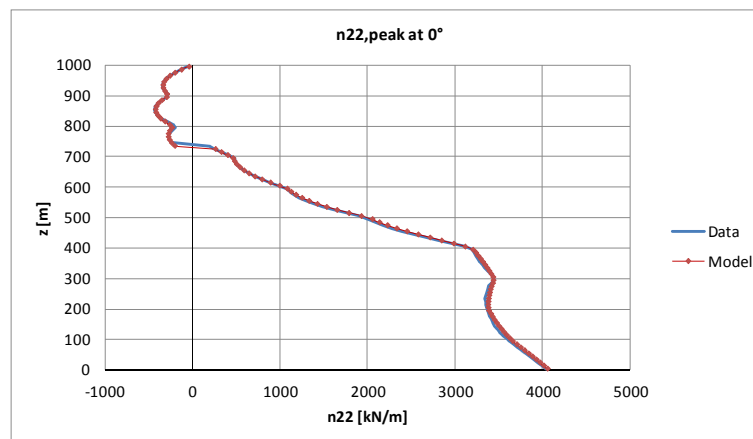


Figure 7.56 d)
Meridional force,
peak values
(continued)

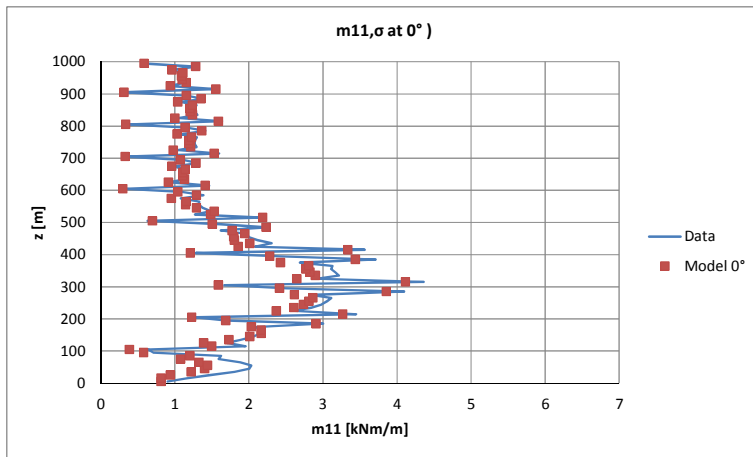


Figure 7.56 e)
Circumferential bending moment, rms values
(continued)

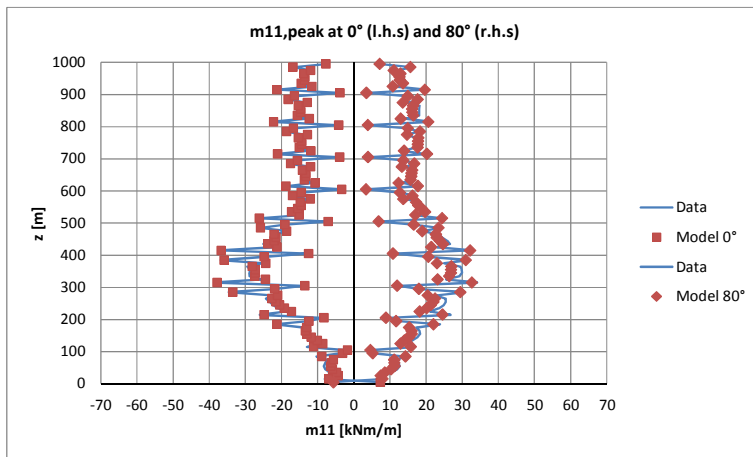


Figure 7.56 f)
Circumferential bending moment, peak values
(continued)

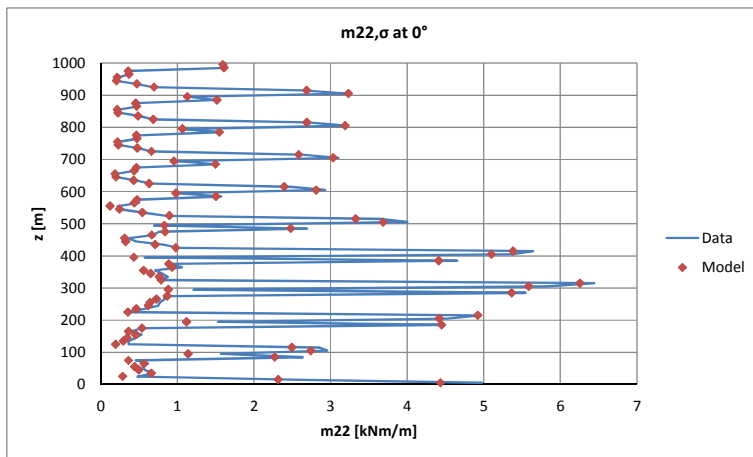


Figure 7.56 g)
Meridional bending moment, rms values
(continued)

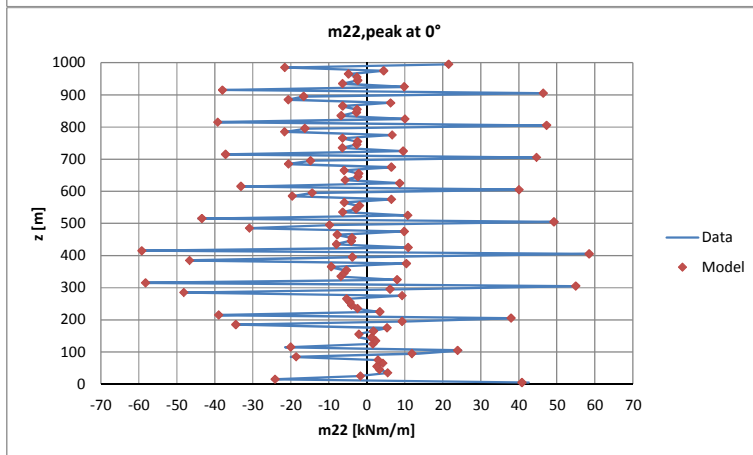


Figure 7.56 h)
Meridional bending moment, peak values
(continued)

Figure 7.56 Structural response along the height at significant angles, comparison by using experimental load data (blue lines) and proposed stochastic load model (red dots). Validation of the model. Resonance not included; effect of the rings on the load not included.

7.3.2 Local effects in the vicinity of the stiffening rings

The stiffening rings were originally introduced in the design (Goldack, 2004; Backström et al., 2008) in order to reduce ovalizations of the shell. A certain number of rings, properly stiffened, can guarantee a beam-like behaviour at the first eigenmode. As a result, the distribution of internal forces under the wind action is improved and the peaks of tension at the windward side are reduced. By increasing the stiffness and/or the number of rings, the circumferential distribution of meridional forces changes from a cosines-like distribution (typical for shells) to a linear distribution crossing zero at 90° , that is typical for beams (Lupi, 2009). With ten rings, such a beam-like distribution is achieved in the cylindrical shell at middle height (Figure 7.57, black curve). Ovalizations of the shell at the windward side in the upper part of the tower are responsible for the negative values of n_{22} at stagnation and lateral tension at the flanges, as it occurs for example at 850 m in the figure.

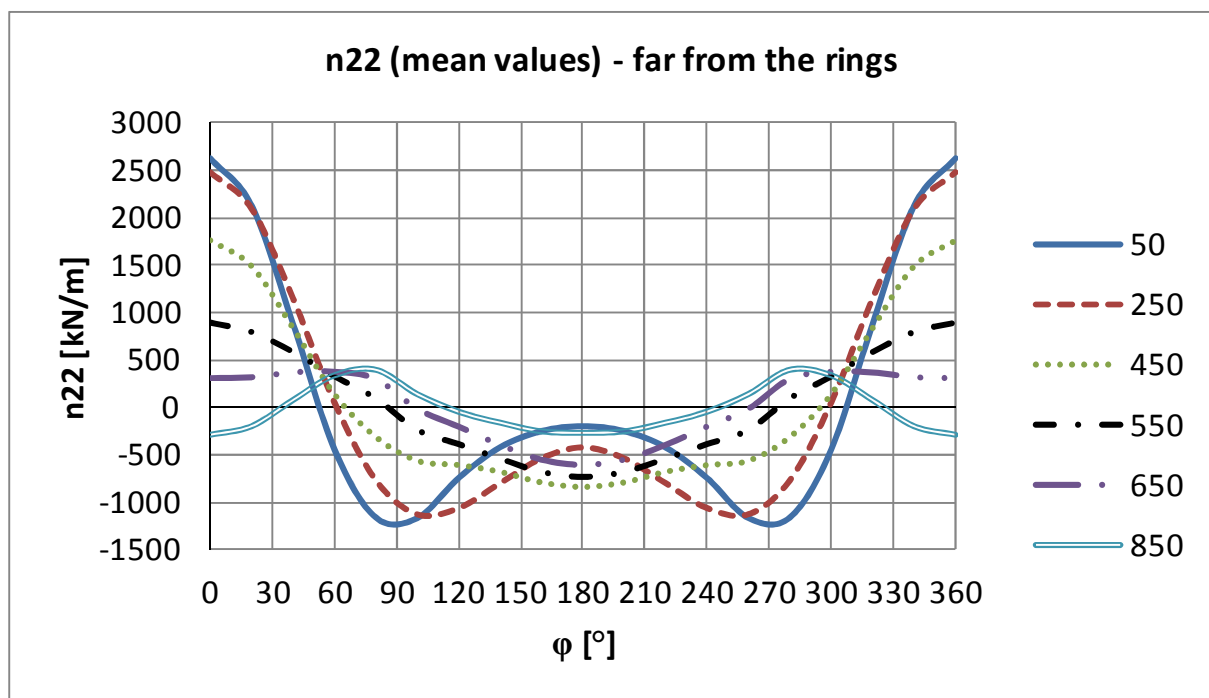


Figure 7.57 Circumferential distribution of meridional stresses – mean response

Even though the stiffening rings guarantee a global beam-like behaviour, evaluation of local effects in the vicinity of the ring beams requires the application of a shell-like model. The magnitude of such local effects – due to ovalization of the cross-section,

especially because of the constraining effect of the rings – confirms what was stated in section 2.4 by equation (2.50): a Solar Tower cannot be fully designed by using the beam theory.

The design of the tower is governed by the stresses in the half of the shell which is exposed to the wind. The meridians at stagnation and at 80° (maximum suction) have the highest tension stresses. The stresses at stagnation are reported in the following figures. The calculation is done by the covariance method (resonance not included). The stochastic wind load model results from wind tunnel investigation; this is now applied to the following design properties of the atmospheric boundary layer:

- terrain category II ($z_0 = 0.05$ m), $V_b(10\text{m}) = 25$ m/s, latitude = 23° ;
- mean wind profile: according to H&D model;
- turbulence intensity: according to the H&D model;
- integral length scale: according to Eurocode;

All these profiles are plotted in Figure 2.4, Figure 2.5, Figure 2.6.

The H&D model would suggest a much larger integral length scale. The approach of the Eurocode is preferred in this calculation, but the designer should bear in mind that a larger integral length scale would imply higher background response.

The following figures show that the structural effect of the rings on the response has an extension in the shell of around 20 m both above and below each ring. In that region both positive and negative peaks of n_{11} , m_{11} and m_{22} arise, due to the constraining effect to the ovalization of the shell exerted by the rings.

Another issue, which is not addressed in this work, but it should be investigated in view of the design, is the correlation of peak effects. In particular, the design of the shell reinforcement should result from combination of axial force and bending moment. The highest limit, if their peaks are fully correlated, is their sum, while the lowest limit in case of zero correlation is the square root of the sum of single square values.

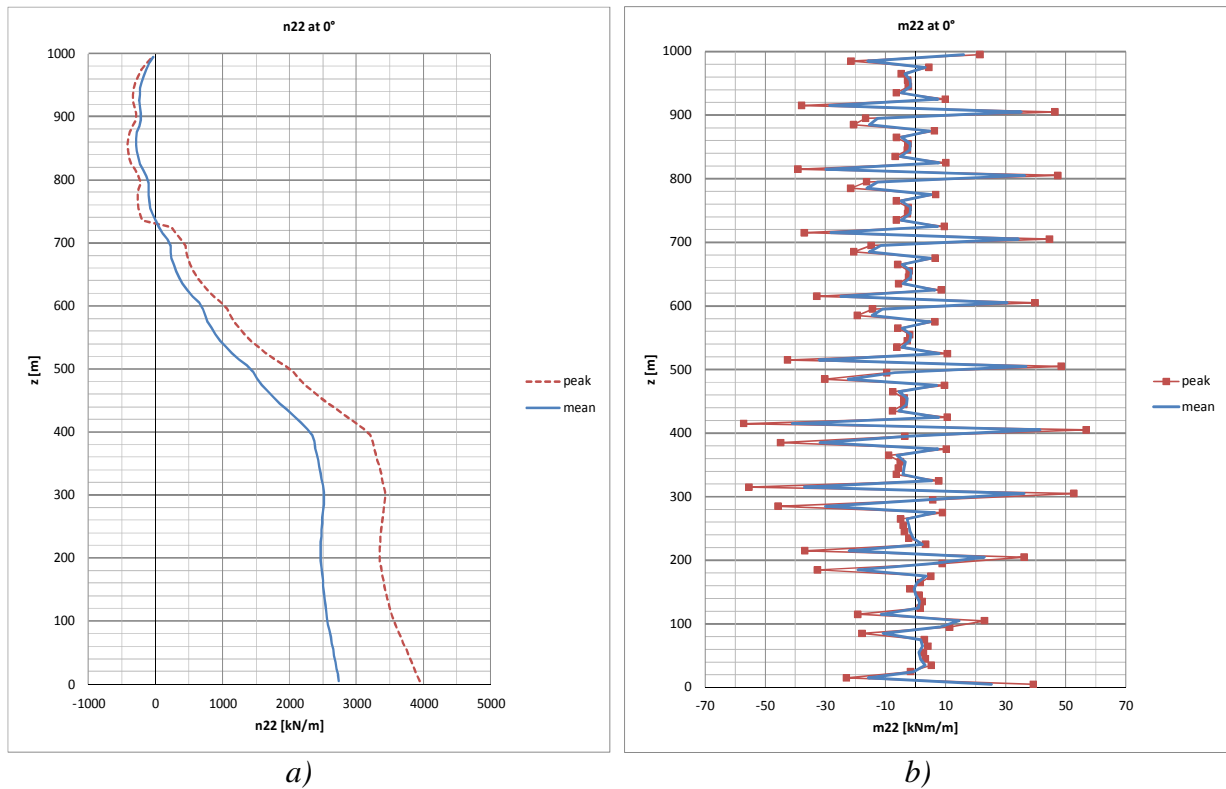


Figure 7.58 Shell response in a design condition: meridional force n_{22} (fig. a) and bending moment m_{22} (fig. b) at 0° (resonance not included, effect of the rings on the load not included)

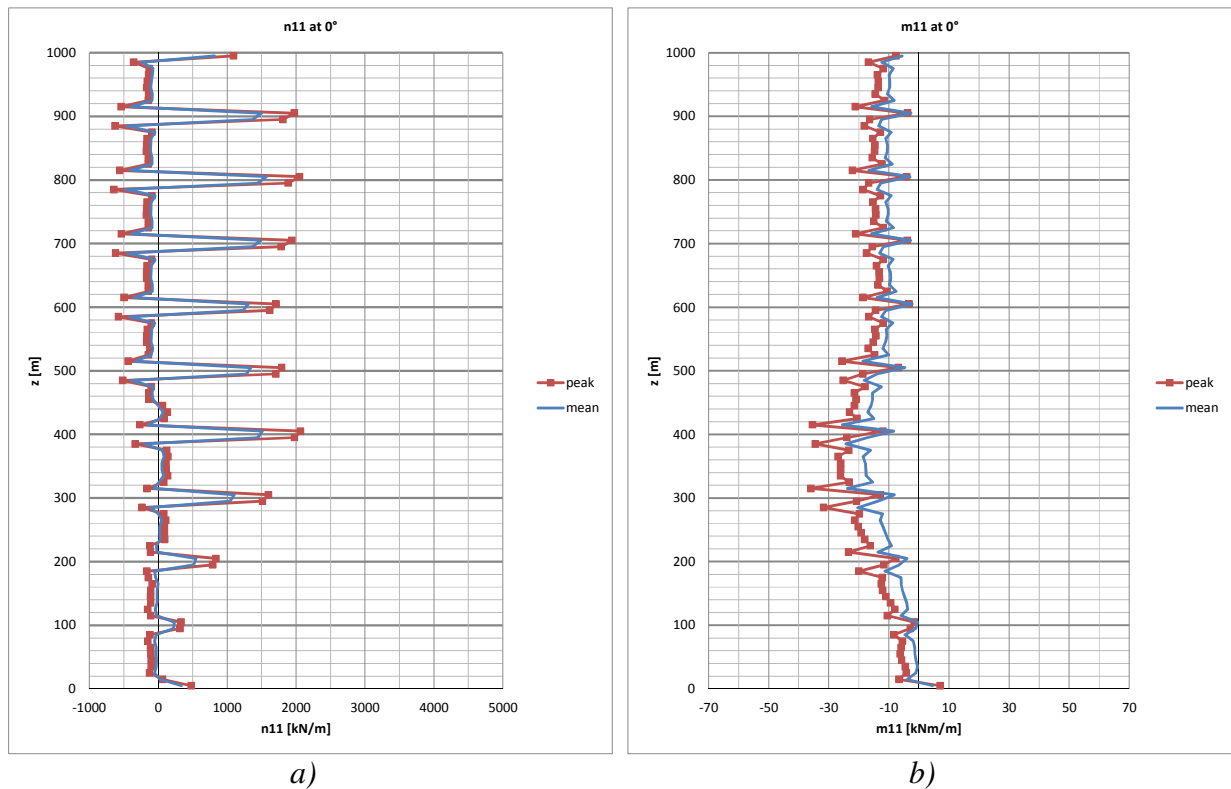


Figure 7.59 Shell response in a design condition: circumferential force n_{11} (fig. a) and bending moment m_{11} (fig. b) at 0° (resonance not included, effect of the rings on the load not included)

7.3.3 Dynamic amplification

The dynamic amplification is calculated by using the software Ansys. Simultaneous time histories measured in the wind tunnel along the circumference at $z/H = 0.95; 0.85; 0.75; 0.65$ are used for the purpose of this investigation. All the other loads are then fully correlated with them. The result is on the safe side because the predominant contribution is the bending mode, which does not present inversions of shape along the height. However, the result can be only considered as a global effect on the structure. A more sophisticated load condition should be considered in order to investigate dynamic effects in the vicinity of the ring beams. This is, however, beyond the purpose of this work.

The calculation includes mass and damping forces. The Rayleigh damping ($\mathbf{D} = \alpha\mathbf{M} + \beta\mathbf{K}$) is calculated assuming modal damping ratios ξ_i equal to 0.01 (corresponding to a logarithmic decrement $\delta = 2\pi\xi \approx 0.06$) at $n_1 = 0.17$ Hz (beam bending mode) and $n_3 = 0.33$ Hz (shell-like mode with two waves), according to the formula $\xi_i = \alpha/2\omega_i + \beta\omega_i/2$, where $\omega_i = 2\pi n_i$. As in the beam calculation (section 7.2.1), the time factor for transferring data from wind tunnel to full-scale is $\lambda_T = 488$. The integration time step is 0.244 s, as in the beam calculation.

In order to evaluate the dynamic amplification, the results of the dynamic analysis (including mass and damping forces) are compared with the results of a quasi-steady calculation, i.e. a static calculation (not including mass and damping forces) at each time step. The dynamic amplification is the ratio of peak responses, the one at the nominator results from dynamic calculation, the one at the denominator results from the quasi-steady calculation. The mean response is included in the definition of the dynamic amplification. Moreover, only representative results are considered. In fact, the interest of the designer is in the dynamic amplification of those parts of the tower which are especially exposed to the wind action and thus govern the design. In practice, the stagnation line plays the most important role. Since the tower thickness varies along the height, it is important to be aware of the dynamic amplification all along the height, although internal forces are smaller in the tip region. As shown by Figure 7.60, the dynamic amplification is around 10% only at the base of the tower. Along the height, it is much higher than what was expected according to Eurocode calculations ($C_d = 1.04$ in Lupi, 2009). Further studies are then necessary. The result does not depend significantly on the class of concrete which is selected for the calculation.

These calculations are performed with C50/60 concrete (so that $n_1 = 0.17$ Hz). In fact, the class could be even higher (C70/85) and in this case it would be $n_1 = 0.18$ Hz.

However, as seen in a comparative calculation, this does not change significantly the dynamic response.

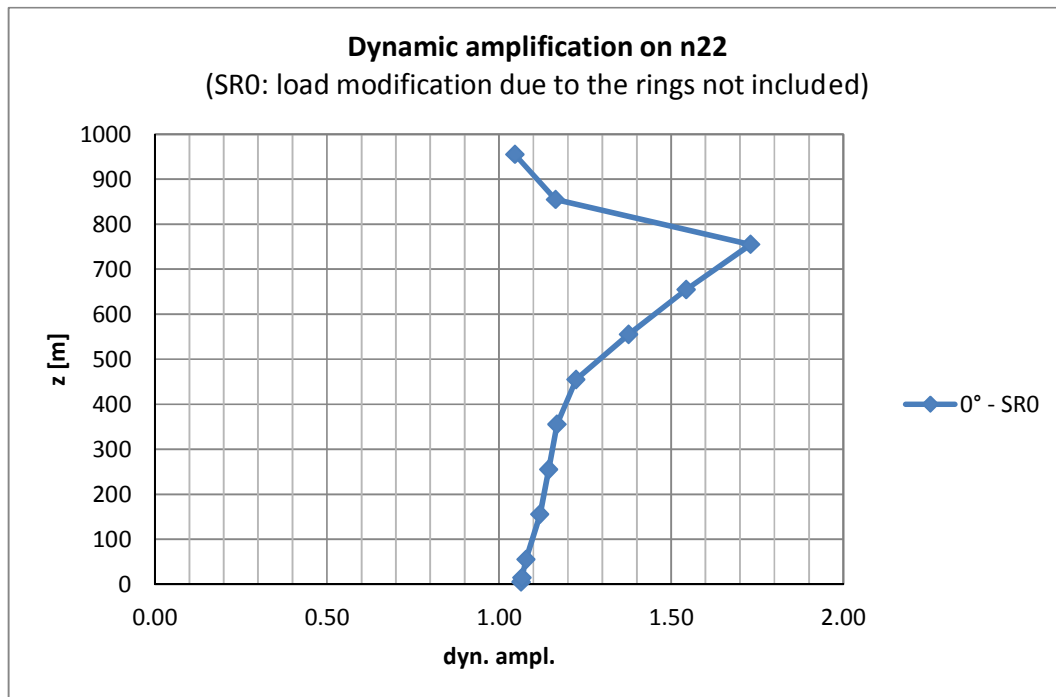


Figure 7.60 Dynamic amplification at stagnation – WiSt results (load modification due to the rings not included)

7.3.4 The shell response under asymmetric wind load (10 ring beams)

The asymmetric response of the tower, due to the load modification induced by the rings (SR1) is analyzed in this section, both in quasi-static and dynamic calculations.

The covariance method is applied to input data that describe the asymmetric load condition, with inversion along the height, created by 10 ring beams (section 5.5). This load condition corresponds to SR1. The response to the SR1 load condition (red lines in the following graphs) is compared to the response in SR0 (load modification due to rings not included, blue lines in the graphs). In any case, the calculation is made on a structure with ten rings (like in Figure 1.13). The flow condition (mean profile, turbulence intensity, integral length scale) is the one in the WiSt tunnel, properly scaled according to the prototype.

The most appreciable effect on the response, due to the load modification induced by the ring beams, is on the meridional forces n_{22} (Table 7.15, Figure 7.63). In particular, the increase in the peak meridional force (n_{22}) at the base is around 10%, comparable to the increase in bending moment in the beam-like model (section 7.2.2).

As regards the circumferential stresses (n_{11}), they are high only close to the rings and the highest ones are at the throat of the hyperboloid. The increase in stresses due to the

load modification induced by the rings is less than 10% in the peak response and somewhat higher in the standard deviations (Table 7.14, Figure 7.62).

The bending moments in both meridional and circumferential directions do not present significant variations due to rings; they do not differ more than 5 kNm/m in the peak response.

Numerical values are reported in the appendix (Table A.14, Table A.15, Table A.16).

In any case, these results represent the highest limit in case of ten big rings. Intermediate situations are expected with smaller rings and/or at larger distance. Moreover, the asymmetric load condition all along the height is the worst condition in which the two asymmetric states are never mixed. In fact, the mixture of the two states at low levels tends to weaken the asymmetry towards a mostly symmetric condition at the base, as observed in Chapter 6.

*Table 7.14 Effect of load modification due to 10 rings on the quasi-static response (n_{11})
WiSt data; SR0 = load modification due to the rings not included;
SR1 = load modification due to 10 rings included*

z [m]	$n_{11,peak}$ at 0° [kN/m]			$n_{11,m}$ at 0° [kN/m]			$n_{11,\sigma}$ at 0° [kN/m]		
	SR0	SR1	SR1/SR0	SR0	SR1	SR1/SR0	SR0	SR1	SR1/SR0
5	479	533	1.11	326	347	1.07	45	54	1.20
105	362	370	1.02	232	245	1.05	38	36	0.97
205	890	830	0.93	548	553	1.01	99	80	0.81
305	1672	1681	1.00	1078	1090	1.01	171	169	0.99
405	2144	2269	1.06	1472	1509	1.03	193	218	1.13
505	1841	1966	1.07	1324	1361	1.03	148	174	1.17
605	1737	1824	1.05	1292	1306	1.01	128	148	1.17
705	1945	2007	1.03	1472	1468	1.00	136	154	1.14
805	2039	2084	1.02	1553	1541	0.99	139	155	1.12
905	1965	2012	1.02	1490	1484	1.00	136	152	1.11
995	1090	1096	1.00	817	798	0.98	79	86	1.09

*Table 7.15 Effect of load modification due to 10 rings on the quasi-static response (n_{22})
WiSt data; SR0 = load modification due to the rings not included;
SR1 = load modification due to 10 rings included*

z [m]	$n_{22,peak}$ at 0° [kN/m]			$n_{22,m}$ at 0° [kN/m]			$n_{22,\sigma}$ at 0° [kN/m]		
	SR0	SR1	SR1/SR0	SR0	SR1	SR1/SR0	SR0	SR1	SR1/SR0
5	4039	4442	1.10	2695	2863	1.06	385	451	1.17
105	3581	3973	1.11	2520	2709	1.08	304	362	1.19
205	3364	3683	1.09	2447	2637	1.08	262	299	1.14

305	3440	3608	1.05	2519	2649	1.05	264	275	1.04
405	3100	3117	1.01	2278	2308	1.01	236	232	0.98
505	1893	1814	0.96	1376	1334	0.97	149	137	0.93
605	992	874	0.88	667	580	0.87	93	85	0.90
705	414	337	0.81	204	128	0.62	60	60	1.00
805	-220	-260	1.18	-94	-113	1.20	36	42	1.17
905	-280	-277	0.99	-197	-186	0.95	25	27	1.08
995	-43	-44	1.02	-30	-30	1.03	5	5	1.00

From the dynamic point of view, the calculation is repeated in SR1 as in section 7.3.3. The main difference between SR1 and SR0 is at level 650 m, where the bistable asymmetric flow starts its disruption on the bubble side.

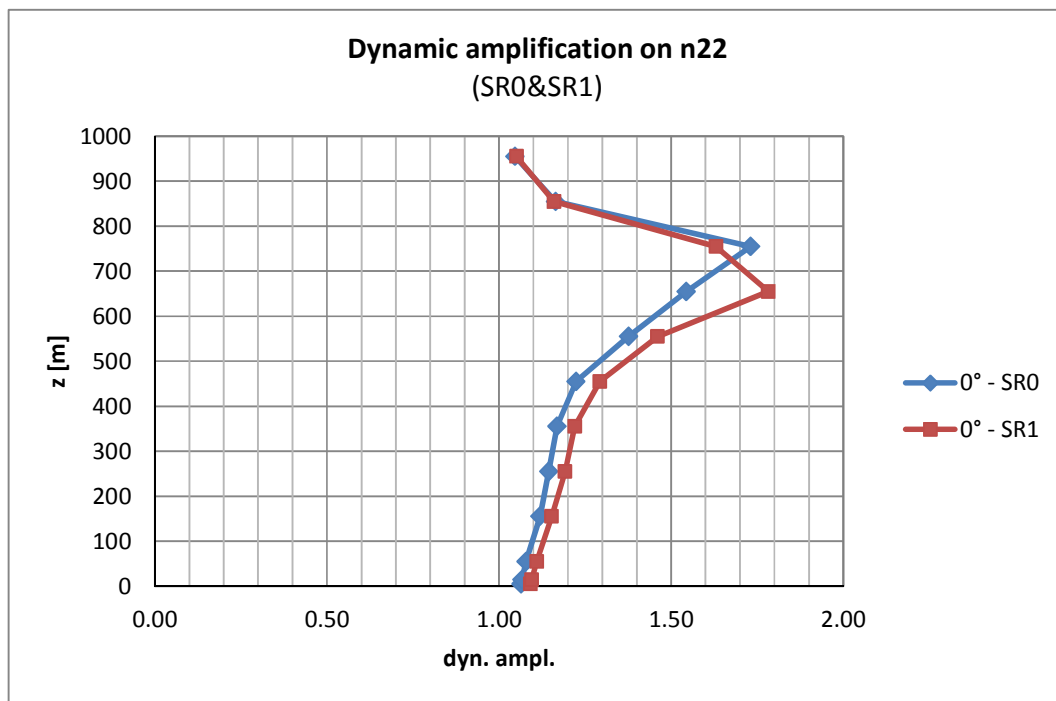


Figure 7.61 Dynamic amplification at stagnation: SR0&SR1– WiSt results

The presence of jumps in the time histories, which mark the transition from state 1 to state 2 or viceversa, should not create severe dynamic problems to the structure. The scale factor $\lambda_T = 488$ is applied to the jump reported in Figure 5.10, so that two seconds in the wind tunnel correspond to about 1000 s in full-scale. Figure 7.66 shows that the jump basically occurs between the time steps “d” and “f”. It takes about 10 s, i.e. about twice the natural period of the structure. Nevertheless, the effect of the jump on the response should be further investigated in the future (see Chapter 8), because even in a time period comparable to the natural period of the tower, the load might undergo a steep change.

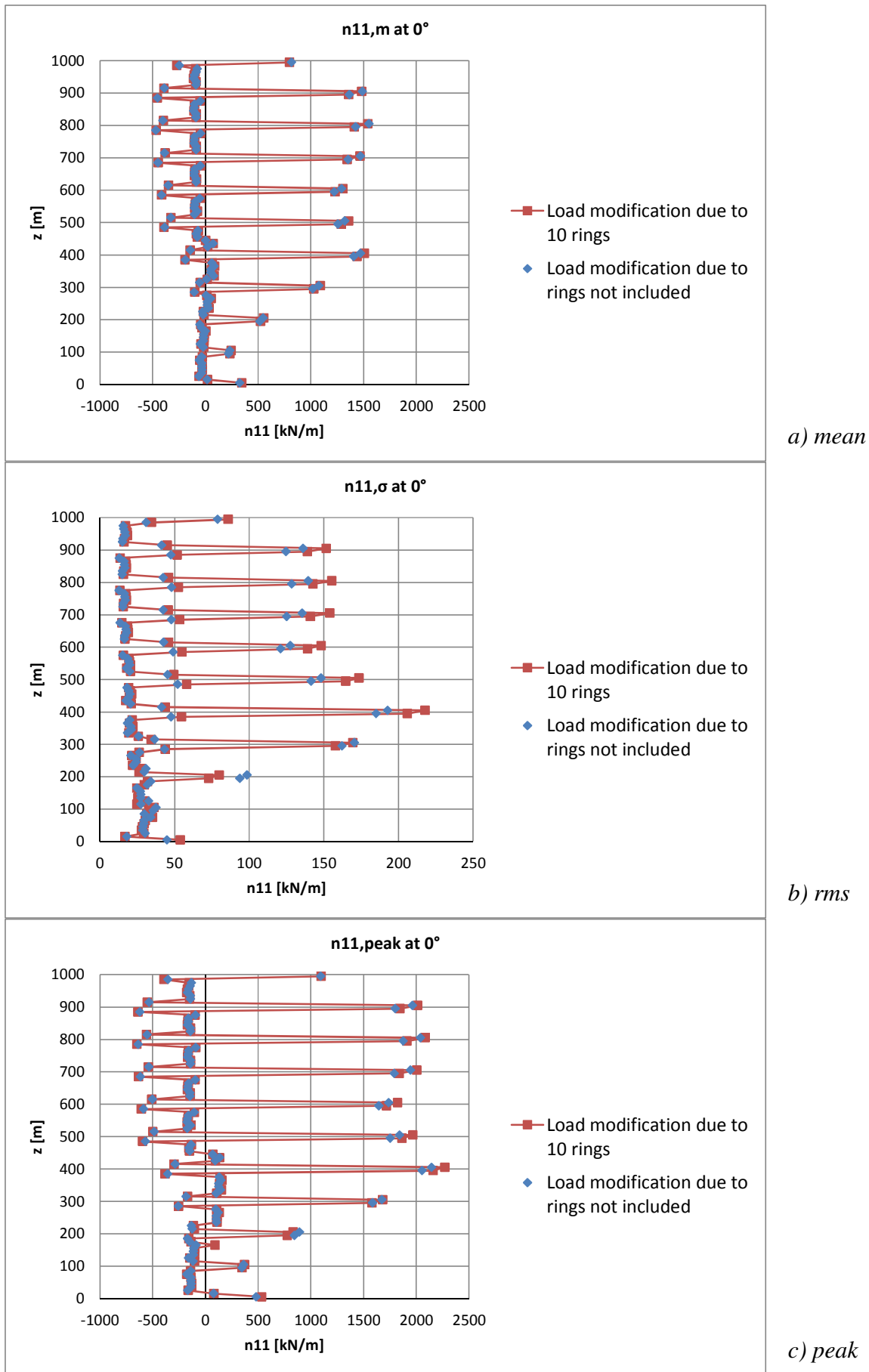
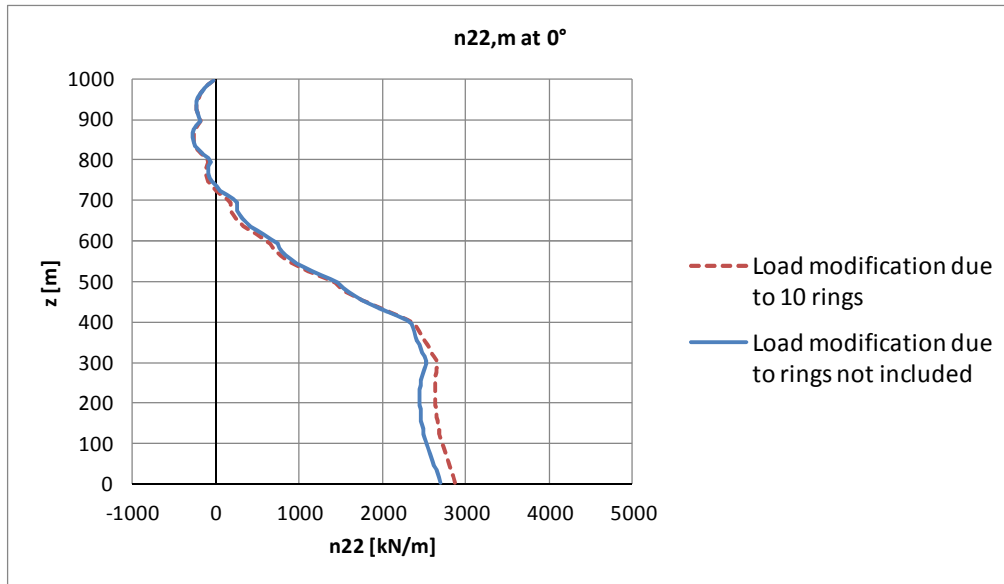
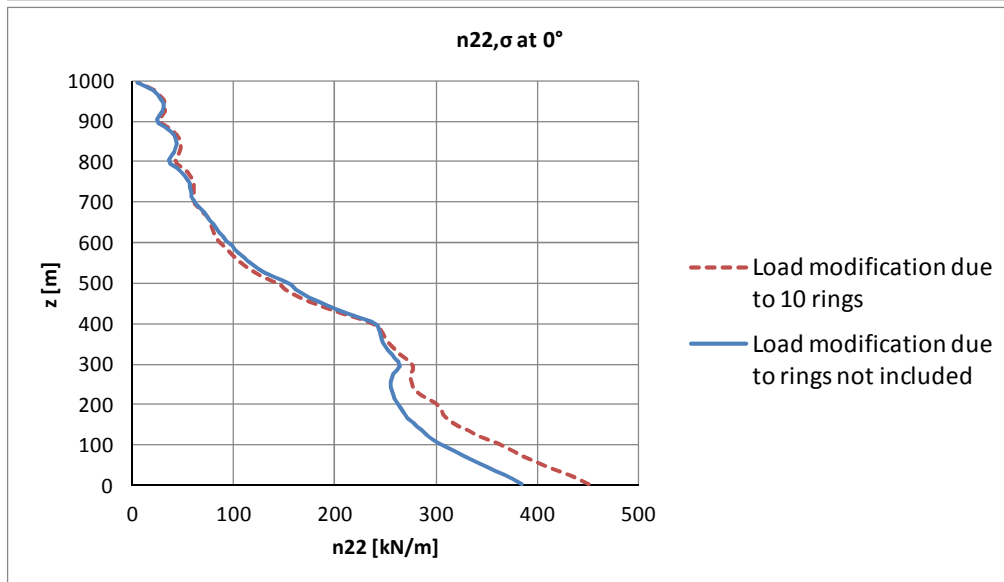


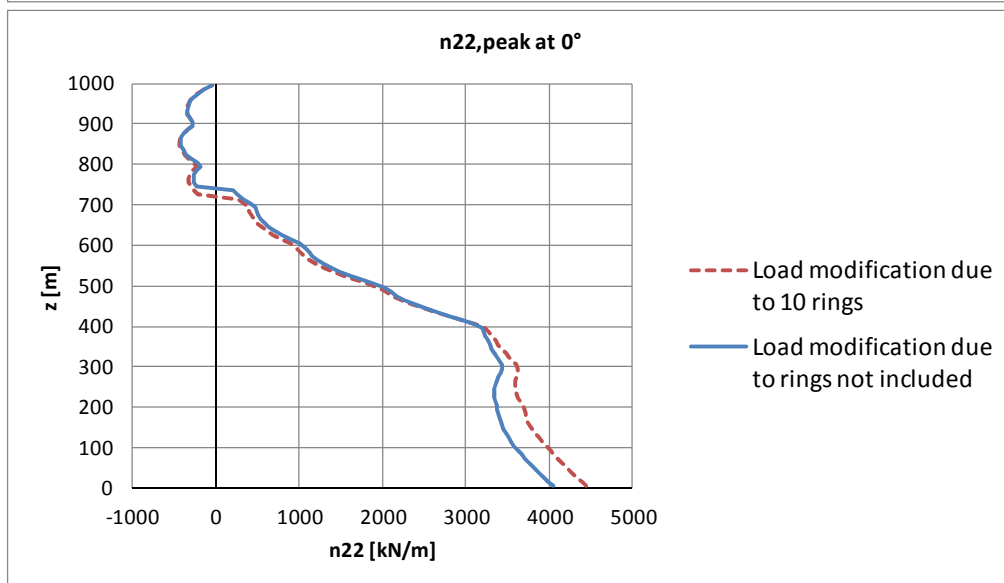
Figure 7.62 Effect of the rings on the quasi-static response (n_{11})



a) mean



b) rms



c) peak

Figure 7.63 Effect of the rings on the quasi-static response (n_{22})

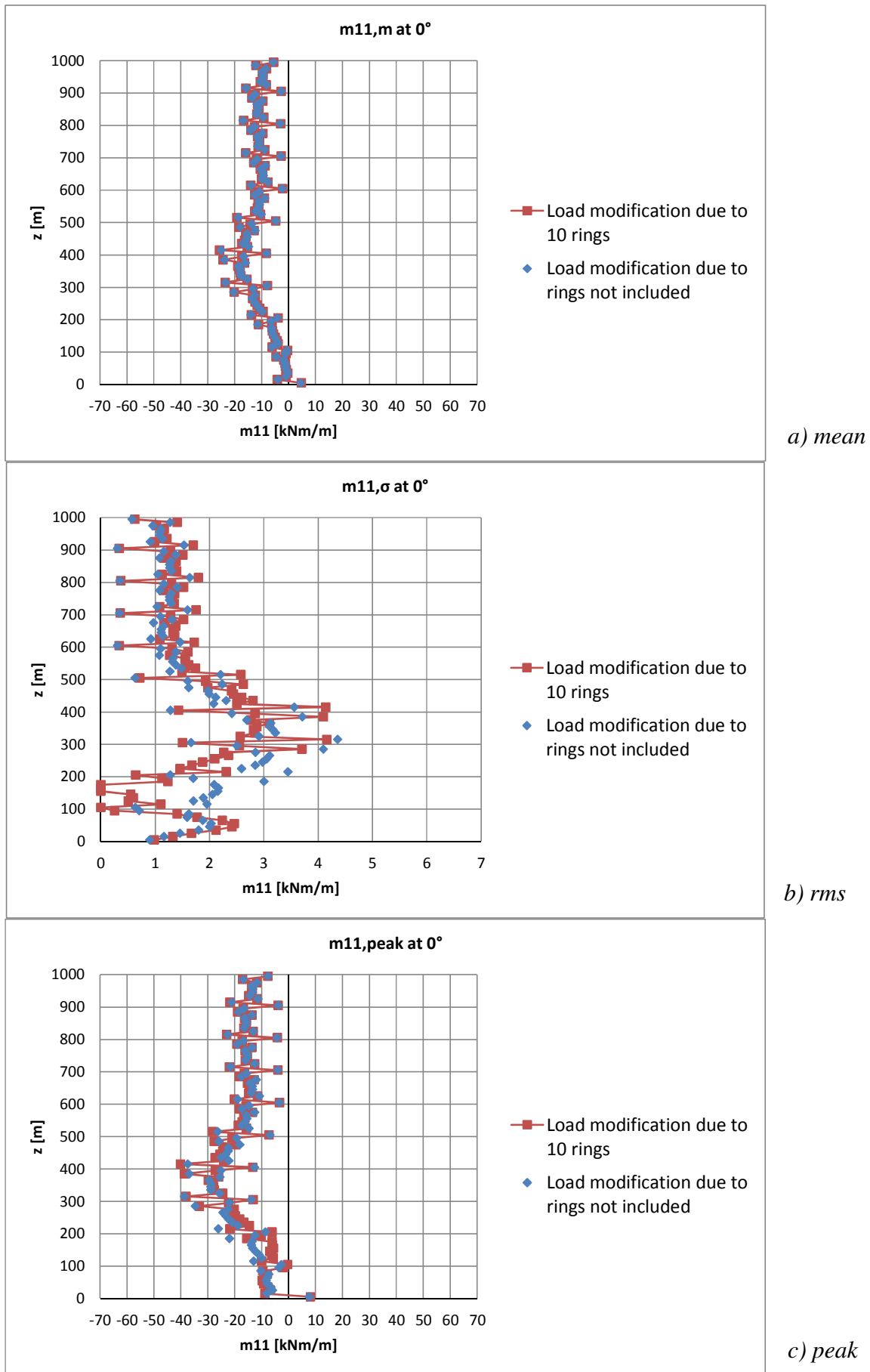


Figure 7.64 Effect of the rings on the quasi-static response (m_{11})

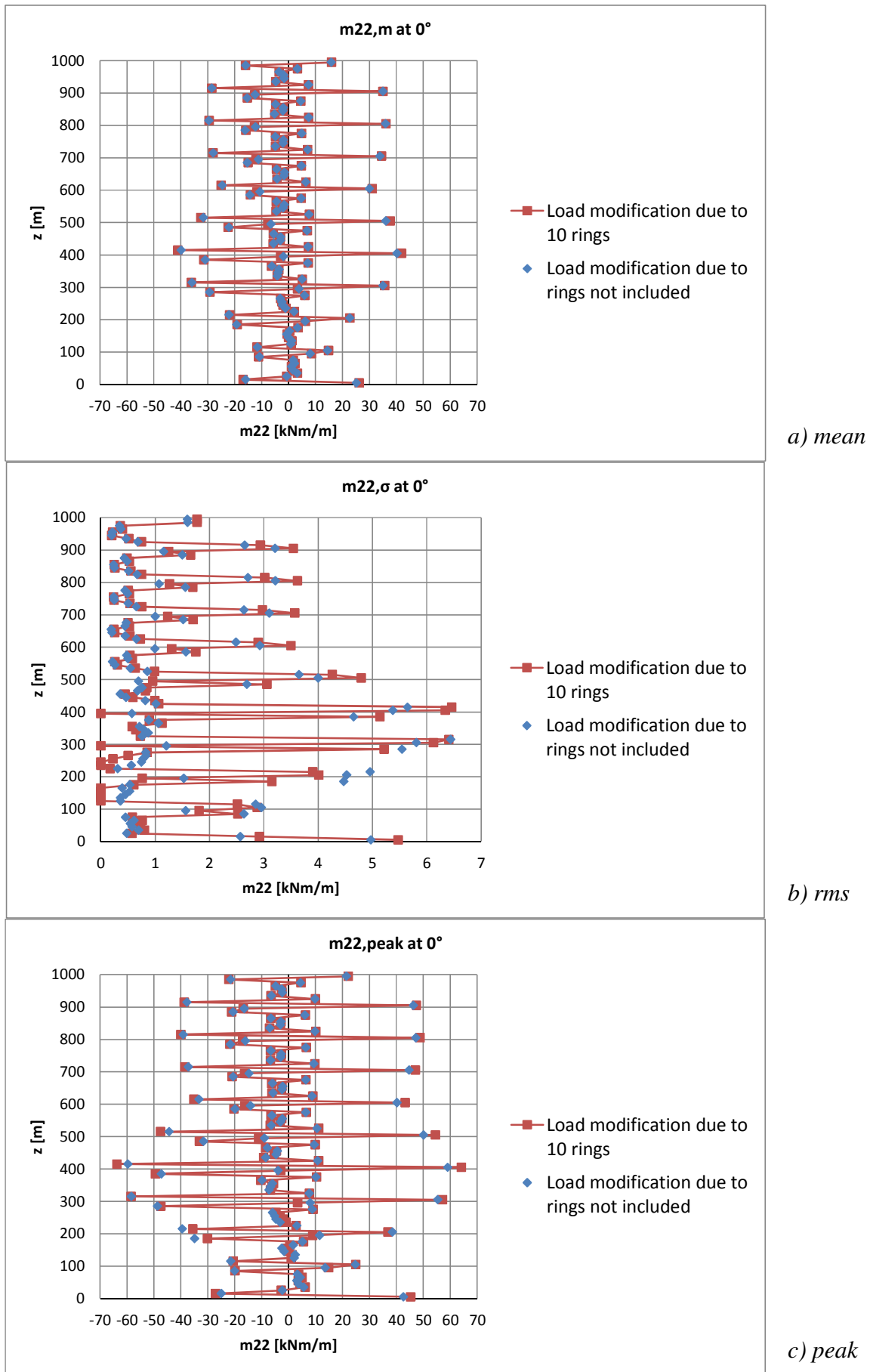


Figure 7.65 Effect of the rings on the quasi-static response (m_{22})

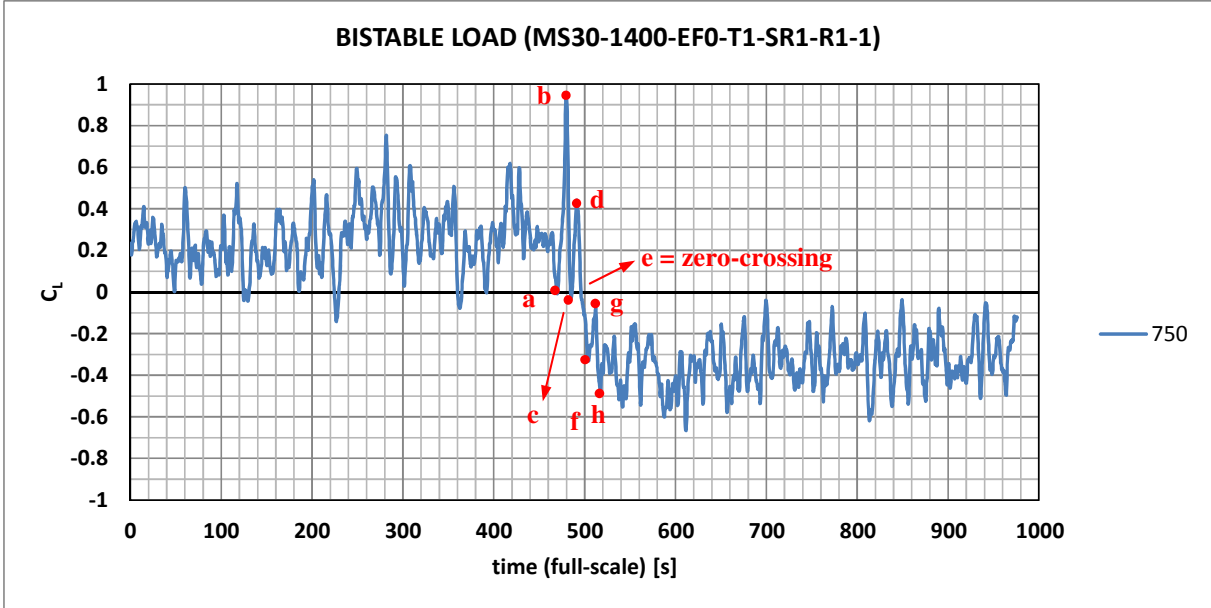


Figure 7.66 Bistable load on the structure: change of state

Chapter 8. Conclusions and future outlooks

The dissertation studies the Aeolian risk scenario in the design of ultra-high structures exposed to strong winds in the atmospheric boundary layer. Solar updraft towers represent the main application and constitute the thread of the dissertation.

A deeper knowledge of the natural hazard - the wind action - at large heights and also at small latitudes in the atmospheric boundary layer is addressed in Chapter 2. In the design of ultra-high structures, the coupling between wind engineering and boundary layer meteorology becomes stronger and it cannot benefit of experimental data, which are scarce at large heights and even inexistent in strong wind conditions. Therefore, Chapter 2 approaches the problem at first on theoretical bases, and then outlines the possible experimental and numerical investigations which could support future studies.

Then, the aerodynamic study of the flow around circular cylinders is required for the design of towers with circular cross-section. A large amount of literature has been written on the topic and it is reviewed in Chapter 3. However, the flow around circular cylinders is so sensitive to many either governing or influencing parameters (such as Re , aspect ratio, free-end, characteristics of the boundary layer...), that a unified and systematic investigation is currently not available to the designer.

In Chapter 4, the dissertation investigates the flow around a circular cylinder of finite length through wind tunnel tests at WiSt laboratory (Ruhr-University Bochum). The full understanding of such a reference case study is the basis to interpret the effect of spanwise rings along the height of the tower.

The discovery and the physical interpretation of a new phenomenon around circular cylinders, induced by stiffening rings along the height, is the original contribution of this research. The phenomenon is described in Chapter 5 on the basis of WiSt wind tunnel results. An asymmetric and bistable flow condition establishes around a symmetric structure like a circular cylinder and it does not disappear at moderately high Reynolds numbers, far beyond the Re_{cr} .

The debate between literature and novelty, between similar effects in completely different physical contexts, encouraged the deep investigation of this asymmetric and bistable flow condition. Similar cases of bistable flows are also described in literature.

They are well-known for example on isolated cylinders in the critical range of the Reynolds number, as well as on side-by-side cylinders. But despite the similarities, the physical reasons appeared to be profoundly different. This immediately resulted from the analysis of the conditions of occurrence. The Reynolds numbers at which this new bistable phenomenon occurs are not limited to a small range around Re_{cr} . The effect can also be considered as a sort of interaction phenomenon. However, the interaction is not between wide and narrow wakes, like in the case of side-by-side cylinders, but between the wake in different spanwise compartments along the height. In fact, the peculiar characteristic of the cylinder, which is responsible for the occurrence of the phenomenon, is the presence of spanwise rings at a certain distance along the height of the tower. The contribution of the flow over the tip seems to play a key role, so that the phenomenon is a cascade effect, alternated in different compartments, towards the base of the tower.

In order to confirm and provide experimental evidence of the same asymmetric bistable flow condition even in a different wind tunnel, the experiments are repeated on the same model at CRIACIV wind tunnel at University of Florence and documented in Chapter 6. It is confirmed that the phenomenon does not depend on some local conditions or disturbances of a certain laboratory, but it is induced by the ring beams. It is also confirmed that in the moderately high range of Re which was investigated on the rough cylinder (up to $Re = 3 \cdot 10^5$), the effect does not disappear. So far, no reason has been identified, which may suggest the disappearance of the phenomenon at higher Reynolds numbers, e.g. in full-scale conditions.

A further proof is provided by numerical simulations (Chapter 6). They have been performed on the basis of CRIACIV experiments by the TEE group, in the Industrial Energy Department at the University of Florence. The CFD simulation reproduces the experimental conditions but it benefits of two additional important aspects: ideal conditions and higher Reynolds numbers (in the order of 10^7 , obtained by reduction of air viscosity). Even in this case, the asymmetric bistable phenomenon appears.

Therefore, the thesis can state that under peculiar conditions (the presence of spanwise rings along a circular cylinder of finite length), an asymmetric flow tends to stabilize around a symmetric structure. Random jumps occur in the time histories and reverse the situation. The wind tunnel experiments confirmed that the phenomenon belongs to one of those paradoxical cases where the symmetric flow structure appears to be intrinsically unstable and hence impossible. This was cited by Zdravkovich (2003)

concerning side-by-side cylinders, but the concept seems to be perfectly fitting also to the case of an isolated cylinder with spanwise rings.

Furthermore, this type of asymmetric flow is not only an interesting fluid dynamic phenomenon. In fact, the presence of rings along the height of the tower, which are responsible for creating the effect, has an important structural function. In many pre-designs of the solar tower, stiffening rings were introduced in order to reduce the structural vulnerability to the wind action. They enhance a beam-like behaviour and reduce the peaks of tension at the windward side. They also increase the buckling stiffness. The stiffening rings were then considered, for the solar tower, a strategy to mitigate the structural risk. However, the effect of the rings on the load had never been investigated before, so it was not expected that the improvement in the structural behaviour might also be responsible for an even more severe load condition. This increases the structural damage. For this reason, the effect of the fluid dynamic phenomenon had to be quantified in terms of structural response. Fortunately, the increase in internal forces did not result to be dramatic (in the order of 10-15%), but the designer should be aware that reduction of structural vulnerability, by adding stiffening rings, can become a double-edge sword. Because of that, further design conditions (with a different number and/or size of rings), as well as mitigation strategies are also investigated in this work. It resulted that the asymmetric bistable flow tends to disappear as the rings become smaller and/or at larger distance. Moreover, the presence of efflux inside the chimney is a natural rescue.

A further contribution of the research is the development of a stochastic load model to be used in quasi-static calculations of the tower in any atmospheric boundary layer flow. It could be developed thanks to the comparative studies between WiSt and CRIACIV results, which allowed to investigate the dependency of wind forces and pressures on the characteristics of the atmospheric boundary layer. This tool allows the designer to evaluate the structural damage even in the vicinity of the stiffening rings, where the shell-like behaviour predominates and no load model was available before.

The dissertation suggested many interesting aspects and new ideas, which would deserve further investigation in the future.

The asymmetric and bistable flow discovered in this work was completely unknown, so there are many issues which should be further addressed. The results suggested that the bistable asymmetric flow is a three-dimensional phenomenon, related to the flow

structures which develop around the free-end. This explains also the disruption along the height. In view of that, experiments in two dimensional conditions are recommended as a further proof. Moreover, it would also be important to test the influence of the aspect ratio of the cylinder. In any case, even if the phenomenon is related to the free-end condition, it is not the top ring alone which initiates the effect. In fact, in the case, for example, of five rings (instead of ten) the top ring is still there but the phenomenon disappears. This suggests to study the distribution of rings in the tip region more in detail. The thesis proved, by experiments, that equally distributed rings at sufficiently large distance mitigate the effect. However, the designer might need rings at smaller distance. Because of that, an important result would be to know whether it is sufficient, in order to mitigate the phenomenon, to outdistance the rings only in the tip region, as supposed in Chapters 5 and 6 on the basis of these results.

The CFD simulations presented in Chapter 6 are just at their first stage. The time window of the URANS is presently too short to be representative. More periods should be investigated. If it is the case, a large eddy simulation could allow to better investigate the bistability of the flow, being the bistability a stochastic effect.

Wind tunnel tests at higher Reynolds numbers on a smooth cylinder in three dimensional conditions would represent a decisive result to confirm what has been stated in this dissertation by using the concept of effective Reynolds number.

Moreover, the three dimensional correlation field should be investigated more extensively in the wind tunnel. This would allow to refine results in Chapter 7. A future aim of the research is to develop a simpler wind load model, e.g. an equivalent static wind load, which could be easily used to evaluate local effects. The approach could be the same as for cooling towers, by using the load response correlation method (Niemann, 1998).

The dynamic response of the solar tower should be further investigated, too. In the case of rings, a dynamic effect could rise within the jump. In this regard, it would be important to characterize the bistable pressure field and model bistable time histories. Moreover, the non-linear behaviour should be included in the analyses.

Chapter 9. Bibliography

- Achenbach E. (1968). Distribution of local pressure and skin friction around a circular cylinder in cross-flow up to $Re=5 \times 10^6$. *Journal of Fluid Mechanics*, 34, 625-639.
- Achenbach E. (1971). Influence of surface roughness on the cross-flow around a circular cylinder. *Journal of Fluid Mechanics*, 46, 321-335.
- Achenbach E., Heinecke E. (1981). On vortex shedding from smooth and rough cylinders in the range of Reynolds numbers 6×10^3 to 5×10^6 . *Journal of Fluid Mechanics*, 109, 239-251.
- Afgan I., Moulinec C., Prosser R., Laurence D. (2006). Large eddy simulation of turbulent flow for wall mounted cantilever cylinders of aspect ratio 6 and 10. *International Journal of heat and fluid flow*, 28 (4), 561-574.
- Augusti G., Borri C., Niemann H.-J. (2001). Is aeolian risk as significant as other environmental risks? *Reliability Engineering and System Safety*, 74 (3), 227-237.
- Ayoub A., Karamcheti K. (1982). An experiment on the flow past a finite circular cylinder at high subcritical and supercritical Reynolds numbers. *Journal of Fluid Mechanics*, 118, 1-26.
- Backström T.W. von, Fluri T.P. (2006). Maximum fluid power condition for solar chimney power plants – An analytical approach. *Solar Energy*, 80, 1417-1423.
- Backström T.W. von, Harte R., Höffer R., Krätzig W.B., Kröger D.G., Niemann, H.-J., van Zijl, G.P.A.G. (2008). State and Recent Advances of Solar Chimney Power Plant Technology. *VGB PowerTech*, 88 Vol. 7, 64-71.
- Backström T.W. von, Fluri T.P. (2010). Solar chimney turbine layout and design considerations. *Proc. 2nd Int. Conf. Solar Chimney Power Technology*, 239-246. Ruhr-Universität Bochum and Bergische Universität Wuppertal.
- Baker, C.J. (1980). Vortex flow around the bases of obstacles. Dissertation, Cambridge.
- Baker, C.J. (1980). The turbulent horseshoe vortex. *Journal of Wind Engineering and Industrial Aerodynamics*, 6 (1-2), 9-23.
- Baker, C.J. (1991). Oscillation of horseshoe vortex systems. *Journal of Fluids Engineering, Transactions of the ASME*, 113 (3), 489-495.

- Banakh V.A., Smalikho I.N., Köpp F., Werner C. (1995). Representativeness of wind measurements with a cw Doppler lidar in the atmospheric boundary layer. *Applied Optics*, 34 (12), 2055-2067.
- Bange J. (2007). Airborne measurement of turbulent energy exchange between the earth surface and the atmosphere. Habilitationsschrift, Technical University Braunschweig, Germany.
- Basu, R.I. (1985). Aerodynamic forces on structures of circular cross-section. Part 1. Model-scale data obtained under two-dimensional conditions in low-turbulence streams. *Journal of Wind Engineering and Industrial Aerodynamics*, 21 (3), 273-294
- Basu, R.I. (1986). Aerodynamic forces on structures of circular cross-section. Part 2. The influence of turbulence and three-dimensional effects. *Journal of Wind Engineering and Industrial Aerodynamics*, 24 (1), 33-59.
- Batham J.P. (1973). Pressure distributions on circular cylinders at critical Reynolds numbers. *Journal of Fluid Mechanics*, 57, 209-228.
- Bearman P.W. (1969). On vortex shedding from a circular cylinder in the critical Reynolds number regime. *Journal of Fluid Mechanics* 37 (3), 577-585.
- Bearman P.W., Wadcock A.J. (1973). The interaction between a pair of circular cylinders normal to a stream. *Journal of Fluid Mechanics*, 61, 499-511.
- Belik L. (1973). The secondary flow around circular cylinders mounted normal to a flat plate. *Aero. Quart.*, 29, 47-54.
- Bénard H. (1908). Formation of centres of circulation behind a moving obstacle (in French). *Comptes Rendus Academie des Sciences*, 147, 839-842.
- Bendat J.S., Piersol A. (1993). *Engineering Applications of Correlation and Spectral Analysis*. John Wiley&Sons, Inc.
- Bendat J.S., Piersol A. (2000). *Random Data, analysis and measurement procedures*. John Wiley&Sons, Inc.
- Bennett A.R. (1896). An improved differential temperature air motor, adapted for scientific applications, for philosophical toys, for advertising and for other purposes. A.D. 1896, n. 8711. Printed by Darling and Son Ltd, London.
- Bergemann R., Weinrebe G. (2010). Realization and costs of solar updraft towers. *Proceedings of the SCPT 2010 – International Conference on Solar Chimney Power Technology*, 63-68. Ruhr-University Bochum and Bergische Universität Wuppertal, Bochum, Germany.

- Bernardes M.A.d.S. (2004). Technische, ökonomische und ökologische Analyse von Aufwind-kraftwerken. Dr.-Ing. Thesis, University of Stuttgart.
- Bernardes M.A.d.S. (2012). On the heat storage in solar updraft towers collectors. Proc. 3rd Int. Conf. on Solar Updraft Power Technology SUTPT 2012, 13-25. HUST, Wuhan, China.
- Bloor M.S., Gerrard J.H. (1966). Measurements on turbulent vortices in a cylinder wake. Proceedings of the Royal Society of London, Series A (Mathematical and Physical Sciences), 294 (1438), 319-342.
- Borri C., Pastò S. (2006). Lezioni di Ingegneria del Vento. Firenze University Press.
- Borri C., Lupi F., Marino E. (2010). Optimum Shell Design of Solar Updraft Towers. Proc. 2nd Int. Conf. Solar Chimney Power Technology, Ruhr-Universität Bochum and Bergische Universität Wuppertal, 155-162.
- Breuer W., Hüwe A (2010). Solar chimney power plants – An economist's point of view. International Conference on Solar Chimney Power Technology, 55-61. Ruhr-University Bochum and Bergische Universität Wuppertal, Bochum, Germany.
- Britter R.E., Hunt J.C.R., Mumford J.C. (1979). The distortion of turbulence by a circular cylinder. Journal of Fluid Mechanics, 92 (2), 269-301.
- Buresti G. (1981). The effect of surface roughness on the flow regime around circular cylinders. Journal of Wind Engineering and Industrial Aerodynamics, 8 (1-2), 105-114.
- Buresti G. (2012). Elements of Fluid Dynamics. Ed. Imperial College Press.
- Cabanyes I. (1903). Las chimeneas solares (Solar chimneys). La energia eléctrica. Cited due to Wikipedia.
- Canadillas B. (2010). A study of the marine boundary layer by LES-modelling and experimental observations with a focus on offshore wind energy applications. Gottfried Wilhelm Leibniz Universitaet Hannover.
- Clobes M., Willecke A., Peil U. (2009). A refined analysis of guyed masts in turbulent wind. Proc. 5th European and African Conference on Wind Engineering, EACWE 5, Florence, Italy.
- Clobes M., Willecke A. (2009). On the numerical simulation of gust and vortex excitation of guyed masts. IASS 24th meeting, Helsinki.
- Cook N.J. (1985). Designer's Guide to Wind Loading of Building Structures Part 1: Background, Damage Survey, Wind Data&Structural Classification. Department of the Environment Building research establishment.

- Cook N.J. (1997). The Deaves and Harris ABL model applied to heterogeneous terrain. *Journal of Wind Engineering and Industrial Aerodynamics*, 66, 197-214.
- Counihan J. (1969). An improved method of simulating an atmospheric boundary layer in a wind tunnel. *Atmospheric Environment* 3 (2), 197-214.
- Couregelongue J. (1929). On the existence of two families of eddies behind immersed solids (in French). *Comptes Rendus Academie Sciences*, 189, 972-974.
- Courtney M., Wagner R., Lindelöw P. (2008). Testing and comparison of lidars for profile and turbulence measurements in wind energy. *IOP Conference Series: Earth and Environmental Science*, 1.
- Crandall S.H., Mark W.D. (1963). *Random Vibration in Mechanical Systems*. Academic Press, New Yoerk and London.
- Csanady G.T. (1967). On the resistance law of a turbulent Ekman layer. *Journal of the Atmospheric Sciences*, 24 (5), 467-471.
- Davies F., Collier C.G., Bozier K.E., Pearson G.N. (2003). On the accuracy of retrieved wind information from Doppler lidar observations. *Quart. Journal. Royal. Meteorology. Society*. 129, 321-334.
- Deaves D.M. (1981). A note on the upper boundary conditions for turbulence models in the neutral atmosphere. *Boundary Layer Meteorology*, 21 (4), 489-493.
- Deaves D.M., Harris R.I (1982). A note on the use of asymptotic similarity theory in neutral atmosphere boundary layers. *Atmospheric Environment*, 16 (8), 1889-1893.
- DIN EN 4133 (2009). German industrial standards: Steel stack / Chimneys built of Steel.
- Durbin P.A., Hunt J.C.R. (1980). On surface pressure fluctuations beneath turbulent flow round bluff bodies. *Journal of Fluid Mechanics*, 100 (1), 161-184.
- Dyrbye C., Hansen S.O. (1997). *Wind Loads on Structures*. John Wiley & Sons.
- Eaddy M. (2004). Lift forces on smooth and rough circular cylinders in low and high turbulence flows. Dissertation. Monash University, Victoria.
- Eisner F. (1925). Pressure measurements in flow cylinders. *Zeitschrift für angewandte Mathematik und Mechanik*, 5, 486-489.
- Ekman (1905). Influence of the Earth's rotation on ocean currents. *Arkiv for Matematik, Astronomioch Fysik*, 2 (11), 1-52.
- Emeis S., Harris M., Banta R.M. (2007). Boundary-layer anemometry by optical remote sensing for wind energy applications. *Meteorologische Zeitschrift*, 16 (4), 337-347.

- Emeis S. (2010). Surface-Based Remote Sensing of the Atmospheric Boundary Layer. Atmospheric and Oceanographic Sciences Library. Springer.
- EN 1990:2001-11, Eurocode - Basis of structural design, CEN 2001.
- ESDU 71012, Fluid forces on non-streamline bodies - background notes and description of the flow phenomena, Engineering Sciences Data Unit, London.
- ESDU 74030, Characteristics of atmospheric turbulence near the ground. Part I: definitions and general information, Engineering Sciences Data Unit, London.
- ESDU 80025, Mean forces, pressures and flow field velocities for circular cylindrical structures: single cylinder with two-dimensional flow, Engineering Sciences Data Unit, London.
- ESDU 81017, Mean forces, pressures, and moments for circular cylindrical structures: finite-length cylinders in uniform and shear flow, Engineering Sciences Data Unit, London.
- ESDU 82026, Strong Winds in the Atmospheric Boundary Layer. Part 1: Mean hourly wind speeds, Engineering Sciences Data Unit, London.
- ESDU 83045, Strong Winds in the Atmospheric Boundary Layer. Part 2: Discrete Gust Speeds, Engineering Sciences Data Unit, London.
- ESDU 85020, Characteristics of atmospheric turbulence near the ground. Part II: single point data for strong winds (neutral atmosphere), Engineering Sciences Data Unit, London.
- ESDU 86010, Characteristics of atmospheric turbulence near the ground. Part III: variations in space and time for strong winds (neutral atmosphere), Engineering Sciences Data Unit, London.
- ESDU 96030, Response of structures to vortex shedding, Engineering Sciences Data Unit, London.
- Fage A. (1928). The air flow around circular cylinder in the region where boundary layer separates from the surface. Aeronautical Research Council, Rep&Memo 1179.
- Fage A, and Warsap J.H. (1929). The effects of turbulence and surface roughness on the drag of a circular cylinder. Aeronautical Research Council, Rep.&Memo 1253.
- Farrell C., Blessmann J. (1983). On critical flow around smooth circular cylinders. *Journal of Fluid Mechanics*, 136, 375-391.
- Farivar Dj. (1981). Turbulent uniform flow around cylinders of finite length. *AIAA Journal*, 19 (3), 275-281.

- Fasel H. F. (2012). Fluid dynamics and heat transfer analysis of geometrically scaled models of solar updraft tower plants using CFD. Proc. 3rd Int. Conf. on Solar Updraft Power Technology SUTPT 2012, 126-127. HUST, Wuhan, China.
- Ferziger J.H., Peric M. (2002). Computational Methods for Fluid Dynamics. Springer.
- Fluri T.P. (2008). Turbine layout for and optimization of solar chimney power conversion units. Ph.D. thesis, University of Stellenbosch.
- Fluri T.P., Backström T.W. von (2008). Performance analysis of the power conversion unit of a solar chimney power plant. *Solar Energy*, 82 (11), 999-1008.
- Fox T. A., West G.S. (1990). On the use of end plates with circular cylinders in wind tunnel studies. Research Report Series - University of Queensland, Department of Civil Engineering, CE118, 1-17
- Fox T.A., West G.S. (1993). Fluid-Induced Loading of Cantilevered Circular Cylinders in a Low-Turbulence Uniform Flow. Part 1: Mean Loading with Aspect Ratios in the Range 4 to 30. *Journal of Fluids and Structures*, 7 (1), 1-14.
- Fox T.A., West G.S. (1993). Fluid-Induced Loading of Cantilevered Circular Cylinders in a Low-Turbulence Uniform Flow. Part 2: Fluctuation Loads on a Cantilever of Aspect Ratio 30. *Journal of Fluids and Structures*, 7, (1), 15-28.
- Fox T.A., Apelt C.J. (1993). Fluid-Induced Loading of Cantilevered Circular Cylinders in a Low-Turbulence Uniform Flow. Part 3: Fluctuating Loads with Aspect Ratios 4 to 25. *Journal of Fluids and Structures*, 7 (4), 375-386.
- Fox T.A., Apelt C.J., West G.S. (1993). The aerodynamic disturbance caused by the free-ends of a circular cylinder immersed in a uniform flow. *Journal of Wind Engineering and Industrial Aerodynamics*, 49 (1-3), 389-399.
- Fröhlich J., Rodi W. (2004). LES of the flow around a circular cylinder of finite height. *International Journal of Heat and Fluid Flow*, 25 (3), 537-548.
- Garg R.K., Niemann H.-J. (1995). On three dimensionality of fluctuating aerodynamic forces on circular cylindrical structures. Proc. of the 9th International Conference on Wind Engineering, New Delhi, India.
- Gerrard, J.H. (1966). Three-dimensional structure of wake of circular cylinder. *Journal of Fluid Mechanics*, 25, 143-164.
- Gerrard J.H. (1978). The wakes of cylindrical bluff bodies at low Reynolds number. *Philosophical Transactions of the Royal Society of London A (Mathematical and Physical Sciences)*, 288 (1354), 351-382.

- Gill A.E. (1968). Similarity theory and geostrophic adjustment. *Journal Royal Meteorology Society*, 94, 586-588.
- Goldack A. (2004). Tragverhalten und Aussteifung hoher Stahlbetonrohren fuer Aufwindkraftwerke (Load-bearing behaviour and stiffening of high-rise RC-tubes for updraft power plants). Dissertation, University of Stuttgart. (in German).
- Goldack A. (2011). Natural frequencies and Mode Shapes of Towers for Solar Updraft Power Plants. Proc. 8th Int. Conf. Structural Dynamics, EUROLYN 2011, Leuven, Belgium, 3575-3581.
- Goliger A. M., Milford R. V. (1998). A review of worldwide occurrence of tornadoes. *Journal of Wind Engineering and Industrial Aerodynamics*, 74/76, 111-121.
- Gould R.W.E., Raymer W.G., Ponsford P.J. (1968). Wind tunnel tests on chimneys of circular section at High Reynolds Number. Proceedings of the Symposium on wind effects on buildings and structures, Loughborough.
- Günther H. (1931). In hundert Jahren - Die künftige Energieversorgung der Welt (In hundred years – World's future energy supply). Kosmos, Franckh'sche Verlagshandlung Stuttgart.
- Güven O., Farrell C., Patel V.C. (1980). Surface-roughness effects on the mean flow past circular cylinders. *Journal of Fluid Mechanics*, 98 (4), 673-701
- Güven O., Farrell C., Patel V.C. (1983). Boundary-layer development on a circular cylinder with ribs. *Transactions of the ASME. Journal of Fluids Engineering*, 105 (2), 179-184.
- Haan F.L., Sarkar P.P., Gallus W.A. (2008). Design construction and performance of a large tornado simulator for wind engineering applications. *Engineering Structures*, 30, 1146-1159.
- Hardesty R.M., Darby L.S. (2005). Ground-based and airborne lidar. *Encyclopedia of Hydrologic Sciences*. Malcolm G. Anderson (Ed.), Wiley, 697–712.
- Harris R.I., Deaves D.M. (1980). The structure of strong winds. Proc. CIRIA Conference. London, Construction Industry Research and Information Association.
- Harris R.I. (1986). Longer turbulence length scales. *Journal of Wind Engineering and Industrial Aerodynamics*, 24 (1), 61-68.
- Harris M., Constant M., Ward C. (2001). Continuous wave bistatic laser Doppler wind sensor. *Applied Optics*, 40, 1501–1506.
- Harte R., Graffmann M., Wörmann R. (2010). Progress in the Structural Design of Solar Chimneys. Proc. 2nd Int. Conf. Solar Chimney Power Technology, Ruhr-

- Universität Bochum and Bergische Universität Wuppertal, 145-152, Bochum, Germany.
- Holmes J.D. (2003). *Wind Loading of Structures*. Spon Press, Taylor&Francis Group.
- Hölscher N., Niemann H.-J. (1993). On the flow around finite circular cylinders in turbulent shear flows. *Physics of separated flows – Numerical, experimental and theoretical aspects*. Ed.: Kl. Gersten, Notes on numerical fluid mechanics, Vol 40, pp. 216-244.
- Hölscher N. (1993). Ein multivariater Ansatz fuer die aerodynamische Uebertragungsfunktion der Winddruecke in atmosphaerischer Grenzschichtstroemung. Dissertation 93-3, Ruhr University Bochum.
- Holton J.R. (1979). *An introduction to dynamic meteorology*. Academic Press, New York.
- Houghton J.T. (1977). *The physics of the atmospheres*. Cambridge University Press.
- Hunt J.C.R. (1972). A theory for fluctuating pressures on bluff bodies in turbulent flows. *Symposium on flow-induced structural vibrations*. Karlsruhe, Germany.
- Hunt J.C.R. (1973) A theory of turbulent flow round two-dimensional bluff bodies. *Journal of Fluid Mechanics*, 61, 625-705.
- Hunt J.C.R. (1975) Turbulent velocities near and fluctuating surface pressures on structures in turbulent winds. *Proc. International Conference on Wind Effects on Building and Structures*.
- Hunt J.C.R. (1990). A review of velocity and pressure fluctuations in turbulent flows around bluff bodies. *Journal of Wind Engineering and Industrial Aerodynamics*, 35, 49-85.
- Irwin P. (2009). Wind engineering research needs, building codes and project scientific studies. *Proc. 11th American Conference on Wind Engineering*. San Juan, Puerto Rico.
- Ishigai S., Nishikawa E., Nishimura K., Cho K. (1972). Experimental study on structure of gas flow in tube banks with tube axes normal to flow. *Bulletin of the Japan Society of Mechanical Engineers*, 15 (86), 949-956.
- Isyumov N. (1999). *Wind Tunnel Studies of Buildings and Structures*. ASCE American Society of Civil Engineers.
- Jørgensen Finn E. (2002). *How to measure turbulence with hot-wire anemometers - a practical guide*. Dantec Dynamics.

- Kalash S., Naimeh W., Ajib S. (2012). A simplified analysis of the main parameters affecting the solar updraft power plants. Proc. 3rd Int. Conf. on Solar Updraft Power Technology SUTPT 2012, 101-106. HUST, Wuhan, China.
- Karman Th. von, Rubach H. (1912). On the mechanism of resistance in fluids (in German). *Physikalische Zeitschrift*, 13.
- Kasperski M, Niemann H.-J. (1988). On the correlation of dynamic wind loads and structural response of natural-draught cooling towers. *Journal of Wind Engineering and Industrial Aerodynamic*, 30, 67-75.
- Kawamura T. Hiwada M, Hibino T., Mabuchi I., Kumada M. (1984). Flow around a finite circular cylinder on a flat plate. Cylinder height greater than turbulent boundary layer thickness. *Bulletin of the Japan Society of Mechanical Engineers*, 27 (232), 2142-2151.
- Kindler D., Oldroyd A., Macaskill A., Finch D. (2007). An 8 month test campaign of the QinetiQ ZephIR system: preliminary results. *Meteorologische Zeitschrift*, 16, 463–473.
- Kitagawa T., Fujino Y., Kimura K. (1999). Effects of free-end condition on end-cell-induced vibration. *Journal of Fluids and Structures*, 13 (4), 499-518.
- Kitagawa T., Fujino Y., Kimura K., Mizuno Y. (2001). Wind pressures on end-cell-induced vibration of circular tower. *Journal of Engineering Mechanics*, 127 (11), 1135-1143.
- Kitagawa T., Fujino Y., Kimura K., Mizuno Y. (2002). Wind pressures measurement on end-cell-induced vibration of a cantilevered circular cylinder. *Journal of Wind Engineering and Industrial Aerodynamics*, 90 (4-5), 395-405.
- Kovácsnay, L. S. G. (1949). Hot-Wire Investigation of the Wake behind Cylinders at Low Reynolds Numbers. *Proceedings of the Royal Society of London. Series A, Mathematical and Physical Sciences*, 198 (1053), 174-190.
- Krajnovic, S. (2011). Flow around a tall finite cylinder explored by large eddy simulation. *Journal of fluid mechanics*, 676, 294-317.
- Krätzig W.B., Harte R., Wörmann R. (2008). Large shell structures for power generation technologies. Proc. 6th Int. Conf. IASS-IACM 2008, Cornell University, Ithaca, NY, USA.
- Krätzig W.B., Niemann H.-J., Harte R. and Höffer R. (2009a). Solar Updraft Power Plant with 750 m power towers and collector diameters of 3000 m to 4000 m. Internal manual, Bochum.

- Krätzig W.B., Harte R., Montag U., Woermann R., (2009b). From large natural draft cooling tower shells to chimneys of solar upwind power plants. In: A. Domingo, C. Lazaro (eds.), IASS Symposium on Evolutions and Trends in Design, Analysis and Construction of Shells. CD-Rom, University of Valencia.
- Krätzig W.B., Harte R., Montag U., Graffmann M. (2010). On Structural Engineering Problems of Solar Updraft Chimneys. Proc. 4th Int. Conf. Structural Engineering, Mechanics and Computation, SEMC 2010, Cape Town, South Africa.
- Krätzig W.B., Gould Ph.L., Harte R. (2011). Shell structures for power technology. In: Mungan, I., Abel, J.F. (eds.) Fifty years of progress for shell and spatial structures. International Association for Shell and Spatial Structures (IASS), Madrid, 165-194.
- Krätzig W.B. (2012a). Solar updraft power technology, State and advances of low-concentrated thermal solar power generation. VGB PowerTech 92, Vol. 11, 34-39.
- Krätzig W.B. (2012b). Physics, Computer Simulation and Optimization of Thermo-fluidmechanical Processes of SUPPs. Proceedings 3rd Int. Conf. on Solar Updraft Power Tower Technology SUTPT 2012, 1-12. HUST Wuhan, China.
- Krätzig W.B., Harte R., Graffmann M., Montag U. (2013). Load response and design of Giga-towres. CICIND Report 29 Vol. 1, 55-62.
- Kroonenberg van den A. (2009). Airborne Measurement of Small-Scale Turbulence with special regard to the Polar Boundary Layer. Dissertation. Technical University Carolo-Wilhelmina, Braunschweig.
- Lee T., Lin C.-L., Friehe C.A. (2007). Large-eddy simulation of air flow around a wall-mounted circular cylinder and a tripod tower. Journal of turbulence, 8 (29), 1-28.
- Luo S.C., Gan T.L., Chew Y.T. (1996). Uniform flow past one (or two in tandem) finite length circular cylinder(s). Journal of Wind Engineering and Industrial Aerodynamics, 59 (1), pp. 69-93.
- Lupi F. (2009) Structural behaviour, optimization and design of a solar chimney prototype under wind loading and other actions. Master Thesis, University of Florence in cooperation with Ruhr University Bochum.
- Lupi F., Borri C., Krätzig W.B., Niemann H.-J., (2011). Solar Updraft Power Plant technology: basic concepts and structural design. In Encyclopedia Online of Life Support Systems (EOLSS) developed under the auspices of the UNESCO, Eolss Publishers, Oxford, UK.

- Lupi F., Borri C., Niemann H.-J., Peil U. (2011) Non-conventional wind loading on ultra-high Towers in Solar Updraft Power Plants. *International Journal of Shell and Space Structures*, 52 (4), 257-264.
- Mahbub Alam, Md., Sakamoto, H., Moriya, M. (2003). Reduction of fluid forces acting on a single circular cylinder and two circular cylinders by using tripping rods. *Journal of Fluids and Structures* 18 (3-4), 347-366.
- Mahbub Alam Md., Meyer, J.P. (2011). Two interacting cylinders in cross flow. *Physical Review Section E, Statistical Nonlinear and Soft Matter Physics* 84 (5).
- Mann J., Cariou J.P., Courtney M., Parmentier R., Mikkelsen T., Wagner R., Lindelöw P., Sjöholm M., Enevoldsen K. (2008). Comparison of 3D turbulence measurements using three staring wind lidars and a sonic anemometer. *IOP Conference Series: Earth and Environmental Science*, 1.
- Matsuno T. (1966). Quasi-geostrophical motions in the equatorial area. *Journal Meteorol. Jpn.*, 44, 25-42.
- Mikkelsen T., Mann J., Courtney M., Sjöholm (2008). Windscanner: 3-D wind and turbulence measurements from three steerable Doppler Lidars. *Proc. 14th Int. Symposium for the Advancement of Boundary Layer Remote Sensing*.
- Monin A.S., Yaglom A.M. (1971). *Statistical fluid mechanics: mechanics of turbulence*, Vol. 1. Mit Press, Cambridge.
- Nakamura Y., Tomonari Y. (1982). The effects of surface roughness on the flow past circular cylinders at high Reynolds numbers. *Journal of Fluid Mechanics*, 123, 363-378.
- Neuhaus C. (2009). *Zur Identifikationselbsterregter aeroelastischer Kräfte im Zeitbereich*. Dissertation. Bergische Universität Wuppertal, Germany.
- Neuhaus C. (2010). *Numerische frequenzabhängige Kalibrierung langer Druckmessschlauchsysteme*. Internal report, Windingenieurwesen und Strömungsmechanik, Ruhr-Universität Bochum, Germany.
- Newland D.E. (1993). *An Introduction to Random Vibrations, Spectral & Wavelet Analysis*. Dover Publications, Inc, Mineola, New York.
- Niemann H.-J., Schröder P. (1981). *Konstruktiver Ingenierbau Berichte, Heft 35/36, Gebäudeaerodynamik*. DFG-Kolloquium, Ruhr-Universität Bochum, Germany.
- Niemann H.-J., Hölscher N. (1990). A review of recent experiments on the flow past circular cylinders. *Journal of Wind Engineering and Industrial Aerodynamics*, 33 (1-2), 197-209.

- Niemann H.-J., Flaga A., Höffer R., Hölscher N., Kasperski M. (1996). Structural response to wind. In: Dynamics of Civil Engineering Structures, Wilfried B. Krätzig & Hans-Jürgen Niemann (Eds.) A.A. Balkema, Rotterdam.
- Niemann H.-J. (1998). Wind load modelling in the analysis of very high cooling towers. Proc. Wind effects on buildings and structures, A.A. Balkema.
- Niemann H.-J., Hölscher N., Meiswinkel R. (2007). A probabilistic approach for the determination of extreme actions with respect to the structural design. Proc. of ICAPP 2007, Nice, France.
- Niemann H.-J., Höffer R. (2007). Wind loading for the design of the solar tower. Proc. 3rd Int. Conf. SEMC, Cape Town, South Africa.
- Niemann H.-J. (2008). Prototyp eines Aufwindkraftwerks. Windeigenschaften, winderregte Schwingungen und Windlasten zur Bemessung des Stahlbetonturms. Internal report, Bochum. (in German)
- Niemann H.-J., (2009). A Refined Approach to Wind Loading for the Design of the Solar Tower. CICIND Report, 25 (2).
- Niemann H.-J., Lupi F., Höffer R., Hubert W., Borri C., (2009). The solar updraft power plant: design and optimization of the tower for wind effects. Proceedings of the 5th European and African Conference on Wind Engineering EACWE5, Florence, Italy.
- Niemann H.-J. (2010). Static, quasi-static and resonant wind effects on solar towers. 2nd International Conference on Solar Chimney Power Technology, Ruhr-University Bochum and Bergische Universität Wuppertal, Bochum.
- Okamoto S., Yagita M. (1973). The experimental investigation on the flow past a circular cylinder of finite length placed normal to the plane surface in a uniform stream. Bulletin of the Japan Society of Mechanical Engineers, 16 (95), 805-814.
- Okamoto S., Yagita M. (1984). Flow past circular cylinder of finite length placed normal to ground plane in uniform shear flow. Bulletin of the Japan Society of Mechanical Engineers. 27 (229), 1454-1459.
- Okamoto S., Sunabashiri Y. (1992). Vortex shedding from a circular cylinder of finite length placed on a ground plane. Transactions of the ASME. Journal of Fluids Engineering, 114 (4), 512-521.
- Palau-Salvador G., Stoesser T., Fröhlich J., Kappler M., Rodi W. (2010). Large Eddy Simulations and Experiments of Flow Around Finite-Height Cylinders. Flow, Turbulence and Combustion, 84 (2), 239-275.

- Park C.-W., Lee S.J. (2000). Free end effects on the near wake flow structure behind a finite circular cylinder. *Journal of Wind Engineering and Industrial Aerodynamics*, 88, (2-3), 231-246.
- Park C.-W., Lee S.J. (2002). Flow structure around a finite circular cylinder embedded in various atmospheric boundary layers. *Fluid Dynamics Research*, 30 (4), 197-215.
- Parsumarathi N., Sherif S.A. (1997). Performance of a Demonstration Solar Chimney Model for Power Generation. Proc. 35th Heat Transfer and Mechanics Conference, 203-240. California State University, School of Engg. and Computer Science. Sacramento.
- Peil U., Nölle H. (1990). Measurement of Wind Load and Response of a guyed Mast. Proc. European Conference on Structural Dynamics, Eurodyn '90, Bochum, Germany.
- Peil U., Nölle H., (1992). Guyed masts under wind load. *Journal of Wind Engineering and Industrial Aerodynamics*, 43 (3), 2129-2140.
- Peil U., Nölle H., Wang Z.H. (1996). Dynamic behaviour of guys under turbulent wind load. *Journal of Wind Engineering and Industrial Aerodynamics*, 65 (1-3), 43-54.
- Peil U., Nölle H., (1998). Stress distribution in steel chimneys. CICIND, Proc. 6th International Chimney Conference, 1. Brighton, England.
- Plate E.L. (1982). *Engineering meteorology*. Elsevier Scientific Publishing Company.
- Pliefke T. (2010). Public Investments in Disaster Risk Reduction – A Social Cost Benefit Analysis. Dissertation. Technical University of Braunschweig, University of Florence.
- Pope S.B. (2000). *Turbulent flows*. Cambridge University Press.
- Prandtl L. (1904). Fluid motion with very small friction (in German). Proc. of the 3rd International Mathematical Congress, 484-491.
- Pretorius J.P., Kröger D.G. (2006). Solar Chimney Power Plant Performance. *ASME J. Solar Energy Engineering* 128, 302-311.
- Pretorius J.P. (2007). Optimization and Control of a Large-Scale Solar Chimney Power Plant, PhD-Thesis, University of Stellenbosch.
- Pretorius J.P., Kröger D.G. (2010). Basic theory and numerical simulation of large scale solar updraft power plants. Proc. 2nd Int. Conf. Solar Chimney Power Technology, 45-54. Ruhr-Universität Bochum and Bergische Universität Wuppertal.

- Procino L. (2010). Profilo mare. Internal report, CRIACIV.
- Pröpper H. (1977) Zur aerodynamischen Belastung großer Kühltürme. Dissertation 77-3, Ruhr-Universität Bochum, Germany.
- Raasch S., Etling D. (1991). Numerical simulation of rotating turbulent thermal convection. *Beitr. Phys. Atmos.* 64, 185-199.
- Raasch S., Etling D. (1998). Modelling deep ocean convection: large eddy simulation in comparison with laboratory experiments. *Journal of Physical Oceanography*, 28, 1786-1802.
- Raasch S., Schröter M. (2001). PALM – A large eddy simulation model performing on massively parallel computers. *Meteorologische Zeitschrift*, 10 (5), 363-372.
- Rayleigh L. (1896). *The theory of sound*.
- Rayleigh L. (1915). Aolian tones. *Philosophical Magazine*, 6th series, 42, 173-176.
- Reynolds O. (1883). An experimental investigation of the circumstances which determine whether the motion of water shall be direct or sinuous, and the law of resistance in parallel channels. *Philosophical Transactions*, 174, 935-982.
- Ribeiro D.J.L. (1991). Effects of surface roughness on the two-dimensional flow past circular cylinders I: mean forces and pressures. *Journal of Wind Engineering and Industrial Aerodynamics*. 37 (3), 299-309.
- Ribeiro D.J.L. (1991). Effects of surface roughness on the two-dimensional flow past circular cylinders II: fluctuating forces and pressures. *Journal of Wind Engineering and Industrial Aerodynamics*. 37 (3), 311-326.
- Roshko A. (1954). On development of turbulent wakes from vortex streets. *National Advisory Committee for Aeronautics, Reports*.
- Roshko A. (1954). On the effect of air pressure on Strouhal number. *Journal of the Aerospace Sciences*, 26 (2), 121.
- Roshko A. (1955). On the wake and drag of bluff bodies. *Journal of the Aeronautical Sciences*, 22 (2), 124-132.
- Roshko A. (1961). Experiments on the flow past a circular cylinder at very high Reynolds number. *Journal of Fluid Mechanics* 10 (3), 345-356.
- Rostamy N., Sumner D., Bergstrom D. J., Bugg J. D (2012). Local flow field of a surface-mounted finite circular cylinder. *Journal of fluid and structures*, 34, 105-122.
- Sagaut P. (2006). *Large eddy simulation for incompressible flows*. Springer, Germany.

- Sakamoto H., Arie M. (1983). Vortex shedding from a rectangular prism and a circular cylinder placed vertically in a turbulent boundary layer. *Journal of Fluid Mechanics*, 126, 147-165.
- Salvadori S.&Mattana A., Barbanti G.&Vita G. (2013). CFD simulations on a Solar Updraft Tower on the basis of CRIACIV experiments, personal communication, unpublished.
- Sathe A., Mann J., Gottschall J., Courtney M.S. (2011). Can wind lidars measure turbulence? *Journal of Atmospheric and Oceanic Technology*, 28 (7), 853-868.
- Schewe G. (1983). On the forces acting on a circular cylinder in cross-flow from subcritical up to transcritical Reynolds numbers. *Journal Fluid Mechanics* 133, 265-285.
- Schlaich J. (1995). *The Solar Chimney, Electricity from the Sun*. Edition A. Menges, Stuttgart.
- Schlaich J., Bergermann R., Schiel W., Weinrebe G. (2005). Design of Commercial Solar Updraft Tower Systems. *ASME J. Solar Energy Engineering*, 127, 117-124.
- Schlaich J. (2010). Concept and motivation of solar updraft power technology. *Proc. 2nd Int. Conf. Solar Chimney Power Technology*, 15-18. Ruhr-Universität Bochum and Bergische Universität Wuppertal, Bochum, Germany.
- Schlichting, H. (1960). *Boundary layer theory*. McGraw-Hill.
- Schrader P. (1993). *Die statistische Stabilität gemessener integraler Längenmaße und anderer Windparameter*. Dissertation, Ruhr-Universität Bochum, Germany.
- Simiu E., Scanlan R.H. (1996). *Wind effects on structures - Fundamentals and application to design*. John Wiley&Sons, Inc. New York.
- Simiu E. (2011). *Design of Buildings for Wind*. John Wiley&Sons, Inc.
- Sjöholm M., Mikkelsen T., Mann J., Enevoldsen K., Courtney M. (2008). Time series analysis of continuous-wave coherent Doppler Lidar wind measurements. *IOP Conference Series: Earth and Environmental Science*, 1 (1).
- Stull R.B. (1988). *An introduction to boundary layer meteorology*. Kluwer Academic Publishers, Dordrecht, The Netherlands.
- SCPT (2010). *Proc. 2nd Int. Conf. on Solar Chimney Power Technology*, Ruhr-Universität Bochum and Bergische Universität Wuppertal, Bochum, Germany.
- Strømme E.N. (2010). *Theory of Bridge Aerodynamics*. Springer.

- Sumner D., Heseltine J.L. (2008). Tip vortex structure for a circular cylinder with a free end. *Journal of Wind Engineering and Industrial Aerodynamics*, 96, 1185-1196.
- Sumner, D. (2010). Two circular cylinders in cross-flow: A review. *Journal of Fluids and Structures* 26 (6), 849-899.
- SUTPT (2012). Proc. 3rd Int. Conf. on Solar Updraft Power Technology SUTPT 2012. HUST, Wuhan, China.
- Szechenyi E. (1974). Simulation of high Reynolds numbers on a cylinder in wind tunnel tests. *Recherche Aerospaciale*, 3, 155-164.
- Szechenyi E. (1975). Supercritical Reynolds number simulation for two-dimensional flow over circular cylinders. *Journal of Fluid Mechanics*, 70, 529-542.
- Tamura Y., Iwatani Y., Hibi K., Suda K., Nakamura O., Maruyama T., Ishibashi R (2007). Profiles of mean wind speeds and vertical turbulence intensities measured at seashore and two inland sites using Doppler sodars. *Journal of Wind Engineering & Industrial Aerodynamics*, 95 (6), 411-427.
- Taniguchi S., Sakamoto H., Arie M. (1981). Flow around a circular cylinder vertically mounted in a turbulent boundary layer. *Bulletin of the Japan Society of Mechanical Engineers*, 24 (193), 1130-1136.
- Taylor G.I. (1916). Pressure distribution round the cylinder. Advisory Committee of Aeronautics, Rep&Memo.
- Teunissen H.W. (1970). Characteristics of the mean wind and turbulence in the planetary boundary layer. UTIAS Review No 32. Institute for Aerospace Studies, University of Toronto.
- Thompson N. (1990). Integral length scales of turbulence: a re-analysis including data from non-uniform terrain. ESDU Memorandum n.76.
- Uematsu Y., Yamada M. (1994). Aerodynamic forces on circular cylinders of finite height. *Journal of Wind Engineering and Industrial Aerodynamics*, 51 (2), 249-265.
- Verkley W.T.M., van der Velde I.R. (2010). Balanced dynamics in the Tropics. *Quarterly Journal of the Royal Meteorological Society*, 136 (646), 41-49.
- Versteeg H.K., Malalasekera W. (1995). *An Introduction to Computational Fluid Dynamics. The Finite Volume Method*. Longman Scientific&Technical.
- VGB (2005). Structural design of cooling towers. Guideline VGB R 610Ue, VGB PowerTech, Essen.

- VGB (2010). Structural design of cooling towers. Guideline VGB R 610e, VGB PowerTech, Essen.
- Waechter M., Rettenmeier A., Kuehn M., Peinke, J. (2009). Characterization of short time fluctuations in atmospheric wind speeds by LIDAR measurements. *Meteorologischezeitschrift*, 18 (3), 277-280.
- Wie Y., Wu Z. (2012). Shed absorbability and tower structure characteristics of the Solar Heated Wind Updraft Tower Power. Proc. 3rd Int. Conf. on Solar Updraft Power Technology SUTPT 2012, 126-127. HUST, Wuhan, China.
- Weinrebe G. (2000). Technische, ökologische und ökonomische Analyse von solarthermischen Turmkraftwerken. Dissertation, University of Stuttgart.
- Zdravkovich M.M. (1987). The effects of interference between circular cylinders in cross flow. *Journal of Fluids and Structures*, 1 (2), 239-261.
- Zdravkovich M. M. (1992). A reflection on two modes of eddy shedding at $Re = 180-300$. Iutam Symposium, Bluff body wakes, Dynamics and Instabilities, Göttingen, 631-639. Springer, Berlin.
- Zdravkovich M. M., Pridden D.L., (1977). Interference between two circular cylinders; Series of unexpected discontinuities. *Journal of Wind Engineering and Industrial Aerodynamics*, 2 (3), 255-270
- Zdravkovich, M. M (1997). Flow around circular cylinders, Vol. 1, Fundamentals. Oxford University Press.
- Zdravkovich, M. M (2003). Flow around circular cylinders, Vol. 2, Applications. Oxford University Press.

Chapter 10. Appendix

10.1 Modelling of wind load (Chapter 7)

Table A.1 Load data: body-induced pressure fluctuations - variance (SR0, effect of the rings on the load not included)

Cp,σ _b ² = body-induced pressure fluctuations										
	0	20	40	60	80	100	120	140	160	180
0.95	0	0	0	1.04E-05	0.0023097	0.0136799	0.0198095	0.0102689	0.0184776	0.0273402
0.85	0	0	5.006E-05	0.00103	0.0074486	0.0411091	0.0128124	0.014862	0.0199033	0.0155416
0.75	0	0	0	0.000128	0.0070256	0.0211319	0.0041208	0.0030748	0.0037577	0.0034584
0.65	0	0	0	0	0.0014349	0.0192708	0.0023672	0.0017146	0.0019685	0.0020286
0.55	0	0	0	0	0	0	0.0005087	0.0002179	0.0009585	0.0010654
0.45	0	0	0	0	0	0	0.0001991	0	0.0004456	0.000387
0.35	0	0	0	0	0	0	0.0007821	0	5.383E-05	0.0002192
0.25	0.0099196	0.0097788	0	0	0.0072963	0	0	0	0	0.0006125
0.15	0.0373687	0.0325377	0.0093249	0.016141	0.0453442	0	0.0143486	0.0123303	0.012928	0.0100694
0.05	0	0	0	0	0.0669672	0	0.0596038	0.0943915	0.1293659	0.0646646

Table A.2 Load data: horizontal correlations tip region 1 (SR0, effect of the rings on the load not included)

TIP REGION N.1																			
	0	20	40	60	80	100	120	140	160	180	200	220	240	260	280	300	320	340	360
0	1.00	0.73	0.10	-0.40	-0.54	-0.43	-0.27	-0.28	-0.23	-0.19	-0.23	-0.28	-0.27	-0.43	-0.54	-0.40	0.10	0.73	1.00
20	0.73	1.00	0.64	0.02	-0.36	-0.40	-0.26	-0.22	-0.18	-0.14	-0.15	-0.21	-0.13	-0.24	-0.42	-0.53	-0.31	0.23	0.73
40	0.10	0.64	1.00	0.69	0.19	-0.05	-0.06	0.02	0.03	0.06	0.08	0.03	0.16	0.19	0.02	-0.31	-0.49	-0.31	0.10
60	-0.40	0.02	0.69	1.00	0.77	0.43	0.24	0.30	0.29	0.26	0.32	0.28	0.40	0.57	0.50	0.13	-0.31	-0.53	-0.40
80	-0.54	-0.36	0.19	0.77	1.00	0.79	0.46	0.45	0.43	0.33	0.40	0.37	0.42	0.68	0.75	0.50	0.02	-0.42	-0.54
100	-0.43	-0.40	-0.05	0.43	0.79	1.00	0.69	0.47	0.40	0.26	0.29	0.26	0.27	0.55	0.68	0.57	0.19	-0.24	-0.43
120	-0.27	-0.26	-0.06	0.24	0.46	0.69	1.00	0.62	0.35	0.26	0.15	0.12	0.07	0.27	0.42	0.40	0.16	-0.13	-0.27
140	-0.28	-0.22	0.02	0.30	0.45	0.47	0.62	1.00	0.52	0.36	0.23	0.21	0.12	0.26	0.37	0.28	0.03	-0.21	-0.28
160	-0.23	-0.18	0.03	0.29	0.43	0.40	0.35	0.52	1.00	0.39	0.31	0.23	0.15	0.29	0.40	0.32	0.08	-0.15	-0.23
180	-0.19	-0.14	0.06	0.26	0.33	0.26	0.26	0.36	0.39	1.00	0.39	0.36	0.26	0.26	0.33	0.26	0.06	-0.14	-0.19
200	-0.23	-0.15	0.08	0.32	0.40	0.29	0.15	0.23	0.31	0.39	1.00	0.52	0.35	0.40	0.43	0.29	0.03	-0.18	-0.23
220	-0.28	-0.21	0.03	0.28	0.37	0.26	0.12	0.21	0.23	0.36	0.52	1.00	0.62	0.47	0.45	0.30	0.02	-0.22	-0.28
240	-0.27	-0.13	0.16	0.40	0.42	0.27	0.07	0.12	0.15	0.26	0.35	0.62	1.00	0.69	0.46	0.24	-0.06	-0.26	-0.27
260	-0.43	-0.24	0.19	0.57	0.68	0.55	0.27	0.26	0.29	0.26	0.40	0.47	0.69	1.00	0.79	0.43	-0.05	-0.40	-0.43
280	-0.54	-0.42	0.02	0.50	0.75	0.68	0.42	0.37	0.40	0.33	0.43	0.45	0.46	0.79	1.00	0.77	0.19	-0.36	-0.54
300	-0.40	-0.53	-0.31	0.13	0.50	0.57	0.40	0.28	0.32	0.26	0.29	0.30	0.24	0.43	0.77	1.00	0.69	0.02	-0.40

320	0.10	-0.31	-0.49	-0.31	0.02	0.19	0.16	0.03	0.08	0.06	0.03	0.02	-0.06	-0.05	0.19	0.69	1.00	0.64	0.10
340	0.73	0.23	-0.31	-0.53	-0.42	-0.24	-0.13	-0.21	-0.15	-0.14	-0.18	-0.22	-0.26	-0.40	-0.36	0.02	0.64	1.00	0.73
360	1.00	0.73	0.10	-0.40	-0.54	-0.43	-0.27	-0.28	-0.23	-0.19	-0.23	-0.28	-0.27	-0.43	-0.54	-0.40	0.10	0.73	1.00

Table A.3 Load data: horizontal correlations tip region 2 (SR0, effect of the rings on the load not included)

TIP REGION N.2																			
	0	20	40	60	80	100	120	140	160	180	200	220	240	260	280	300	320	340	360
0	1.00	0.69	-0.05	-0.55	-0.65	-0.38	-0.18	-0.27	-0.21	-0.15	-0.21	-0.27	-0.18	-0.38	-0.65	-0.55	-0.05	0.69	1.00
20	0.69	1.00	0.61	-0.02	-0.39	-0.36	-0.14	-0.17	-0.15	-0.10	-0.12	-0.19	-0.08	-0.18	-0.52	-0.70	-0.55	0.07	0.69
40	-0.05	0.61	1.00	0.73	0.29	-0.02	0.06	0.14	0.07	0.06	0.11	0.08	0.13	0.21	-0.01	-0.37	-0.67	-0.55	-0.05
60	-0.55	-0.02	0.73	1.00	0.82	0.41	0.30	0.38	0.28	0.18	0.29	0.31	0.26	0.44	0.44	0.11	-0.37	-0.70	-0.55
80	-0.65	-0.39	0.29	0.82	1.00	0.78	0.54	0.50	0.40	0.21	0.34	0.39	0.24	0.45	0.63	0.44	-0.01	-0.52	-0.65
100	-0.38	-0.36	-0.02	0.41	0.78	1.00	0.79	0.46	0.41	0.13	0.21	0.23	0.04	0.18	0.45	0.44	0.21	-0.18	-0.38
120	-0.18	-0.14	0.06	0.30	0.54	0.79	1.00	0.56	0.37	0.11	0.11	0.12	-0.04	0.04	0.24	0.26	0.13	-0.08	-0.18
140	-0.27	-0.17	0.14	0.38	0.50	0.46	0.56	1.00	0.48	0.14	0.19	0.21	0.12	0.23	0.39	0.31	0.08	-0.19	-0.27
160	-0.21	-0.15	0.07	0.28	0.40	0.41	0.37	0.48	1.00	0.05	0.18	0.19	0.11	0.21	0.34	0.29	0.11	-0.12	-0.21
180	-0.15	-0.10	0.06	0.18	0.21	0.13	0.11	0.14	0.05	1.00	0.05	0.14	0.11	0.13	0.21	0.18	0.06	-0.10	-0.15
200	-0.21	-0.12	0.11	0.29	0.34	0.21	0.11	0.19	0.18	0.05	1.00	0.48	0.37	0.41	0.40	0.28	0.07	-0.15	-0.21
220	-0.27	-0.19	0.08	0.31	0.39	0.23	0.12	0.21	0.19	0.14	0.48	1.00	0.56	0.46	0.50	0.38	0.14	-0.17	-0.27
240	-0.18	-0.08	0.13	0.26	0.24	0.04	-0.04	0.12	0.11	0.11	0.37	0.56	1.00	0.79	0.54	0.30	0.06	-0.14	-0.18
260	-0.38	-0.18	0.21	0.44	0.45	0.18	0.04	0.23	0.21	0.13	0.41	0.46	0.79	1.00	0.78	0.41	-0.02	-0.36	-0.38
280	-0.65	-0.52	-0.01	0.44	0.63	0.45	0.24	0.39	0.34	0.21	0.40	0.50	0.54	0.78	1.00	0.82	0.29	-0.39	-0.65
300	-0.55	-0.70	-0.37	0.11	0.44	0.44	0.26	0.31	0.29	0.18	0.28	0.38	0.30	0.41	0.82	1.00	0.73	-0.02	-0.55
320	-0.05	-0.55	-0.67	-0.37	-0.01	0.21	0.13	0.08	0.11	0.06	0.07	0.14	0.06	-0.02	0.29	0.73	1.00	0.61	-0.05
340	0.69	0.07	-0.55	-0.70	-0.52	-0.18	-0.08	-0.19	-0.12	-0.10	-0.15	-0.17	-0.14	-0.36	-0.39	-0.02	0.61	1.00	0.69
360	1.00	0.69	-0.05	-0.55	-0.65	-0.38	-0.18	-0.27	-0.21	-0.15	-0.21	-0.27	-0.18	-0.38	-0.65	-0.55	-0.05	0.69	1.00

Table A.4 Load data: horizontal correlations tip region 3 (SR0, effect of the rings on the load not included)

TIP REGION N.3																			
	0	20	40	60	80	100	120	140	160	180	200	220	240	260	280	300	320	340	360
0	1.00	0.67	-0.09	-0.56	-0.61	-0.21	-0.19	-0.20	-0.19	-0.17	-0.19	-0.20	-0.19	-0.21	-0.61	-0.56	-0.09	0.67	1.00
20	0.67	1.00	0.65	0.06	-0.32	-0.22	-0.04	-0.04	-0.08	-0.10	-0.16	-0.19	-0.18	0.03	-0.47	-0.70	-0.63	-0.08	0.67
40	-0.09	0.65	1.00	0.76	0.32	-0.04	0.31	0.30	0.25	0.12	0.05	-0.02	0.00	0.25	0.04	-0.35	-0.69	-0.63	-0.09
60	-0.56	0.06	0.76	1.00	0.82	0.32	0.52	0.49	0.44	0.29	0.21	0.15	0.16	0.30	0.42	0.14	-0.35	-0.70	-0.56
80	-0.61	-0.32	0.32	0.82	1.00	0.71	0.65	0.57	0.54	0.35	0.23	0.19	0.15	0.20	0.52	0.42	0.04	-0.47	-0.61
100	-0.21	-0.22	-0.04	0.32	0.71	1.00	0.71	0.47	0.52	0.22	0.03	0.02	-0.10	-0.28	0.20	0.30	0.25	0.03	-0.21
120	-0.19	-0.04	0.31	0.52	0.65	0.71	1.00	0.75	0.67	0.36	0.01	0.01	-0.06	-0.10	0.15	0.16	0.00	-0.18	-0.19
140	-0.20	-0.04	0.30	0.49	0.57	0.47	0.75	1.00	0.74	0.39	0.08	0.08	0.01	0.02	0.19	0.15	-0.02	-0.19	-0.20
160	-0.19	-0.08	0.25	0.44	0.54	0.52	0.67	0.74	1.00	0.45	0.09	0.08	0.01	0.03	0.23	0.21	0.05	-0.16	-0.19

180	-0.17	-0.10	0.12	0.29	0.35	0.22	0.36	0.39	0.45	1.00	0.45	0.39	0.36	0.22	0.35	0.29	0.12	-0.10	-0.17
200	-0.19	-0.16	0.05	0.21	0.23	0.03	0.01	0.08	0.09	0.45	1.00	0.74	0.67	0.52	0.54	0.44	0.25	-0.08	-0.19
220	-0.20	-0.19	-0.02	0.15	0.19	0.02	0.01	0.08	0.08	0.39	0.74	1.00	0.75	0.47	0.57	0.49	0.30	-0.04	-0.20
240	-0.19	-0.18	0.00	0.16	0.15	-0.10	-0.06	0.01	0.01	0.36	0.67	0.75	1.00	0.71	0.65	0.52	0.31	-0.04	-0.19
260	-0.21	0.03	0.25	0.30	0.20	-0.28	-0.10	0.02	0.03	0.22	0.52	0.47	0.71	1.00	0.71	0.32	-0.04	-0.22	-0.21
280	-0.61	-0.47	0.04	0.42	0.52	0.20	0.15	0.19	0.23	0.35	0.54	0.57	0.65	0.71	1.00	0.82	0.32	-0.32	-0.61
300	-0.56	-0.70	-0.35	0.14	0.42	0.30	0.16	0.15	0.21	0.29	0.44	0.49	0.52	0.32	0.82	1.00	0.76	0.06	-0.56
320	-0.09	-0.63	-0.69	-0.35	0.04	0.25	0.00	-0.02	0.05	0.12	0.25	0.30	0.31	-0.04	0.32	0.76	1.00	0.65	-0.09
340	0.67	-0.08	-0.63	-0.70	-0.47	0.03	-0.18	-0.19	-0.16	-0.10	-0.08	-0.04	-0.04	-0.22	-0.32	0.06	0.65	1.00	0.67
360	1.00	0.67	-0.09	-0.56	-0.61	-0.21	-0.19	-0.20	-0.19	-0.17	-0.19	-0.20	-0.19	-0.21	-0.61	-0.56	-0.09	0.67	1.00

Table A.5 Load data: horizontal correlations tip region 4 (SR0, effect of the rings on the load not included)

TIP REGION N.4																			
	0	20	40	60	80	100	120	140	160	180	200	220	240	260	280	300	320	340	360
0	1.00	0.66	-0.07	-0.55	-0.51	0.00	-0.14	-0.16	-0.15	-0.15	-0.15	-0.16	-0.14	0.00	-0.51	-0.55	-0.07	0.66	1.00
20	0.66	1.00	0.65	0.03	-0.35	-0.19	-0.01	0.00	-0.02	-0.05	-0.10	-0.12	-0.09	0.23	-0.29	-0.68	-0.62	-0.05	0.66
40	-0.07	0.65	1.00	0.73	0.17	-0.18	0.25	0.28	0.25	0.18	0.11	0.09	0.10	0.36	0.18	-0.31	-0.68	-0.62	-0.07
60	-0.55	0.03	0.73	1.00	0.70	0.07	0.47	0.51	0.48	0.40	0.30	0.28	0.26	0.29	0.51	0.20	-0.31	-0.68	-0.55
80	-0.51	-0.35	0.17	0.70	1.00	0.60	0.62	0.61	0.60	0.48	0.34	0.31	0.25	0.01	0.47	0.51	0.18	-0.29	-0.51
100	0.00	-0.19	-0.18	0.07	0.60	1.00	0.48	0.40	0.40	0.29	0.14	0.10	0.04	-0.22	0.01	0.29	0.36	0.23	0.00
120	-0.14	-0.01	0.25	0.47	0.62	0.48	1.00	0.71	0.63	0.49	0.32	0.27	0.23	0.04	0.25	0.26	0.10	-0.09	-0.14
140	-0.16	0.00	0.28	0.51	0.61	0.40	0.71	1.00	0.76	0.55	0.38	0.32	0.27	0.10	0.31	0.28	0.09	-0.12	-0.16
160	-0.15	-0.02	0.25	0.48	0.60	0.40	0.63	0.76	1.00	0.68	0.46	0.38	0.32	0.14	0.34	0.30	0.11	-0.10	-0.15
180	-0.15	-0.05	0.18	0.40	0.48	0.29	0.49	0.55	0.68	1.00	0.68	0.55	0.49	0.29	0.48	0.40	0.18	-0.05	-0.15
200	-0.15	-0.10	0.11	0.30	0.34	0.14	0.32	0.38	0.46	0.68	1.00	0.76	0.63	0.40	0.60	0.48	0.25	-0.02	-0.15
220	-0.16	-0.12	0.09	0.28	0.31	0.10	0.27	0.32	0.38	0.55	0.76	1.00	0.71	0.40	0.61	0.51	0.28	0.00	-0.16
240	-0.14	-0.09	0.10	0.26	0.25	0.04	0.23	0.27	0.32	0.49	0.63	0.71	1.00	0.48	0.62	0.47	0.25	-0.01	-0.14
260	0.00	0.23	0.36	0.29	0.01	-0.22	0.04	0.10	0.14	0.29	0.40	0.40	0.48	1.00	0.60	0.07	-0.18	-0.19	0.00
280	-0.51	-0.29	0.18	0.51	0.47	0.01	0.25	0.31	0.34	0.48	0.60	0.61	0.62	0.60	1.00	0.70	0.17	-0.35	-0.51
300	-0.55	-0.68	-0.31	0.20	0.51	0.29	0.26	0.28	0.30	0.40	0.48	0.51	0.47	0.07	0.70	1.00	0.73	0.03	-0.55
320	-0.07	-0.62	-0.68	-0.31	0.18	0.36	0.10	0.09	0.11	0.18	0.25	0.28	0.25	-0.18	0.17	0.73	1.00	0.65	-0.07
340	0.66	-0.05	-0.62	-0.68	-0.29	0.23	-0.09	-0.12	-0.10	-0.05	-0.02	0.00	-0.01	-0.19	-0.35	0.03	0.65	1.00	0.66
360	1.00	0.66	-0.07	-0.55	-0.51	0.00	-0.14	-0.16	-0.15	-0.15	-0.15	-0.16	-0.14	0.00	-0.51	-0.55	-0.07	0.66	1.00

Table A.6 Load data: horizontal correlations normal region (SR0, effect of the rings on the load not included)

NORMAL REGION																			
	0	20	40	60	80	100	120	140	160	180	200	220	240	260	280	300	320	340	360
0	1.00	0.70	-0.06	-0.59	-0.54	0.07	-0.14	-0.17	-0.18	-0.17	-0.18	-0.17	-0.14	0.07	-0.54	-0.59	-0.06	0.70	1.00
20	0.70	1.00	0.64	-0.03	-0.44	-0.16	-0.01	-0.02	-0.04	-0.07	-0.11	-0.13	-0.09	0.27	-0.29	-0.70	-0.60	-0.02	0.70

40	-0.06	0.64	1.00	0.71	0.12	-0.19	0.27	0.29	0.29	0.23	0.15	0.11	0.12	0.37	0.24	-0.30	-0.68	-0.60	-0.06
60	-0.59	-0.03	0.71	1.00	0.69	0.06	0.50	0.54	0.56	0.48	0.36	0.30	0.28	0.24	0.54	0.26	-0.30	-0.70	-0.59
80	-0.54	-0.44	0.12	0.69	1.00	0.61	0.66	0.65	0.67	0.54	0.36	0.29	0.23	-0.14	0.38	0.54	0.24	-0.29	-0.54
100	0.07	-0.16	-0.19	0.06	0.61	1.00	0.54	0.44	0.45	0.32	0.14	0.07	0.03	-0.30	-0.14	0.24	0.37	0.27	0.07
120	-0.14	-0.01	0.27	0.50	0.66	0.54	1.00	0.75	0.70	0.58	0.38	0.28	0.25	0.03	0.23	0.28	0.12	-0.09	-0.14
140	-0.17	-0.02	0.29	0.54	0.65	0.44	0.75	1.00	0.83	0.64	0.44	0.33	0.28	0.07	0.29	0.30	0.11	-0.13	-0.17
160	-0.18	-0.04	0.29	0.56	0.67	0.45	0.70	0.83	1.00	0.79	0.56	0.44	0.38	0.14	0.36	0.36	0.15	-0.11	-0.18
180	-0.17	-0.07	0.23	0.48	0.54	0.32	0.58	0.64	0.79	1.00	0.79	0.64	0.58	0.32	0.54	0.48	0.23	-0.07	-0.17
200	-0.18	-0.11	0.15	0.36	0.36	0.14	0.38	0.44	0.56	0.79	1.00	0.83	0.70	0.45	0.67	0.56	0.29	-0.04	-0.18
220	-0.17	-0.13	0.11	0.30	0.29	0.07	0.28	0.33	0.44	0.64	0.83	1.00	0.75	0.44	0.65	0.54	0.29	-0.02	-0.17
240	-0.14	-0.09	0.12	0.28	0.23	0.03	0.25	0.28	0.38	0.58	0.70	0.75	1.00	0.54	0.66	0.50	0.27	-0.01	-0.14
260	0.07	0.27	0.37	0.24	-0.14	-0.30	0.03	0.07	0.14	0.32	0.45	0.44	0.54	1.00	0.61	0.06	-0.19	-0.16	0.07
280	-0.54	-0.29	0.24	0.54	0.38	-0.14	0.23	0.29	0.36	0.54	0.67	0.65	0.66	0.61	1.00	0.69	0.12	-0.44	-0.54
300	-0.59	-0.70	-0.30	0.26	0.54	0.24	0.28	0.30	0.36	0.48	0.56	0.54	0.50	0.06	0.69	1.00	0.71	-0.03	-0.59
320	-0.06	-0.60	-0.68	-0.30	0.24	0.37	0.12	0.11	0.15	0.23	0.29	0.29	0.27	-0.19	0.12	0.71	1.00	0.64	-0.06
340	0.70	-0.02	-0.60	-0.70	-0.29	0.27	-0.09	-0.13	-0.11	-0.07	-0.04	-0.02	-0.01	-0.16	-0.44	-0.03	0.64	1.00	0.70
360	1.00	0.70	-0.06	-0.59	-0.54	0.07	-0.14	-0.17	-0.18	-0.17	-0.18	-0.17	-0.14	0.07	-0.54	-0.59	-0.06	0.70	1.00

Table A.7 Load data: horizontal correlations bottom region (SR0, effect of the rings on the load not included)

BOTTOM REGION																			
	0	20	40	60	80	100	120	140	160	180	200	220	240	260	280	300	320	340	360
0	1.00	0.71	-0.14	-0.66	-0.73	0.02	-0.25	-0.31	-0.32	-0.33	-0.32	-0.31	-0.25	0.02	-0.73	-0.66	-0.14	0.71	1.00
20	0.71	1.00	0.66	-0.14	-0.51	-0.44	-0.16	-0.15	-0.16	-0.19	-0.21	-0.21	-0.15	0.24	-0.48	-0.75	-0.67	0.08	0.71
40	-0.14	0.66	1.00	0.73	0.24	-0.29	0.27	0.31	0.29	0.26	0.20	0.18	0.24	0.51	0.33	-0.27	-0.68	-0.67	-0.14
60	-0.66	-0.14	0.73	1.00	0.81	0.23	0.56	0.59	0.57	0.54	0.47	0.44	0.41	0.53	0.71	0.40	-0.27	-0.75	-0.66
80	-0.73	-0.51	0.24	0.81	1.00	0.73	0.69	0.67	0.69	0.63	0.54	0.50	0.38	-0.13	0.79	0.71	0.33	-0.48	-0.73
100	0.02	-0.44	-0.29	0.23	0.73	1.00	0.64	0.52	0.53	0.42	0.29	-0.03	-0.06	-0.35	-0.13	0.53	0.51	0.24	0.02
120	-0.25	-0.16	0.27	0.56	0.69	0.64	1.00	0.78	0.72	0.58	0.36	0.32	0.25	-0.06	0.38	0.41	0.24	-0.15	-0.25
140	-0.31	-0.15	0.31	0.59	0.67	0.52	0.78	1.00	0.84	0.65	0.44	0.39	0.32	-0.03	0.50	0.44	0.18	-0.21	-0.31
160	-0.32	-0.16	0.29	0.57	0.69	0.53	0.72	0.84	1.00	0.78	0.52	0.44	0.36	0.29	0.54	0.47	0.20	-0.21	-0.32
180	-0.33	-0.19	0.26	0.54	0.63	0.42	0.58	0.65	0.78	1.00	0.78	0.65	0.58	0.42	0.63	0.54	0.26	-0.19	-0.33
200	-0.32	-0.21	0.20	0.47	0.54	0.29	0.36	0.44	0.52	0.78	1.00	0.84	0.72	0.53	0.69	0.57	0.29	-0.16	-0.32
220	-0.31	-0.21	0.18	0.44	0.50	-0.03	0.32	0.39	0.44	0.65	0.84	1.00	0.78	0.52	0.67	0.59	0.31	-0.15	-0.31
240	-0.25	-0.15	0.24	0.41	0.38	-0.06	0.25	0.32	0.36	0.58	0.72	0.78	1.00	0.64	0.69	0.56	0.27	-0.16	-0.25
260	0.02	0.24	0.51	0.53	-0.13	-0.35	-0.06	-0.03	0.29	0.42	0.53	0.52	0.64	1.00	0.73	0.23	-0.29	-0.44	0.02
280	-0.73	-0.48	0.33	0.71	0.79	-0.13	0.38	0.50	0.54	0.63	0.69	0.67	0.69	0.73	1.00	0.81	0.24	-0.51	-0.73
300	-0.66	-0.75	-0.27	0.40	0.71	0.53	0.41	0.44	0.47	0.54	0.57	0.59	0.56	0.23	0.81	1.00	0.73	-0.14	-0.66
320	-0.14	-0.67	-0.68	-0.27	0.33	0.51	0.24	0.18	0.20	0.26	0.29	0.31	0.27	-0.29	0.24	0.73	1.00	0.66	-0.14
340	0.71	0.08	-0.67	-0.75	-0.48	0.24	-0.15	-0.21	-0.21	-0.19	-0.16	-0.15	-0.16	-0.44	-0.51	-0.14	0.66	1.00	0.71
360	1.00	0.71	-0.14	-0.66	-0.73	0.02	-0.25	-0.31	-0.32	-0.33	-0.32	-0.31	-0.25	0.02	-0.73	-0.66	-0.14	0.71	1.00

10.2 The beam response (Chapter 7)

Table A.8 Load data: mean and rms drag forces (SR0, effect of the rings on the load not included)

z [m]	U [m/s]	q_m [kN/m ²]	D [m]	Δz [m]	$C_{D,m}$	F_m [kN]	$C_{D,\sigma}$	F_σ [kN]	
990	51.22	1.640	150	30	0.725	5346.37	0.120	884.04	
950	50.86	1.616	150	40	0.799	7751.58	0.111	1078.48	
910	50.48	1.593	150	30	0.769	5513.67	0.115	822.48	
890	50.29	1.581	150	30	0.716	5091.11	0.113	806.49	
850	49.89	1.556	150	70	0.606	9901.57	0.100	1635.98	
750	48.83	1.490	150	100	0.501	11192.00	0.080	1791.60	
650	47.64	1.419	150	100	0.486	10337.94	0.078	1661.10	
550	46.30	1.340	150	65	0.486	6345.71	0.084	1094.48	
520	45.85	1.314	150	22.5	0.492	2183.83	0.089	393.90	
505	45.62	1.301	150	12.5	0.483	1177.26	0.090	219.80	
495	45.46	1.292	150	12.5	0.482	1167.56	0.092	221.95	
480	45.22	1.278	150	22.5	0.504	2173.84	0.092	397.82	
450	44.73	1.250	150	65	0.508	6196.09	0.094	1142.33	
350	42.83	1.147	158.94	100	0.554	10098.03	0.116	2115.57	
250	40.43	1.021	183.15	100	0.604	11306.93	0.139	2592.24	
150	38.34	0.919	217.59	100	0.698	13956.99	0.163	3251.36	
50	33.26	0.691	258.20	100	0.816	14564.22	0.206	3668.03	
$M_{D,m}(z=0)$	6.45E+07	kNm							
$M_{D,\sigma}(z=0)$	6.53E+06	kNm	including lack of correlation						
$M_{D,peak}(z=0)$	8.74E+07	kNm							

Table A.9 Load data: correlation matrix of drag forces (SR0, effect of the rings on the load not included)

Z [m]	990	950	910	890	850	750	650	550	520	505	495	480	450	350	250	150	50
990	1.000	0.683	0.445	0.387	0.357	0.316	0.214	0.129	0.031	0.028	0.026	0.023	0.019	0.009	0.004	0.002	0.001
950	0.683	1.000	0.705	0.614	0.519	0.425	0.341	0.155	0.112	0.104	0.099	0.091	0.078	0.047	0.028	0.017	0.010
910	0.445	0.705	1.000	0.863	0.610	0.393	0.308	0.187	0.117	0.108	0.102	0.094	0.079	0.046	0.026	0.015	0.009
890	0.387	0.614	0.863	1.000	0.710	0.398	0.337	0.205	0.130	0.120	0.114	0.105	0.089	0.051	0.029	0.017	0.010
850	0.357	0.519	0.610	0.710	1.000	0.477	0.365	0.247	0.160	0.148	0.140	0.129	0.109	0.063	0.036	0.021	0.012
750	0.316	0.425	0.393	0.398	0.477	1.000	0.583	0.407	0.329	0.306	0.291	0.271	0.234	0.144	0.089	0.055	0.034
650	0.214	0.341	0.308	0.337	0.365	0.583	1.000	0.610	0.497	0.458	0.433	0.399	0.343	0.202	0.119	0.070	0.041
550	0.129	0.155	0.187	0.205	0.247	0.407	0.610	1.000	0.845	0.775	0.735	0.685	0.613	0.347	0.204	0.120	0.071
520	0.031	0.112	0.117	0.130	0.160	0.329	0.497	0.845	1.000	0.916	0.856	0.806	0.687	0.410	0.240	0.188	0.084
505	0.028	0.104	0.108	0.120	0.148	0.306	0.458	0.775	0.916	1.000	0.945	0.847	0.722	0.444	0.260	0.201	0.091

495	0.026	0.099	0.102	0.114	0.140	0.291	0.433	0.735	0.856	0.945	1.000	0.905	0.763	0.468	0.274	0.210	0.096
480	0.023	0.091	0.094	0.105	0.129	0.271	0.399	0.685	0.806	0.847	0.905	1.000	0.839	0.506	0.297	0.225	0.103
450	0.019	0.078	0.079	0.089	0.109	0.234	0.343	0.613	0.687	0.722	0.763	0.839	1.000	0.606	0.348	0.326	0.121
350	0.009	0.047	0.046	0.051	0.063	0.144	0.202	0.347	0.410	0.444	0.468	0.506	0.606	1.000	0.590	0.431	0.205
250	0.004	0.028	0.026	0.029	0.036	0.089	0.119	0.204	0.240	0.260	0.274	0.297	0.348	0.590	1.000	0.637	0.348
150	0.002	0.017	0.015	0.017	0.021	0.055	0.070	0.120	0.188	0.201	0.210	0.225	0.326	0.431	0.637	1.000	0.590
50	0.001	0.010	0.009	0.010	0.012	0.034	0.041	0.071	0.084	0.091	0.096	0.103	0.121	0.205	0.348	0.590	1.000

Table A.10 Results – covariance method (SR0, effect of the rings on the load not included)

z [m]	$M_{D,m}$ [kNm]	$M_{D,\sigma}$ [kNm]	$M_{D,peak}$ [kNm]
0	6.45E+07	6.53E+06	8.74E+07
50	5.83E+07	5.98E+06	7.93E+07
100	5.28E+07	5.47E+06	7.20E+07
150	4.74E+07	4.98E+06	6.48E+07
200	4.26E+07	4.52E+06	5.84E+07
250	3.78E+07	4.08E+06	5.21E+07
300	3.36E+07	3.67E+06	4.64E+07
350	2.93E+07	3.26E+06	4.07E+07
400	2.56E+07	2.88E+06	3.57E+07
450	2.19E+07	2.51E+06	3.07E+07
500	1.85E+07	2.16E+06	2.61E+07
550	1.54E+07	1.82E+06	2.18E+07
600	1.27E+07	1.51E+06	1.79E+07
650	9.90E+06	1.20E+06	1.41E+07
700	7.66E+06	9.40E+05	1.09E+07
750	5.42E+06	6.81E+05	7.80E+06
800	3.74E+06	4.71E+05	5.39E+06
850	2.06E+06	2.68E+05	3.00E+06
900	9.24E+05	1.28E+05	1.37E+06
950	2.14E+05	3.54E+04	3.38E+05
1000	0.00E+00	0.00E+00	0.00E+00

Table A.11 Load data: mean drag forces (SR1, effect of ten rings on the load included)

z [m]	U [m/s]	q_m [kN/m ²]	D [m]	Δz [m]	$C_{D,m}$	$F_{D,m}$ [kN]
990	51.22	1.640	150	30	0.746	5503.44
950	50.86	1.616	150	40	0.689	6684.68
910	50.48	1.593	150	30	0.633	4533.52
890	50.29	1.581	150	30	0.599	4261.88
850	49.89	1.556	150	70	0.605	9882.94

750	48.83	1.490	150	100	0.606	13548.72
650	47.64	1.419	150	100	0.606	12901.86
550	46.30	1.340	150	65	0.623	8140.94
520	45.85	1.314	150	22.5	0.626	2775.63
505	45.62	1.301	150	12.5	0.616	1502.75
495	45.46	1.292	150	12.5	0.615	1490.81
480	45.22	1.278	150	22.5	0.637	2749.58
450	44.73	1.250	150	65	0.642	7822.83
350	42.83	1.147	158.9367	100	0.687	12530.31
250	40.43	1.021	183.1461	100	0.738	13803.53
150	38.34	0.919	217.5889	100	0.831	16625.38
50	33.26	0.691	258.2017	100	0.949	16946.00

$M_{D,m}(z=0)$ 7.01E+07 kNm

Table A.12 Load data: mean lift forces (SR1, effect of ten rings on the load included)

z [m]	U [m/s]	q_m [kN/m ²]	D [m]	Δz [m]	$C_{L,m}$	$F_{L,m}$ [kN]
950	50.86	1.616	150	100	0.250	6061.72
850	49.89	1.556	150	100	-0.250	-5834.30
750	48.83	1.490	150	100	0.250	5588.57
650	47.64	1.419	150	100	-0.250	-5320.27
550	46.30	1.340	150	100	0.250	5023.32
450	44.73	1.250	150	100	-0.250	-4688.45
350	42.83	1.147	158.9367	100	0.250	4556.57
250	40.43	1.021	183.1461	100	-0.250	-4677.06
150	38.34	0.919	217.5889	100	0.250	4998.87
50	33.26	0.691	258.2017	100	-0.250	-4461.95

$M_{L,m}(z=0)$ 3.14E+06 kNm

10.3 The shell response (Chapter 7)

Table A.13 Shell response (effect of the rings on the load not included)

Response at stagnation - wind tunnel model applied to codified wind profile												
z [m]	Mean				Rms				Peak			
	n11	n22	m11	m22	n11	n22	m11	m22	n11	n22	m11	m22
	kN/m	kN/m	kNm/m	kNm/m	kN/m	kN/m	kNm/m	kNm/m	kN/m	kN/m	kNm/m	kNm/m
5	335.32	2741.12	4.53	25.22	41.06	342.59	0.74	4.00	479.03	3940.17	7.11	39.21
55	-30.04	2651.49	-1.34	1.15	21.94	311.21	1.40	0.42	-106.83	3740.71	-6.22	2.61
85	-32.06	2597.99	-4.64	-10.72	24.94	291.88	1.06	2.02	-119.36	3619.56	-8.37	-17.80
95	222.23	2578.27	-1.06	8.03	26.92	285.34	0.51	0.96	316.45	3576.95	-2.85	11.40
105	233.55	2565.70	-0.39	14.53	28.21	280.28	0.33	2.41	332.27	3546.68	-1.53	22.97

Chapter 10. Appendix

115	-19.05	2552.11	-5.95	-11.41	25.31	275.53	1.29	2.22	-107.63	3516.45	-10.47	-19.19
155	-14.53	2507.25	-5.47	-0.44	26.56	261.37	1.89	0.40	-107.50	3422.06	-12.07	-1.83
185	-52.93	2477.19	-11.24	-19.16	31.85	255.38	2.50	3.83	-164.39	3371.02	-19.99	-32.58
195	515.17	2464.02	-6.58	5.46	78.50	253.57	1.44	0.97	789.91	3351.50	-11.64	8.86
205	547.41	2464.25	-3.98	22.90	83.14	253.12	1.05	3.79	838.40	3350.19	-7.66	36.16
215	-20.04	2466.68	-13.60	-22.08	26.55	252.82	2.80	4.22	-112.96	3351.54	-23.39	-36.86
255	17.78	2489.23	-11.93	-2.20	20.32	255.18	2.37	0.54	88.90	3382.37	-20.21	-4.08
285	-113.27	2510.73	-20.39	-29.92	34.99	260.08	3.24	4.51	-235.72	3421.00	-31.72	-45.71
295	1042.56	2512.81	-13.65	3.07	134.42	261.51	2.02	0.76	1513.03	3428.08	-20.73	5.75
305	1104.82	2511.19	-8.14	36.11	141.49	261.76	1.33	4.73	1600.02	3427.33	-12.78	52.68
315	-60.21	2497.76	-23.83	-36.98	29.41	260.20	3.46	5.27	-163.16	3408.47	-35.94	-55.41
355	50.31	2431.20	-17.84	-3.42	17.67	253.04	2.34	0.46	112.15	3316.84	-26.03	-5.05
385	-198.04	2369.43	-24.28	-31.75	38.45	248.09	2.92	3.76	-332.62	3237.75	-34.50	-44.89
395	1444.30	2342.28	-17.14	-2.28	152.59	245.97	1.94	0.37	1978.36	3203.19	-23.94	-3.56
405	1511.55	2273.12	-8.37	41.38	158.90	240.11	1.02	4.40	2067.69	3113.48	-11.95	56.80
415	-148.16	2173.71	-25.47	-41.04	33.57	231.74	2.85	4.61	-265.65	2984.78	-35.45	-57.16
455	-76.78	1758.99	-15.40	-2.81	17.09	197.91	1.57	0.27	-136.58	2451.67	-20.89	-3.77
485	-392.97	1516.14	-18.21	-22.41	35.29	177.32	1.98	2.22	-516.49	2136.75	-25.14	-30.18
495	1277.73	1455.16	-13.91	-6.96	122.81	171.26	1.35	0.75	1707.55	2054.56	-18.62	-9.57
505	1344.46	1359.20	-4.69	36.75	128.21	162.70	0.62	3.35	1793.18	1928.64	-6.85	48.47
515	-330.27	1248.70	-18.68	-32.04	29.86	153.43	1.97	3.01	-434.77	1785.70	-25.56	-42.56
555	-101.21	894.46	-10.62	-1.49	18.00	122.97	1.06	0.11	-164.20	1324.87	-14.33	-1.88
585	-418.55	742.47	-12.46	-14.42	45.33	107.04	1.21	1.42	-577.19	1117.09	-16.71	-19.38
595	1235.34	712.97	-10.92	-10.99	109.46	102.66	0.98	0.93	1618.46	1072.27	-14.37	-14.26
605	1306.75	643.71	-2.26	30.44	115.15	97.02	0.28	2.67	1709.76	983.29	-3.24	39.80
615	-354.78	557.16	-13.92	-24.87	40.06	91.46	1.33	2.27	-494.99	877.26	-18.59	-32.81
655	-103.39	305.08	-9.50	-1.47	17.60	75.48	1.06	0.18	-165.00	569.26	-13.22	-2.10
685	-453.16	230.75	-13.02	-15.39	47.03	65.96	1.25	1.46	-617.76	461.60	-17.40	-20.51
695	1368.64	226.78	-11.85	-11.48	119.31	62.18	1.05	0.94	1786.23	444.40	-15.52	-14.77
705	1487.98	178.65	-2.75	34.24	129.29	58.62	0.32	2.97	1940.51	383.82	-3.86	44.62
715	-390.52	111.66	-15.76	-28.18	41.92	56.65	1.50	2.52	-537.24	309.94	-21.00	-37.02
755	-105.66	-73.10	-10.28	-1.64	17.11	50.93	1.17	0.21	-165.53	-251.36	-14.37	-2.39
785	-475.22	-106.82	-13.86	-16.22	48.26	40.81	1.35	1.53	-644.14	-249.65	-18.57	-21.57
795	1444.15	-98.35	-12.73	-12.56	125.93	35.83	1.13	1.06	1884.89	-223.77	-16.67	-16.28
805	1571.51	-131.60	-2.95	36.27	136.62	34.26	0.33	3.17	2049.69	-251.52	-4.11	47.35
815	-408.62	-180.28	-16.64	-29.85	42.90	35.92	1.57	2.66	-558.77	-306.01	-22.14	-39.18
855	-107.58	-285.30	-10.46	-1.75	16.86	37.65	1.19	0.21	-166.61	-417.06	-14.62	-2.49
885	-456.89	-247.49	-13.43	-15.34	48.05	28.52	1.34	1.50	-625.07	-347.32	-18.12	-20.60
895	1371.62	-213.67	-12.38	-12.63	125.25	22.40	1.15	1.13	1810.01	-292.06	-16.40	-16.58
905	1496.61	-214.75	-2.71	35.16	136.46	21.47	0.31	3.22	1974.21	-289.91	-3.79	46.43
915	-390.32	-227.98	-15.79	-28.56	42.26	24.71	1.54	2.67	-538.21	-314.48	-21.18	-37.90
955	-99.88	-205.47	-9.70	-1.83	16.65	26.98	1.08	0.21	-158.17	-299.89	-13.47	-2.57
985	-245.32	-85.10	-12.36	-15.89	31.51	12.33	1.27	1.59	-355.60	-128.25	-16.80	-21.46
995	816.33	-28.47	-5.61	15.96	78.39	4.29	0.58	1.57	1090.70	-43.48	-7.63	21.47

Table A.14 Load modification induced by the rings: effect on the quasi-static response (peak values):

SR0 = load modification due to the rings not included;

SR1 = load modification due to 10 rings included

z	n11,peak at 0°		n22,peak at 0°		m11,peak at 0°		m22,peak at 0°	
	SR0	SR1	SR0	SR1	SR0	SR1	SR0	SR1
[m]	kN/m	kN/m	kN/m	kN/m	kNm/m	kNm/m	kNm/m	kNm/m
5	483	535	4042	4443	8	8	43	45
55	-137	-133	3802	4189	-8	-10	3	4
85	-138	-139	3666	4056	-10	-10	-20	-20
95	346	348	3619	4015	-4	-2	14	15
105	363	372	3584	3975	-3	0	25	25
115	-117	-101	3546	3924	-13	-10	-21	-21
155	-110	-101	3434	3766	-13	-6	-2	0
185	-171	-156	3385	3712	-22	-16	-35	-30
195	845	778	3370	3700	-12	-10	12	9
205	893	833	3365	3685	-9	-6	39	37
215	-124	-104	3352	3651	-26	-22	-39	-36
255	104	111	3357	3595	-23	-20	-5	-3
285	-257	-253	3419	3620	-35	-33	-49	-47
295	1587	1581	3442	3626	-22	-22	8	3
305	1675	1683	3442	3610	-14	-13	55	57
315	-183	-169	3408	3564	-39	-38	-58	-59
355	125	135	3287	3390	-29	-28	-6	-6
385	-356	-384	3221	3274	-37	-39	-47	-49
395	2056	2161	3196	3228	-25	-27	-4	-3
405	2147	2272	3103	3119	-13	-13	59	64
415	-286	-297	2958	2964	-37	-40	-60	-64
455	-147	-150	2393	2358	-22	-24	-4	-5
485	-570	-596	2091	2028	-26	-28	-32	-33
495	1754	1865	2020	1946	-19	-21	-9	-11
505	1842	1968	1896	1815	-7	-7	50	55
515	-484	-499	1747	1665	-26	-28	-44	-47
555	-169	-167	1295	1204	-15	-16	-2	-3
585	-586	-608	1113	1003	-17	-18	-20	-20
595	1646	1718	1078	961	-15	-16	-14	-16
605	1739	1825	993	876	-3	-3	40	43
615	-502	-510	885	776	-19	-20	-33	-35
655	-165	-166	581	496	-13	-14	-2	-2
685	-617	-634	483	401	-18	-18	-21	-21
695	1792	1839	475	390	-16	-16	-15	-16
705	1947	2007	415	338	-4	-4	45	47
715	-536	-542	331	268	-22	-22	-37	-38
755	-163	-164	-263	-321	-15	-15	-3	-3

785	-638	-650	-236	-284	-19	-19	-22	-22
795	1877	1912	-194	-239	-17	-17	-16	-17
805	2041	2085	-221	-261	-4	-4	47	49
815	-552	-558	-290	-322	-23	-23	-39	-40
855	-163	-166	-431	-436	-16	-16	-3	-3
885	-622	-639	-346	-344	-19	-19	-21	-21
895	1801	1846	-283	-280	-16	-17	-16	-17
905	1966	2014	-282	-279	-4	-4	46	48
915	-534	-550	-314	-313	-21	-22	-38	-39
955	-160	-170	-311	-316	-13	-13	-3	-3
985	-355	-393	-134	-137	-17	-17	-21	-22
995	1094	1099	-45	-47	-8	-8	21	22

Table A.15 Load modification induced by the rings: effect on the quasi-static response (mean values):

SR0 = load modification due to the rings not included;

SR1 = load modification due to 10 rings included

z	n11,m at 0°		n22,m at 0°		m11,m at 0°		m22,m at 0°	
	SR0	SR1	SR0	SR1	SR0	SR1	SR0	SR1
[m]	kN/m	kN/m	kN/m	kN/m	kNm/m	kNm/m	kNm/m	kNm/m
5	326	347	2695	2863	5	5	25	26
55	-34	-30	2603	2782	-1	-1	1	1
85	-34	-29	2551	2737	-5	-5	-11	-11
95	221	233	2533	2720	-1	-1	8	9
105	232	245	2520	2709	0	0	14	15
115	-21	-15	2506	2696	-6	-6	-11	-12
155	-15	-9	2465	2658	-6	-6	-1	0
185	-52	-45	2451	2644	-11	-11	-19	-19
195	517	523	2446	2637	-6	-6	6	6
205	548	553	2447	2637	-4	-4	23	23
215	-20	-12	2445	2631	-14	-14	-22	-22
255	19	26	2462	2630	-13	-12	-2	-2
285	-106	-100	2505	2652	-20	-20	-29	-29
295	1019	1029	2519	2657	-13	-13	4	3
305	1078	1090	2519	2649	-8	-8	35	36
315	-55	-48	2499	2621	-23	-23	-36	-36
355	52	57	2419	2504	-18	-18	-4	-4
385	-189	-193	2367	2419	-24	-24	-31	-31
395	1408	1440	2347	2387	-17	-17	-2	-3
405	1472	1509	2278	2308	-8	-8	40	42
415	-141	-144	2173	2196	-25	-26	-40	-41
455	-76	-76	1752	1747	-15	-16	-3	-3

485	-388	-392	1524	1497	-18	-18	-22	-22
495	1258	1289	1471	1435	-14	-14	-7	-8
505	1324	1361	1376	1334	-5	-5	36	38
515	-326	-326	1259	1215	-19	-19	-32	-33
555	-101	-97	897	837	-11	-11	-2	-2
585	-415	-415	758	680	-12	-13	-14	-14
595	1222	1231	735	651	-11	-11	-11	-12
605	1292	1306	667	580	-2	-2	30	31
615	-353	-349	574	489	-14	-14	-25	-25
655	-104	-101	312	232	-10	-10	-2	-2
685	-450	-447	250	169	-13	-13	-15	-15
695	1354	1346	254	173	-12	-12	-11	-12
705	1472	1468	204	128	-3	-3	34	35
715	-387	-382	127	58	-16	-16	-28	-28
755	-104	-103	-73	-114	-11	-11	-2	-2
785	-470	-466	-85	-112	-14	-14	-16	-16
795	1427	1413	-62	-87	-13	-13	-12	-13
805	1553	1541	-94	-113	-3	-3	36	36
815	-404	-397	-156	-166	-17	-17	-30	-29
855	-106	-104	-281	-272	-11	-11	-2	-2
885	-455	-457	-234	-222	-14	-14	-15	-15
895	1365	1360	-193	-182	-12	-12	-12	-12
905	1490	1484	-197	-186	-3	-3	35	35
915	-389	-393	-220	-211	-16	-16	-28	-28
955	-102	-107	-211	-210	-9	-9	-2	-2
985	-247	-272	-88	-89	-12	-12	-16	-16
995	817	798	-30	-30	-6	-6	16	16

Table A.16 Load modification induced by the rings: effect on the quasi-static response (rms values):

SR0 = load modification due to the rings not included;

SR1 = load modification due to 10 rings included

<i>z</i>	<i>n11,σ</i> at 0°		<i>n22,σ</i> at 0°		<i>m11,σ</i> at 0°		<i>m22,σ</i> at 0°	
	<i>SR0</i>	<i>SR1</i>	<i>SR0</i>	<i>SR1</i>	<i>SR0</i>	<i>SR1</i>	<i>SR0</i>	<i>SR1</i>
[m]	kN/m	kN/m	kN/m	kN/m	kNm/m	kNm/m	kNm/m	kNm/m
5	45	54	385	451	0.90	0.98	4.97	5.48
55	29	30	342	402	2.03	2.46	0.55	0.71
85	30	31	318	377	1.62	1.40	2.64	2.52
95	36	33	310	370	0.71	0.25	1.57	1.81
105	38	36	304	362	0.64	0.00	2.96	2.88
115	28	25	297	351	1.95	1.11	2.85	2.52
155	27	26	277	316	2.16	0.00	0.53	0.00

Chapter 10. Appendix

185	34	32	267	305	3.00	1.24	4.47	3.15
195	94	73	264	304	1.70	1.12	1.53	0.76
205	99	80	262	299	1.28	0.64	4.53	4.01
215	30	26	259	291	3.45	2.31	4.96	3.91
255	24	24	256	275	3.06	2.10	0.77	0.22
285	43	44	261	277	4.10	3.70	5.55	5.22
295	162	158	264	277	2.51	2.55	1.21	0.00
305	171	169	264	275	1.67	1.50	5.81	6.13
315	37	34	260	269	4.36	4.16	6.44	6.41
355	21	22	248	253	3.11	2.87	0.71	0.58
385	48	55	244	244	3.71	4.10	4.66	5.14
395	185	206	243	241	2.42	2.84	0.57	0.00
405	193	218	236	232	1.28	1.44	5.38	6.34
415	41	44	224	220	3.56	4.14	5.65	6.46
455	20	21	183	175	2.00	2.44	0.36	0.44
485	52	58	162	152	2.23	2.63	2.69	3.06
495	142	165	157	146	1.60	1.93	0.69	0.96
505	148	174	149	137	0.63	0.72	4.00	4.79
515	45	49	139	129	2.21	2.58	3.65	4.26
555	19	20	114	105	1.32	1.55	0.22	0.26
585	49	55	101	92	1.39	1.60	1.57	1.75
595	121	139	98	89	1.10	1.31	0.99	1.31
605	128	148	93	85	0.31	0.34	2.93	3.50
615	43	46	89	82	1.46	1.72	2.49	2.90
655	17	19	77	76	1.11	1.33	0.19	0.24
685	48	53	67	66	1.31	1.53	1.52	1.70
695	125	141	63	62	1.10	1.28	1.00	1.23
705	136	154	60	60	0.34	0.36	3.10	3.58
715	42	46	58	60	1.60	1.76	2.64	2.98
755	17	17	54	59	1.27	1.31	0.24	0.23
785	48	53	43	49	1.41	1.52	1.56	1.70
795	129	143	38	44	1.16	1.30	1.07	1.27
805	139	155	36	42	0.35	0.37	3.22	3.62
815	42	46	38	44	1.64	1.80	2.71	3.02
855	16	17	43	47	1.27	1.35	0.24	0.25
885	48	52	32	35	1.38	1.51	1.50	1.66
895	125	139	26	28	1.16	1.28	1.16	1.25
905	136	152	25	27	0.31	0.34	3.21	3.55
915	41	45	27	29	1.53	1.70	2.65	2.94
955	17	18	28	30	1.09	1.14	0.22	0.22
985	31	35	13	14	1.28	1.41	1.60	1.77
995	79	86	5	5	0.58	0.63	1.59	1.77

The number of decimals after the comma is just a matter of visualization. The values are calculated with higher precision in order to avoid significant truncation errors.

Curriculum Vitae

Personal information

First name / Surname **Francesca Lupi**
Nationality Italian
Date of birth 21/04/1984
Place of birth Prato, Italy
Gender Female
Mother tongue Italian
Other languages English, German

Occupational field **Civil Engineering**

Affiliation DICEA - Department of Civil and Environmental Engineering
University of Florence
Via di S. Marta 3
50139, Florence
Italy
E-mail francesca.lupi@dicea.unifi.it

Education

Dates 2010 - April 2013
Title of qualification Dottore di Ricerca / Dr.-Ing. (grade: outstanding)
awarded International Research Doctorate on “Mitigation of risk due to
natural hazards on structures and infrastructures”
Name of organisation Università degli Studi di Firenze / Technical University Carolo-
Wilhelmina Braunschweig
Dates February 2010
Title of qualification Registered Professional Engineer (Civil and Environmental
awarded Engineering Sector, Section A)
Name of organisation Ordine degli Ingegneri della Provincia di Prato, Italy
Dates 2007 - 2009
Title of qualification Master degree in Civil Engineering, major in Structural
awarded Engineering (110/110 cum laude)
Thesis: “Structural behaviour, optimization and design of a solar
chimney prototype under wind loading and other actions”.
Name of organisation Università degli Studi di Firenze, Florence, Italy

Dates	February - May 2009
	Erasmus placement
Name of organisation	Niemann&Partner Ingenieurgesellschaft, Bochum, Germany
Dates	2003 - 2007
Title of qualification awarded	Bachelor degree in Civil Engineering (110/110 cum laude)
	Thesis: “Progetto di parcheggio interrato in Piazza Mercatale a Prato” (“Desing of an underground parking in Piazza Mercatale, Prato”)
Name of organisation	Università degli Studi di Firenze, Florence, Italy
Dates	1998 - 2003
Title of qualification awarded	Scientific High School Diploma (100/100)
Name and type of organisation	Liceo Scientifico “Conservatorio San Niccolò”, Prato, Italy

Prizes and Awards

Date	September 2011
	“Outstanding young engineer contribution award” for the paper presented at IABSE-IASS 2011 symposium in London: “Non-conventional wind loading on ultra-high Towers in Solar Updraft Power Plants”.